Title

Using Multi-Modality Measurements to Investigate Intracranial Pressure Waveform Morphology in Patients with Normal Pressure Hydrocephalus

Author

Hamilton, Robert Benjamin

Publication Date

2014

Peer reviewed|Thesis/dissertation

UNIVERSITY OF CALIFORNIA

Los Angeles

Using Multi-Modality Measurements to Investigate Intracranial Pressure Waveform Morphology in Patients with Normal Pressure Hydrocephalus

A dissertation submitted in partial satisfaction of the

requirements for the degree Doctor of Philosophy

in Biomedical Engineering

by

Robert Benjamin Hamilton

2014

ABSTRACT OF THE DISSERTATION

Using Multi-Modality Measurements to Investigate Intracranial Pressure Waveform Morphology in Patients with Normal Pressure Hydrocephalus

by

Robert Benjamin Hamilton

Doctor of Philosophy in Biomedical Engineering

University of California, Los Angeles 2014

Professor Xiao Hu Ph.D. co-chair

Professor Marvin Bergsneider M.D. co-chair

Abstract

The dynamic environment of the cranial vault relies on normal brain pulsatility to maintain homeostasis. Small deviations in pressure or flow of either blood or cerebrospinal fluid (CSF) can drastically alter normal brain function. This thesis will investigate alterations in brain pulsatility in normal pressure hydrocephalus (NPH) patients; however, many of the conclusions/analysis methods have a broader impact and can be applied to other neurologic conditions, including traumatic brain injury and subarachnoid hemorrhage. Invasive intracranial pressure (ICP) monitoring and noninvasive Phase-contrast MRI (PC-MRI) will be used to measure brain pulsatility for this thesis, which is divided into three sections with three specific aims.

Study 1: It is commonly accepted that there is some degree of CSF dysfunction in NPH. The first study investigates the stroke volume, latency, and variability changes that occur in the cerebral aqueduct and prepontine cistern of NPH patients and age-

matched controls. Results show significant alterations in all aspects of CSF dynamics, which suggests decrease cisternal buffering, decreased compliance, and increased variability in the NPH cohort.

Study 2: Differentiating shunt responders and non-responders has been a cornerstone of NPH research for over 50 years. Several aspects of ICP monitoring have been investigated as possible prognostic tests for NPH; however, results remain inconsistent and inaccurate. The advanced morphological analysis techniques used in this study show higher accuracy than traditional ICP analysis. These features, once further validated, could replace existing methods for more expensive, less accurate shunt selections.

Study 3: Changes in pressure and flow dominate regulation of the internal dynamic environment of the brain; despite the physical relationship between the two phenomena, little is known about their impact on one another. Using CSF flow measured by PC-MRI, regional and individual ICP metrics that correlate with CSF flow were easily identified. This is a first step toward a better understanding of the characteristic peaks of the ICP pulse pressure waveform.

Conclusion: The aforementioned studies reveal that modest changes in brain pulsatility can be detected in NPH patients. Although it is unlikely that these changes are the sole reason for the symptoms of NPH, these studies make important advances in understanding the pathoetiology of NPH. These discoveries need further investigation, but have the potential to change the way NPH is diagnosed and treated in the future.

The dissertation of Robert Benjamin Hamilton is approved.

Nader Pouratian

Donatello Telesca

Xiao Hu, Co-Chair

Marvin Bergsneider, Co-Chair

University of California, Los Angeles

2014

Dedication

This is dedicated to the two most important women in my life

My mother

Connie Hamilton

and my honeybunny

Jennifer Fuller

Table of Contents

I. List of Abbreviations

ASV – Aqueductal Stroke Volume
AUC – Area Under the Curve
CBF – Cerebral Blood Flow
CBFV – Cerebral Blood Flow Velocity
CH – Communicating Hydrocephalus
CSF – Cerebrospinal Fluid
ECG – Electrocardiography
ELD – Extended Lumbar Drain
ICP – Intracranial Pressure
ICV – Intracranial Volume
iNPH – Idiopathic Normal Pressure Hydrocephalus
IRB – Institutional Review Board
iqr – InterQuartile Range
LD – Lumbar Drain
MCA – Middle Cerebral Artery
mICP – mean ICP
MMSE – Mini Mental Status Exam
MOCAIP – Morphological Clustering and Analysis of Continuous Intracranial Pulse
MRE – Magnetic Resonance Elastography
MRI – Magnetic Resonance Imaging
NPH – Normal Pressure Hydrocephalus
NRC – Normalized Region Contribution
PC-MRI – Phase Contrast Magnetic Resonance Imaging
PET – Positron Emission Tomography
PFL – Peak Flow Latency
R_O – CSF outflow resistance
ROC – Receiver Operator Characteristic
ROI – Region of Interest
SAH – Subarachnoid Hemorrhage
SEM – Standard Error of the Mean
SPECT – Single Photon Emission Computed Tomography
TBI – Traumatic Brain Injury
TCD – Transcranial Doppler
TSE – Turbo Spin Echo
UCLA – University of California, Los Angeles
VA – VentriculoAtrial
V_{enc} – Velocity encoding
VP – VentriculoPeritoneal
waveAmp – wave Amplitude of the ICP pulse pressure waveform
^{133}Xe – Xenon 133

II. Acknowledgments

I would like to express my deep appreciation for my co-advisors Dr. Xiao Hu and Dr. Marvin Bergsneider. Their guidance and mentorship over the past five years has changed my life on both a professional and personal level. In addition to my co-chairs, I would like to thank my other committee members, Dr. Nader Pouratian and Dr. Donatello Telesca.

I would like to thank my funding agencies, the National Institutes of Health (NIH): National Institute of Neurological Disorders and Stroke (NINDS) and the University of California, Los Angeles Department of Engineering for the Dissertation Year Fellowship.

Additionally, I would like to thank my fellow lab members Yong Bai, Dr. Fabien Scalzo, Dr. Magda Kasprowicz, Dr. Shadnaz Asgari, Dr. Sunghan Kim, Jessica Lu, Dr. Peng Xu, Mingxi Zhao, Shaozhi Wu, and Mark Connolly.

I would also like to thank the clinical team at UCLA, including Dr. Paul Vespa, Dr. Neil Martin, Dr. Nestor Gonzalez, Mireya Consiglio, the entire nursing staff of the neuro-intensive care unit, Dr. Tom Glenn, Dr. Dave McArthur, Chris Hanuscin, Mehj Furreedan, Karen Einstein, and Brenda Rinsky.

Finally, my friends and family (Dad and Roger) who got me through the past few years. Special thanks to Zaineb Ahmad for editing countless papers and abstracts, Most importantly I would like to thank Dr. Jennifer Fuller for her years of support.

III. Vita/Biographical Sketch

Education:

M.S., Biomedical Engineering, **University of California, Los Angeles**, 2009

B.S., Biomedical Engineering, **Washington University in Saint Louis**, 2008

B.A., Mathematics, **College of Idaho**, 2008

Publications and Presentations:

------- Journal Articles -------

S. Asgari, N. Gonzalez, A. Subduhi, **R. Hamilton**, M. Bergsneider, P. Vespa, X. Hu. "Continuous Detection of Cerebral Vasodilatation and Vasoconstriction Using Intracranial Pulse Morphological Template Matching". *Plos one 7.11 (2012): e50795.*

S. Kim, **R. Hamilton**, S. Pineles, M. Bergsneider, P. Vespa, N. Martin, X. Hu. "Noninvasive Intracranial Hypertension Detection Utilizing Semi-Supervised Learning." *IEEE Transactions on Biomedical Engineering*. (Accepted 10/2012)

N. Gonzalez, **R. Hamilton**, A. Freiert, J. Dusick, P.Vespa, X. Hu, S. Asgarid. "Cerebral Hemodynamic and Metabolic Effects of Remote Ischemic Preconditioning in Patients with Subarachnoid Hemorrhage." *Acta Neurochirurgica Supplementum*, Vol 115 2012

R. Hamilton, K. Baldwin, J. Fuller, P. Vespa, X. Hu, M. Bergsneider. "Intracranial Pressure Pulse Waveform Correlates with Aqueductal Cerebrospinal Fluid Stroke Volume". *J Appl Physiol,* vol. 113, pp. 1560-6, Nov.

F. Scalzo, **R. Hamilton**, S. Asgari, S. Kim, X. Hu. "Intracranial Hypertension Prediction using Extremely Randomized Decision Trees". Medical Engineering and Physics. In press, 2011.

X. Hu, **R. Hamilton**, K. Baldwin, P. Vespa, M. Bergsneider. "Automated Extraction of Decision Rules for Predicting Lumbar Drain Outcome by Analyzing Overnight Intracranial Pressure". *Acta Neurochir Suppl*, vol. 114, Acta Neurochir. Suppl. 114, 207-212, (2012).

S. Kim, X. Hu, D. McArthur, **R. Hamilton**, M. Bergsneider, T. Glenn, N. Martin, and P. Vespa, "Inter-Subject Correlation Exists Between Morphological Metrics of Cerebral Blood Flow Velocity and Intracranial Pressure Pulses," *Neurocrit Care*, Dec 7 2010.

S. Asgari, M. Bergsneider, **R. Hamilton**, P. Vespa, and X. Hu, "Consistent Changes in Intracranial Pressure Waveform Morphology Induced by Acute Hypercapnic Cerebral Vasodilatation," *Neurocrit Care*, Oct 2010

M. Kasprowicz, S. Asgari, M. Bergsneider, M. Czosnyka, **R. Hamilton**, and X. Hu, "Pattern recognition of overnight intracranial pressure slow waves using morphological features of intracranial pressure pulse," *J Neurosci Methods*, vol. 190, pp. 310-8, Jul 2010.

------- Conference Papers -------

R. Hamilton, J. Fuller, X. Hu, M. Bergsneider. “Elevation of the Third Peak of Intracranial Pressure Pulse Waveform Morphology Differentiated Normal Pressure Hydrocephalus Shunt Responders and Non-Responders” *Acta Neurochir Suppl,* vol. (Waiting review)

R. Hamilton, K. Baldwin, P. Vespa, M. Bergsneider, X. Hu. “Subpeak regional analysis of intracranial pressure waveform morphology based on cerebrospinal fluid hydrodynamics in the cerebral aqueduct and prepontine cistern”. In *Engineering in Medicine and Biology Society (EMBC), 2012 Annual International Conference of the IEEE* (pp. 3935-3938). IEEE.

R. Hamilton, J. Dye, A. Frew, K. Baldwin, X. Hu, and M. Bergsneider, "Quantification of Pulsatile, Cerebrospinal Fluid Flow within in the Prepontine Cistern," *Acta Neurochir Suppl,* vol. 114, 2011.

R. Hamilton. P. Xu, S. Asgari, M. Kasprowicz, P. Vespa, M. Bergsneider, X Hu. “Forecasting Plateau Waves Based on Prescient Changes of Intracranial Pressure Waveform Morphology”. *Conf Proc IEEE Eng Med Biol Soc,* vol. 2009, pp. 4331-4, 2009.

IV. Chapter 1

A. General Overview

The brain consumes 20 percent of the body's cardiac output and oxygen supply while accounting for only 2 percent of its weight, illustrating the critical importance of uninterrupted perfusion to the brain. Although the topic of cerebral blood flow and perfusion span a number of research areas, this thesis will focus specifically on brain pulsatility. Moreover, I will be investigating two distinct areas of brain pulsatility: the pathophysiology of normal pressure hydrocephalus (NPH) and shunt prediction and the source of the intracranial pressure (ICP) pulse pressure waveform morphology. Cerebral hydro- and hemodynamics and the techniques used to quantify them are complex, therefore basic principles and concepts are introduced prior to discussion of the specific aims of this research. First, I will describe the basics of intracranial pulsatility and the evolution of our understanding of it. Then, I will discuss the modalities used to measure intracranial pulsatility, including magnetic resonance imaging (MRI) and invasive ICP monitoring, along with the methods used to analyze them. Finally, I will describe specific aspects of pulsatility as they pertain to the diagnosis of and prediction of therapeutic efficacy.

B. Intracranial Dynamics

To understand the role of imaging and other monitoring techniques in measuring intracranial pulsatility, a basic understanding of cerebrospinal fluid (CSF) dynamics and hemodynamics is required. The cranial vault is composed of four fundamental components: arterial blood (50mL), venous blood (100mL), cerebrospinal fluid (150 mL),

and brain parenchyma (1400mL). The dynamic relationship between these elements is complex and crucial for adequate perfusion of the tissue.

1. Cerebrospinal Fluid (CSF)

CSF is a clear, water-like fluid (in fact, it is composed of 99 percent water) that circulates around the brain and spinal column (**Figure 1**). The brain essentially floats in the CSF, allowing major arterial conducting vessels to remain patent and provide adequate blood flow to the tissue. In addition to the mechanical support that the CSF provides, it also removes metabolic waste. There is approximately 150 mL of CSF within the brain and spinal cord at any given time. CSF is constantly produced and reabsorbed, with an average production rate of 500mL/day, resulting in a turnover rate of about three times per 24-hour period. CSF movement occurs by two different mechanisms, bulk flow and cardiac-induced flow. Bulk flow, shown in **Figure 1**, occurs from the production site of CSF in the choroid plexi within the ventricular system (lateral, third, and forth ventricles) to the site of reabsorption (venous system) in the arachnoid granulations.

Cardiac-induced CSF flow, which is a central theme in this thesis, increases flow volume two orders of magnitude more than bulk flow.[1] CSF flow within the cranial vault is pulsatile and contingent upon both arterial and venous blood flow. During systole, as arterial blood enters the base of the skull via the internal carotid arteries and vertebral arteries, CSF flows in the craniocaudal direction through the Foramen of Magendie from the fourth ventricle into the subarachnoid space before entering the spinal canal through the craniocervical junction. Just before the CSF exits the cranium, there is a momentary

increase in intracranial volume (ICV), which causes the periodic increase in ICP known as the ICP pulse pressure waveform. Following the CSF egress into the spinal canal, CSF flow reverses direction, moving in the caudalcranial direction, back into the cranial vault, as venous blood returns.

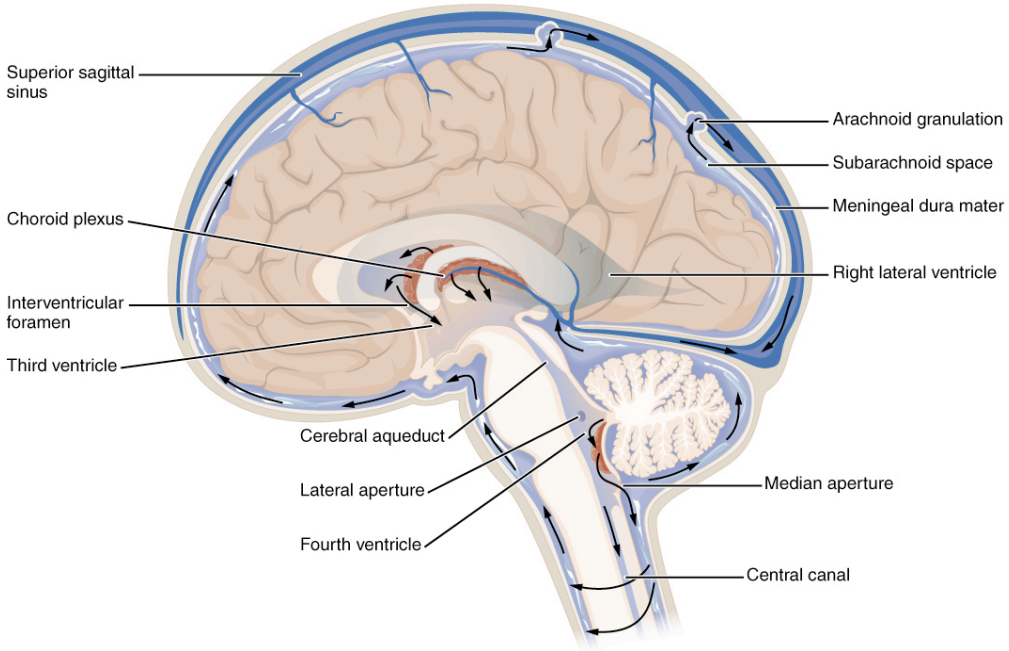

Figure 1: *The ventricular system. CSF flows from the choroid plexus in the lateral and third ventricles through the cerebral aqueduct and into the fourth ventricle. Reproduced with permission*[2]

Greitz[3] elegantly demonstrated this pulsatile movement of CSF and expanded on it with the observation that CSF movement occurs via two basic routes: the cisterns and the ventricles. The larger cisternal movement occurs in response to an up-and-down piston-like motion of the brain with every heartbeat, driven by changes in blood volume in the subarachnoid spaces. The smaller CSF movement out and back into the ventricles, on the other hand, results from a centripetal implosion of the cerebral hemispheres, primarily as a result of an increase in brain volume due to the increase in blood volume. Both cisternal and ventricular CSF volume buffering, as well as the temporal

relationship between the two systems, are important for normal cerebral hemodynamics. Specific hypotheses related to CSF movement are discussed further in Chapter 2.

2. Arterial Blood Flow

Oxygen-rich blood is pumped from the left ventricle through the aorta prior to entering the cranial vault via the vertebral arteries and the internal carotid arteries. **Figure 2** shows the major conducting arteries of the cerebral vasculature, known as the Circle of Willis. The compliance of the intracranial space gradually reduces the pulsatile flow of the arterial blood to a constant flow in the capillary bed. This phenomenon, known as the Windkessel effect, is related to the compliance of the arterial system and is essential for continuous perfusion of the brain tissue. Although arterial hemodynamics is critical for understanding cerebral dynamics, specifics are beyond the scope of this thesis and will only be explained as needed.

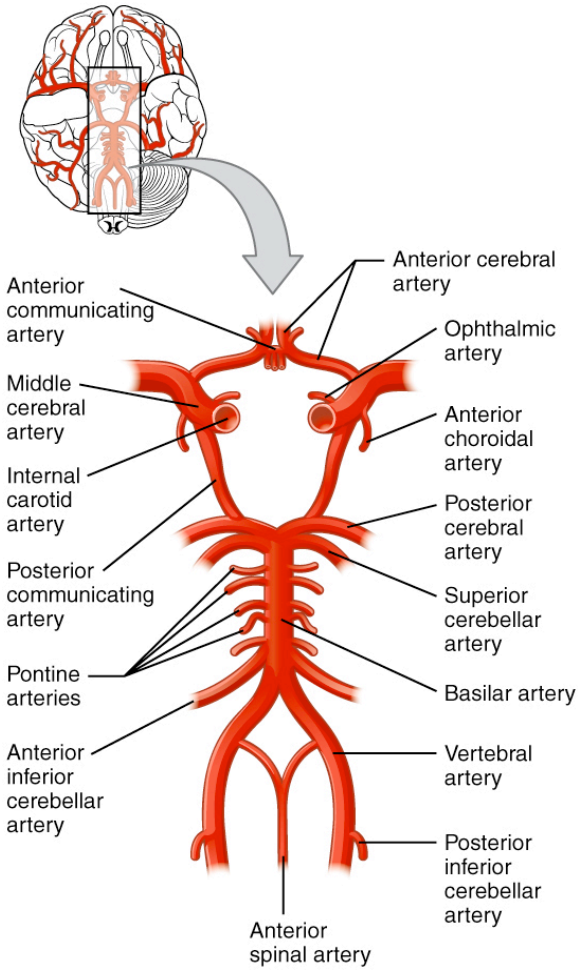

Figure 2: *Map of the Circle of Willis. Reproduced with permission*[2]

3. Venous Blood Flow

Unlike the arterial vasculature, the vessels of the venous system lack smooth muscle tone. This makes the venous system much more susceptible to collapse in the presence of external pressure. Furthermore, unlike the arterial system, which has both a posterior and an anterior path into the cranial vault (via the vertebral and internal carotid arteries, respectively), the venous system relies solely on the internal jugular veins. Again, the healthy dynamics of the venous system are critical to cerebral dynamics but details are beyond the scope of this thesis.

4. Intracranial Pressure (ICP)

ICP is defined as the pressure of the CSF within the cerebral ventricles.[4,5] Unlike most organs in the body, which are affected by atmospheric pressure, the components of the brain are encased within the skull, dramatically changing the pressure environment. Although the standard definition of ICP includes only CSF pressure, it is well known that there is a vascular component.[6] CSF pressure has been defined as the product of the resistance to outflow of CSF and the CSF production rate plus the pressure within the superior sagittal sinus.[6] Vascular pressure is much more complex, including aspects of cerebral blood volume, arterial pressure, venous pressure, and cerebral autoregulation.[6]

Clinically, ICP is a fundamental physiologic parameter that, if elevated, can lead to a pathological reduction in cerebral blood flow and possible herniation of the brain, resulting in irreversible brain damage or death if left untreated. Currently, mean ICP is used to diagnose dangerous increases in pressure and help guide treatment. Current Brain Trauma Foundation guidelines recommend treatment in acute brain injury patients with a mean ICP above 20 mmHg for greater than five minutes.[7] However, several studies have provided evidence that the current threshold should be higher, perhaps as high as 30 mmHg.[8,9] Furthermore, a recent study out of Latin America suggests that ICP monitoring provides no improvement in outcome compared to imaging alone; however, researchers have pointed out critical flaws in the study protocol, including the high mortality rates in both arms (~40%), and many maintain that ICP monitoring is critical to favorable patient outcomes.[10]

One unintended consequence of the Latin American study is a renewed focus on more advanced morphological features and dynamic aspects of ICP. There are two fundamental dynamic features of ICP, the slow wave and the ICP pulse pressure wave, which are described in detail below.

a) Slow waves

Much like CSF dynamics, which comprise two fundamental components (bulk flow and pulsatile flow), ICP monitoring is multifaceted and occurs on different time scales. Slow waves, originally classified by Lundberg in the 1960s, take many forms.[11] Lundberg defined three subsets of slow waves: A, B, and C. The characteristics of the individual waves are shown in **Table 1**, with examples of B waves shown in **Figure 3.** Although the origins of the different types of slow waves remain somewhat conservational, the consensus seems to suggest a vascular origin.[12,13]

Wave Type	Oscillation (waves/min)	Amplitude (mmHg)	Description
A	Variable	50 to 100	Also known as plateau waves
B	0.5 to 2	Baseline to 50	Most commonly used clinically
C	4 to 8	Baseline to 20	

Table 1: *Slow wave categories first described by Lundberg.[11] Similar table can be found in Lemaire et al.[14]*

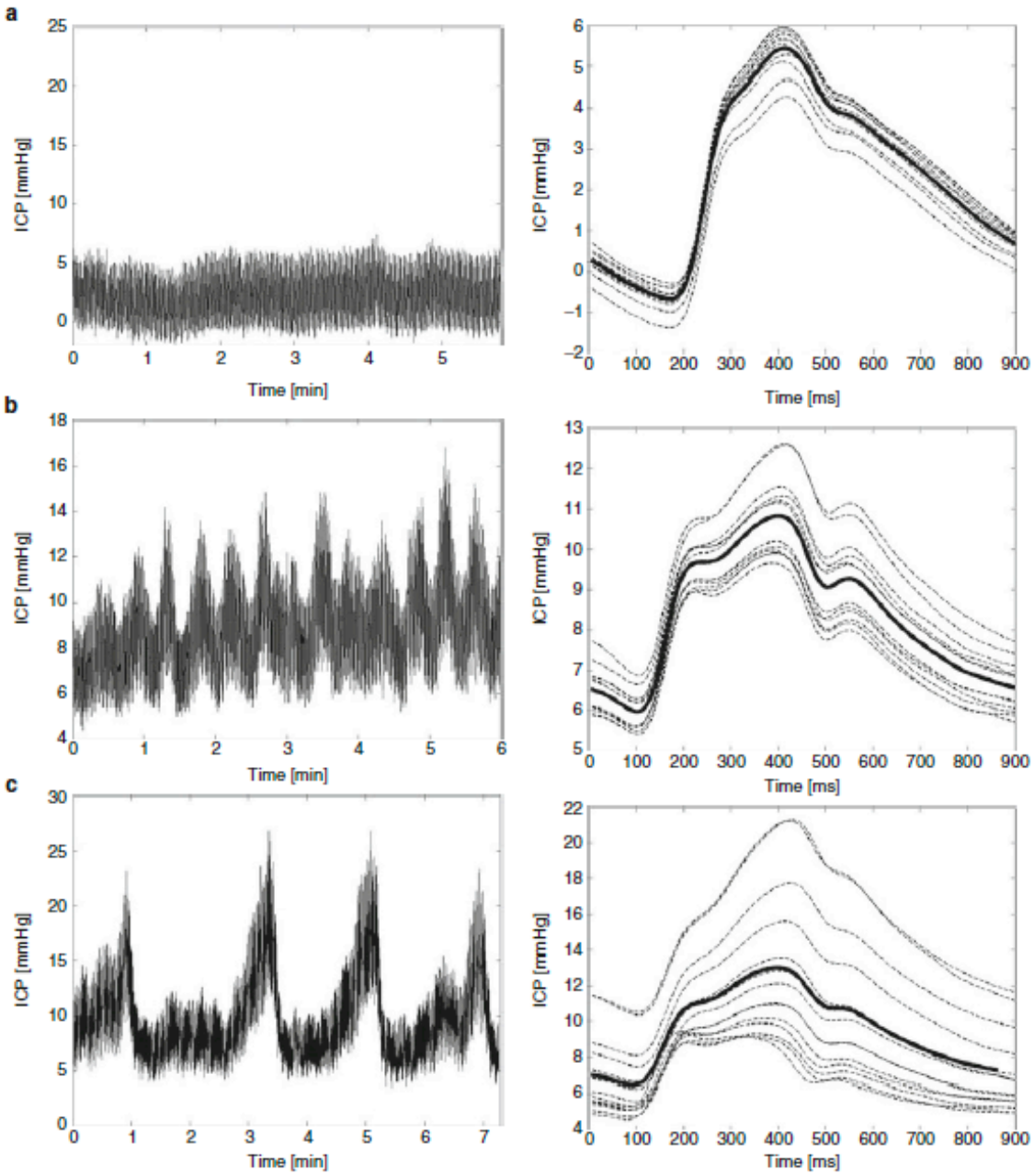

Figure 3: *Three examples of slow wave activity compared to ICP pulse pressure morphology. The figures on the left represent slow wave activity and the figures on the right are the corresponding ICP pulse pressure data. The thick black line represents the average pulse within the segment.* ***A)*** *No slow wave activity; note the low variability in the ICP pulse pressure waveform.* ***B)*** *Small symmetrical waves.* ***C)*** *Large asymmetrical waves. Both the small symmetrical and large asymmetrical waves are considered a subset of* Lundberg B-waves. *Reproduced with permission of Kasprowicz et al.*[15]

Clinically, the presence of B-waves has been tied to shunt responsiveness in patients with NPH;[16] however, the topic remains controversial.[17,18] Attempts have been made to extend slow wave analysis to other neurological conditions where increases in ICP could be pathological; these have not gained widespread acceptance because of substandard analysis techniques[19-22] and a lack of research into these other neurological conditions. Today, with the exception of a few centers, ICP slow wave analysis and interpretation remains a topic of research and not a part of clinical protocol.

b) ICP pulse pressure

In addition to slow wave activity, ICP has a cardiac-induced component known as the ICP pulse pressure waveform. The ICP pulse pressure waveform is driven by the increase in intracranial volume caused by the influx of arterial blood into the cranial vault. A visual depiction of the slow wave activity and ICP pulse pressure waveform are shown in **Figure 4**. For changes in the mean pressure, the ICP pulse pressure waveform changes in shape with the waveform rounding at higher mean values of ICP.[23-25] Shown in **Figure 5** is a progression of ICP morphology in adult cats with the placement of an epidural balloon to artificially increase ICP. Although this study was done in cats, the same morphological trend has been shown in humans.

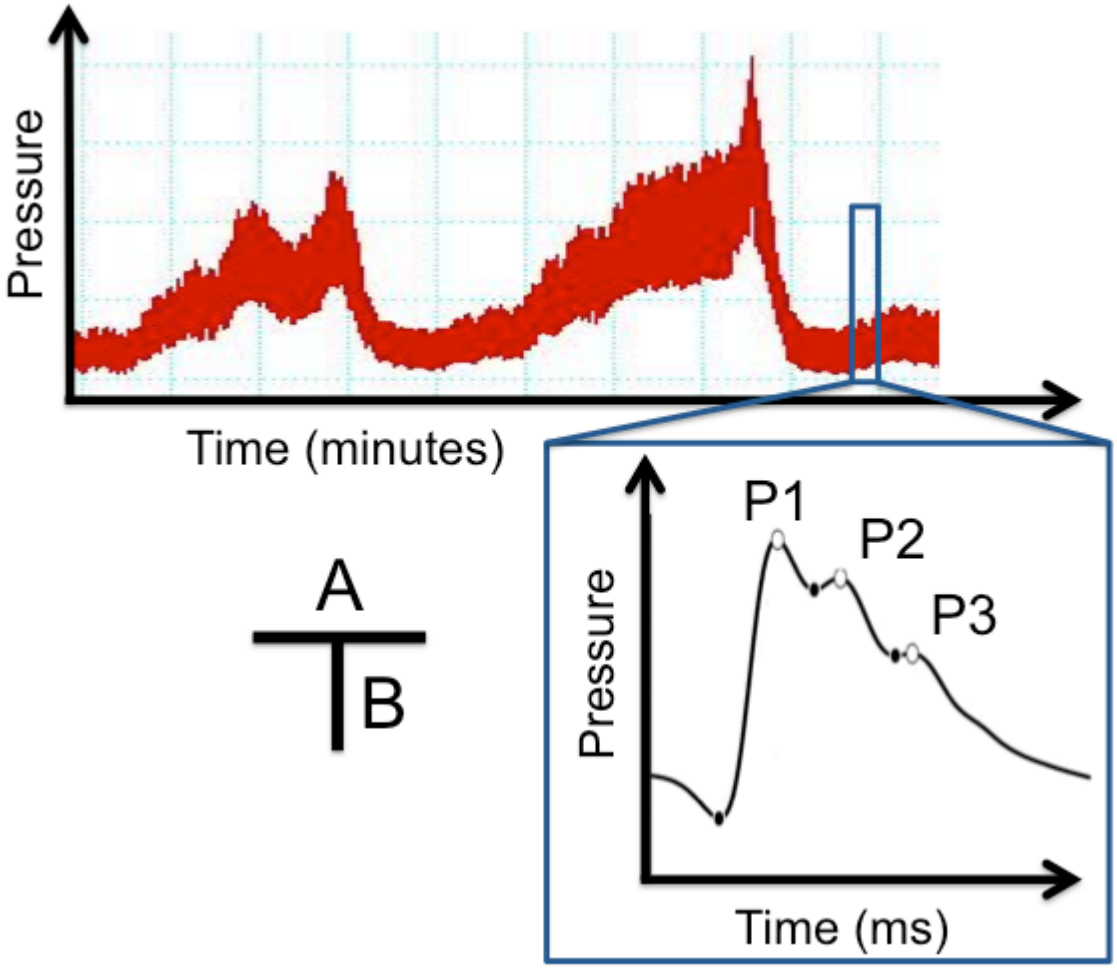

Figure 4: ***A)*** *Segment of slow waves over a 20-minute period with elevations in pressure between 10 mmHg and 40mmHg.* ***B)*** *The inset in blue shows one cardiac induced ICP pulse pressure waveform. The time frame is reduced to ms and amplitude of the individual waveform is approximately 5 mmHg. The three characteristic peaks (P1, P2, P3) are shown in the ICP pulse pressure peak.*

Despite the known trend toward a monotonic waveform for increasing pressure, there is surprisingly little evidence for the origins of the three characteristic peaks **(Figure 4B)**. Physiologically, the ICP pulsations have long been attributed to both arterial and venous components.[26,27] A number of studies have identified the subpeaks within the ICP waveform, and the origins of those subpeaks continue to be a focus of research.[26,28-31]

Adolph et al. used surgical interventions to differentiate arterial and venous contributions to the CSF pulsations in the cisterna magna.[29] The study concluded that although a majority of the CSF pulsations have the arterial system as an origin, there is a venous component. In later work, Cardoso et al. attributed the third peak (p3, or the dicrotic wave) to changes in venous pressure by using several interventions to perturb the ICP and then investigating the resulting morphologic changes in waveform.[28]

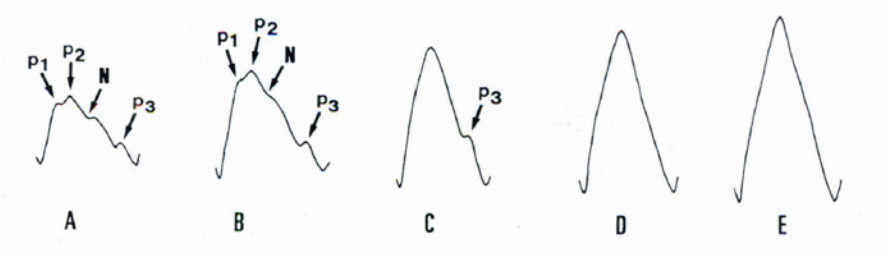

Figure 5: Trending of increasing mean ICP and the impact on the ICP pulse pressure waveform morphology in adult cats*. Reproduced from Hirai et al.*[26]

The study of ICP and ICP-related research is vast and ever expanding; additional topics include cerebral perfusion pressure (CPP),[6] cerebral autoregulation,[6,32] and cerebral compliance (compensatory reserve).[6,32] The topic of brain pulsatility is complex and a majority of the details are outside the scope of this thesis; for a detailed review of brain pulsatility, see Wagshul et al.[33]

C. Measurement Modalities

1. ICP Monitoring

As described above, the cranial vault provides a unique physiologic environment compared to other organ systems. There is level 2 evidence to support the use of ICP monitoring in patients with traumatic brain injury (TBI) that presents with hematomas, contusions, and cerebral edema.[34] ICP monitoring has also been used extensively in the care of subarachnoid hemorrhage (SAH) and other conditions where increased

intracranial volume (ICV) is a concern, including NPH and idiopathic intracranial hypertension (IIH). Methods for monitoring ICP include epidural, subarachnoid, and intraparenchymal pressure probes; however, the intraventricular probe remains the "gold standard" (**Figure 6**).[35] ICP monitoring is not without risk; infection and hemorrhage due to probe placement are commonly cited concerns.[36]

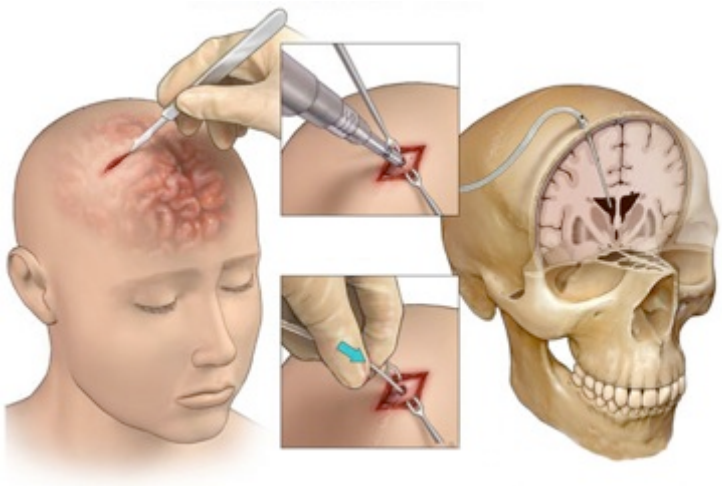

Figure 6: *Surgical diagram of the intraventricular catheter. Reproduced with permission*

a) ICP Advanced Analysis

Mean ICP remains the only feature of ICP that has gained widespread clinical acceptance. However, a number of research groups are investigating advanced ICP analysis. Eide et al.[37] pioneered an approach to reliably extract additional features from an ICP waveform. The method utilizes a 6-second window to extract a variety of features, including temporal and amplitude metrics. Hu et al.[38] developed the Morphological Clustering and Analysis of Continuous Intracranial Pulse (MOCAIP) algorithm, which extracts 128 morphological features from the ICP waveform. MOCAIP, which will be explained in detail in Chapter 3, is used extensively in this thesis. A qualitative comparison between the features extract by Eide et al. and Hu et al.'s

algorithms is shown in **Figure 7**. Finally, a group from University of Cambridge led by Marek Czosnyka has changed the way many researchers and clinicians investigate ICP. Czosnyka and Smielewski developed a software package, ICM+,[39] which utilizes advanced features of ICP and other physiological signals, including arterial blood pressure, to extract additional meaningful features. These researchers have shown that extracting morphological features of ICP and multimodality monitoring can provide additional diagnostic and prognostic information for a number of neurologic conditions, including hydrocephalus,[22,40-46] TBI,[47-51] IIH,[52] and SAH.[47,53-56]

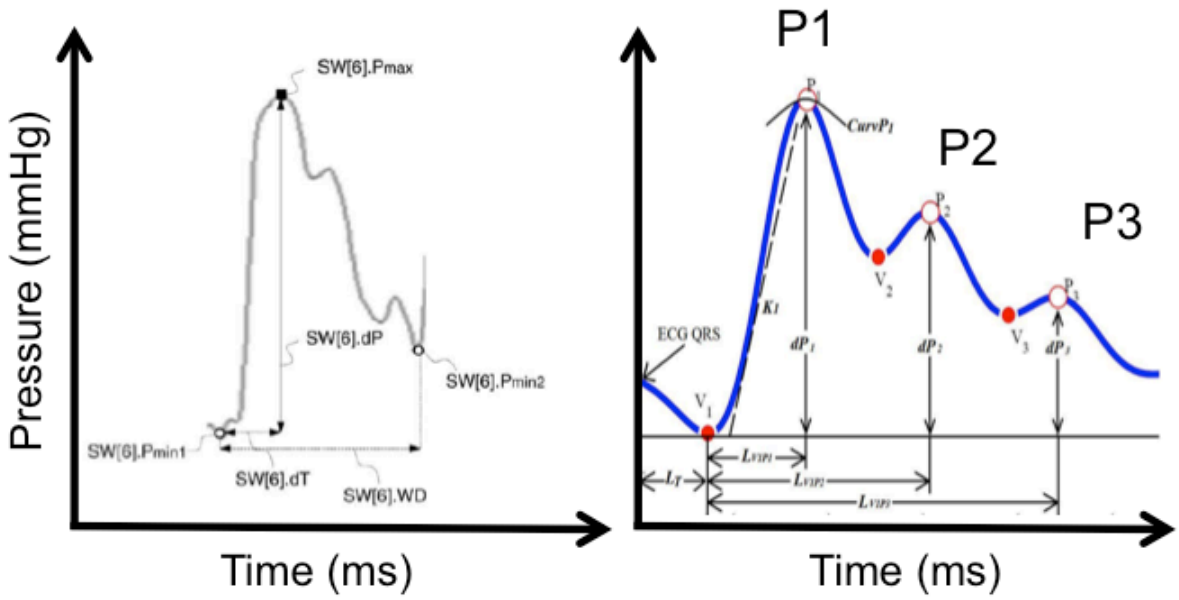

Figure 7: ***Left)*** *Eide et al.[37] representation of the ICP pulse pressure waveform and sample features.* ***Right)*** *Hu et al.[38] representation of the ICP pulse pressure waveform, created using MOCAIP. MOCAIP identifies the three subpeaks, where Eide et al. relies on the identification of the systolic peak.*

2. Magnetic Resonance Imaging (MRI)

The history of MRI has roots as far back as the first half of the 20th century and the technology continues to evolve. The applications of MRI extend much further than the

scope of this thesis; however, phase-contrast MRI (PC-MRI) is used extensively in this thesis and is explained in detail in Chapter 2.

D. Normal Pressure Hydrocephalus (NPH)

Comprehensive definitions of the pathoetiology of NPH remain elusive, despite having been first defined nearly half a century ago.[57] The traditional hypothesis, dating back more than 70 years to the work of Walter Dandy,[58] posits that CSF malabsorption at the level of the arachnoid granulations is responsible for the accumulation of CSF within the ventricles. Interestingly, several lines of evidence suggest that alternative mechanisms may be at play,[59-61] including the theory that interference of pulsatile CSF dynamics plays an important role.[62] NPH is a particular form of communicating hydrocephalus characterized by the presence of some combination of dementia, gait disturbance, and urinary incontinence along with radiological evidence of ventriculomegaly (**Figure 8**). There are two broad forms of NPH, secondary NPH, which develops following subarachnoid hemorrhage, infection, meningitis, or other head injury, and idiopathic normal pressure hydrocephalus (iNPH). Although many of the topics discussed here are applicable to both forms, iNPH will be the focus of this thesis. Diagnostic and effective treatment options for iNPH remain a difficult task for neurosurgeons due to the incomplete understandings of the pathophysiology of the disease and of the effect of treatment.

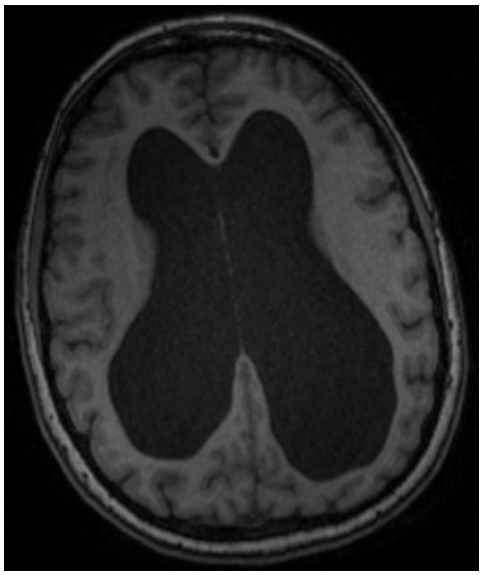

Figure 8: *Dilated lateral ventricles on a T1 axial image of an NPH patient.*

Altered CSF hydrodynamics remain the fundamental element in the pathophysiology of NPH. In addition to the obvious ventriculomegaly, other changes in CSF or CSF-related dynamics have been cited, including an increase in outflow resistance (reduced absorption),[63,64] increased aqueductal stroke volume,[65] changes in compliance of the cerebral vasculature[66,67] and subarachnoid space,[59,67,68] alteration of ICP slow wave activity,[16] and a reduction in cerebral blood flow.[59,66,67]

While shunting excess CSF from the ventricles remains the predominant treatment for NPH, this therapy faces a variety of issues. Shunt failure, infection rates, and over-drainage are significant concerns for clinicians and their patients, and the ability to differentiate who will and will not respond to treatment is a primary concern. Shunt failure rates have been reported as high as 40 percent within the first year and up to 81 percent within the first 12 years after implantation.[69-72] Furthermore, infection rates near

10 percent have been cited[73] and overdrainage symptoms reinforce the need for further research.

To aid in the identification of patients who are likely to respond to shunt, an array of both invasive and noninvasive diagnostic tests have been used, including radionuclide cisternography,[74] overnight ICP monitoring,[16,17,22,40-43,45,75] CSF tap test,[76-78] extended lumbar drainage (ELD),[45,68,79-81] CSF infusion (outflow resistance),[81-97] and CSF flow quantification with MRI.[65,98-101] Unfortunately, no gold standard has prevailed due to conflicting information and lack of understanding of the pathophysiology of NPH. However, based on a recent review, a panel of researchers and clinicians recommended the use of ELD (500 ml/3day) for differentiating patients most likely to respond to shunt; the panel also suggests that additional tests may be performed to increase accuracy.[102] This recommendation was supported by Marmarou et al.'s study on 151 NPH patients, which reported 92 percent sensitivity in differentiating shunt responders and nonresponders; this remains one of the most important recent papers on prognostic testing for NPH patients.[68] However, despite the evidence for ELD, as well as high economic cost (extended hospital stay) and increased risk to the patient (infection) associated with other methods, several institutions have implemented additional prognostic procedures to help identify likely shunt responders.

Overnight ICP monitoring is one example of a possible alternative or supplement to ELD. A majority of the prognostic literature for overnight ICP monitoring has focused on the slow wave activity characterized by Lundberg in the early 1960s.[11] Despite some

early positive results that linked increased slow wave activity to positive shunt response,[16,43] other studies have shown no correlation.[17,18] In addition to investigations of slow wave activity, recent studies looking at the cardiac-induced ICP pulse pressure waveform (**Figure 4**) have shown promising results. Eide et al. compared mean ICP, ICP pulse amplitude (waveAmp), and other ICP metrics from overnight ICP recordings as possible prognostic features for NPH shunt outcome. Their study reported 98 percent sensitivity and 70 percent specificity based on average and percent time values for ICP pulse amplitude (waveAmp), where mean ICP reported much lower values for sensitivity and specificity.[43] This work was made possible by the group's in-house analysis algorithm, which extracted additional features from the ICP pulse pressure waveform.[37] Overnight ICP analysis to aid in shunt prediction, which will be a major theme in this thesis, is discussed in greater detail in Chapter 3.

E. Thesis Overview

The study of brain pulsatility, both invasive and noninvasive, and its role in the pathoetiology of NPH are at the foundation of this thesis. The following chapters are divided by modality. Chapter 2 describes the use of phase-contrast MRI to investigate alternative methods for evaluating NPH patients with the added goal of creating a greater understanding of CSF dynamics. Chapter 3 investigates novel ICP features for the prognosis of ELD outcome in NPH patients. Finally, Chapter 4 combines the modalities in an effort to gain a greater understanding of the relationship between pressure and flow within the cranial vault. **Figure 9** illustrates how the chapters are related.

F. Specific Aims

1. Determine the flow characteristics in the cerebral aqueduct and prepontine cistern in normal pressure hydrocephalus using phase-contrast MRI.
2. Determine predictive accuracy of advanced morphological ICP metrics in determining ELD outcome.
3. Elucidate relationship between intracranial pulse pressure and noninvasive measures of cerebral dynamics.

G. Contributions

1. Specific Aim 1

The contributions from the investigation of CSF dynamics in NPH patients are multifaceted. The worked confirmed that NPH patients have hyperdynamic flow in the aqueduct compared to age-matched controls. Although significance was not reached, I was able to show a decreased buffering capacity in the prepontine cistern which improved following shunting. In addition to the flow results significant changes were found in the temporal aspects of the prepontine cistern suggesting a decrease in cerebral compliance in NPH patients. Finally, a significant difference was found in the variability of flow in the prepontine cistern further suggesting altered CSF dynamics in NPH patients.

2. Specific Aim 2

The second study focused on applications of advanced ICP monitoring using the Morphological Clustering and Analysis of Continuous Intracranial Pulse (MOCAIP) toolbox to help differentiate shunt responders from non-responders by using ELD as a surrogate. The first application showed through the combination of multiple ICP metrics

using novel descriptive features is able to predict external lumbar drain (ELD) outcome. The second application introduced a novel ICP metric, P3Rato that has the promise to replace expensive and dangerous prognostic tests and has the added benefit of a physiologic basis.

3. Specific Aim 3

The final study focused on the relationship between the noninvasive measures of CSF dynamics and the invasive ICP pulse pressure waveform. Little is still known about the characteristic peaks of the ICP pulse pressure waveform. Using two studies I was able to associate regional and individual contributions of specific features of the ICP sub-peaks to CSF dynamics investigated by PC-MRI. The importance of this work car exceeds applications in NPH but lay the foundation for a much better understanding of the ICP waveform.

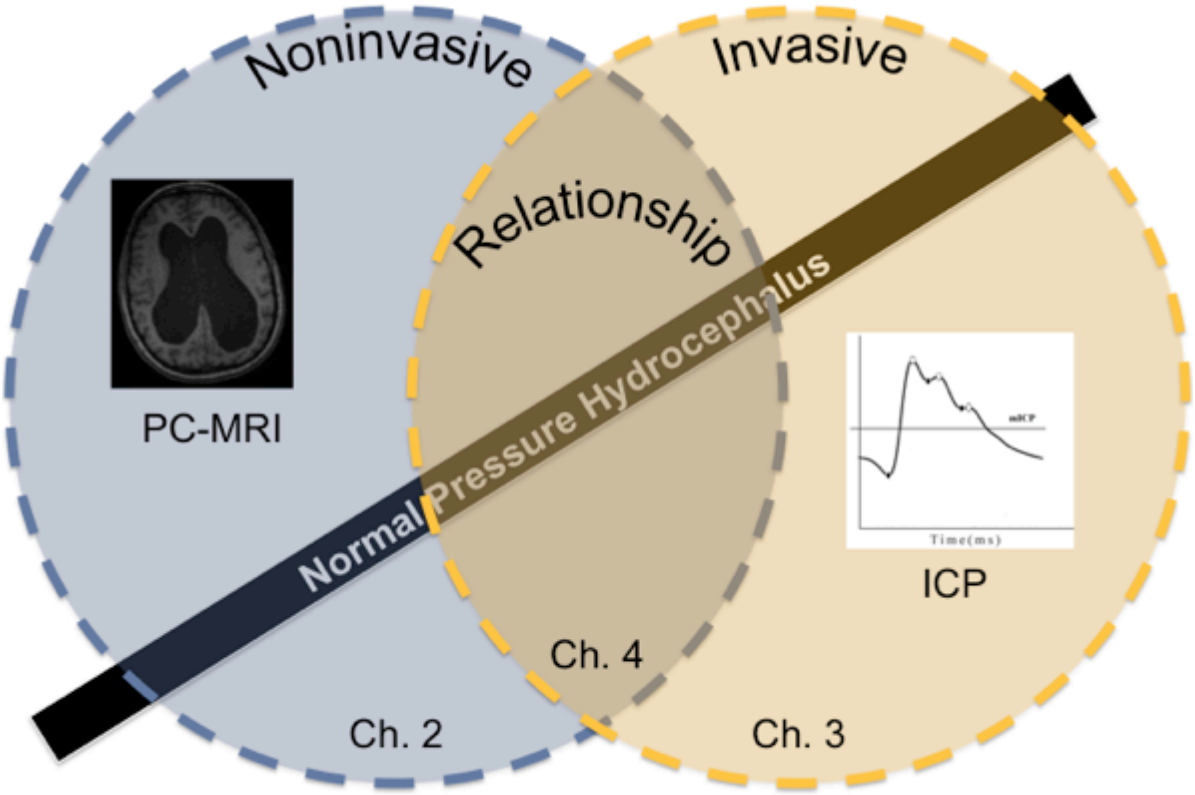

Figure 9: *Diagram showing the relationship between the monitoring modalities and the chapters in this thesis. Chapter 2 focuses on the MRI imaging and CSF flow. Chapter 3 explores the invasive ICP monitoring. Finally, Chapter 4 investigates the relationship between the two modalities. NPH is a central theme throughout the thesis and is represented in each chapter.*

V. Chapter 2

A. Introduction

Traditionally, NPH is characterized clinically by the presence of dementia, gait disturbance, and urinary incontinence, along with radiological evidence of ventriculomegaly.[103] Altered cerebrospinal fluid (CSF) dynamics have been at the center of normal pressure hydrocephalus (NPH) research since initially described over 70 years ago.[58] The study of CSF dynamics has evolved in parallel with technological advancements in imaging modalities and surgical techniques. There are three methods for measuring intracranial pulsatility: invasive intracranial pressure (ICP) monitoring, phase-contrast MRI (PC-MRI), and transcranial Doppler (TCD).[33] In this chapter we will focus on MRI's ability to quantify the pulsatility of CSF within the cranial vault.

1. Magnetic Resonance Imaging

Magnetic resonance imaging (MRI) is a noninvasive imaging modality that provides superior contrast of soft tissue while using non-ionizing radiation. Coupling these properties with the versatility of the specialized sequences provides researchers and clinicians with an invaluable tool for the diagnosis, treatment, and prognosis of numerous diseases and conditions. Cine Phase-Contrast MRI (PC-MRI), which was first described in the early 1980s,[104] is a specialized imaging sequence used for the characterization of fluid flow. Contrary to what the name implies, PC-MRI does not use a contrast agent; the images produced are based on phase differences of individual protons following the application of magnetic gradients. **Figure 1** provides a schematic of the process by which PC-MRI provides flow information. In short, there are equal and opposite magnetic gradients applied to a given tissue. If the tissue is static, or nearly

static like brain parenchyma, the phase offset of the magnetic moment of the proton will be unaffected. If the protons are moving through the imaging plane (within a vessel or other structure), there will be a net increase or decrease in the phase-offset, which is proportional to the velocity. The impact of the phase-encoding sequence is a phase image commonly gated with the heart rate (ECG) of the patient. It is important to note unlike real-time (ICP and TCD) methods for measuring or visualizing flow, PC-MRI is an averages over several cardiac cycles, producing an average representative waveform.[33] **Figure 2** provides an example of selected frames from a phase image of the cerebral aqueduct. Lotz et al. provides a more complete description of the physics of PC-MRI if interested.[105]

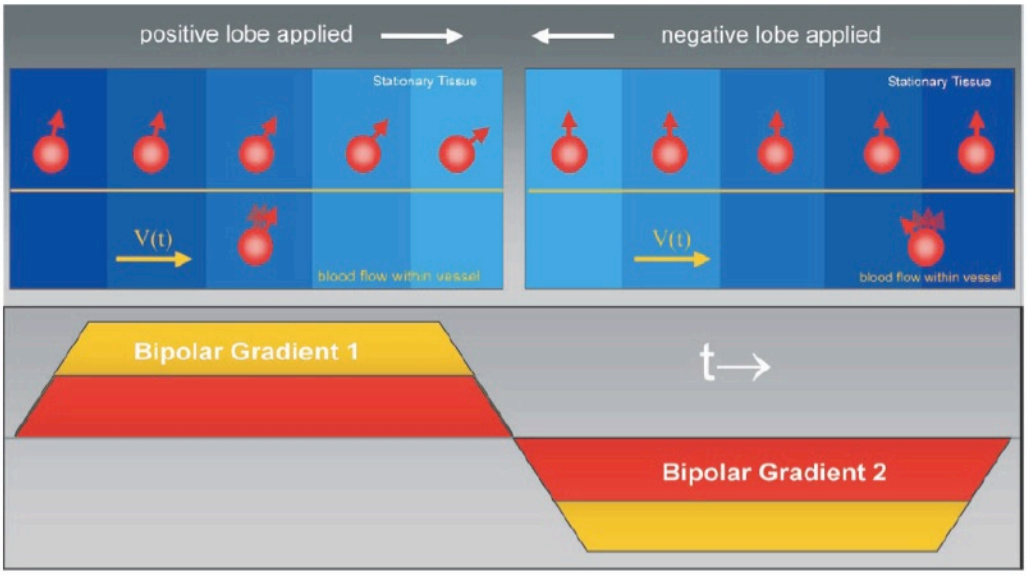

Figure 1: *An image depicting the principles of phase-contrast MRI. The image shows the impact of equal and opposite magnetic gradients (bottom) applied to a single proton while stationary and with some velocity. Image taken from Lotz et al.*[105]

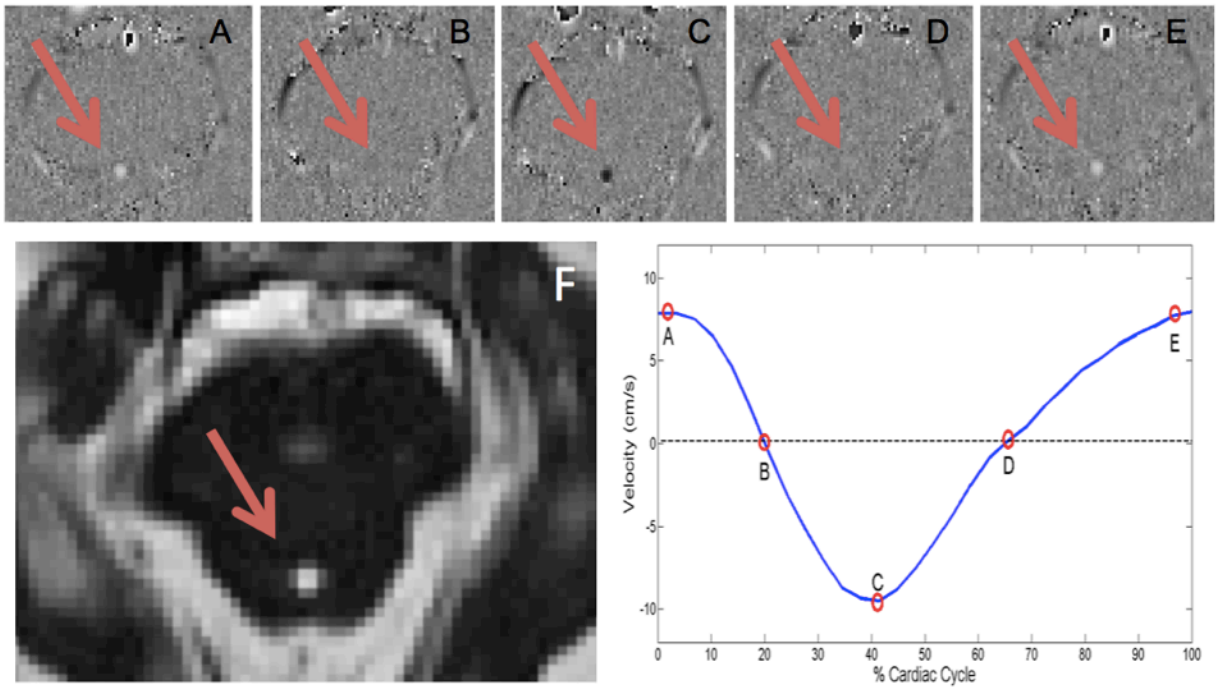

Figure 2: *Several images depicting phase-contrast imaging (PC-MRI).* ***A-E)*** *are time points within the phase image of the sequence (five out of the 30 total images). The red arrows in images* ***A-F*** *point toward the cerebral aqueduct.* ***F)*** *is the TrueFISP image, which visualizes the CSF as hyperintense. Finally, the waveform plot shows the time series of CSF flow within the cerebral aqueduct. The dotted line represents zero flow and thus appears equal to the static tissue in images* ***B*** *and* ***D****.*

Clinically, PC-MRI is used to quantify of blood flow throughout the body,[106] but has also been utilized in the quantification of CSF within the cranial vault, which will be the focus of this thesis.[107-110] With regards to CSF dynamics, PC-MRI is being investigated for the possible use in the diagnosis and treatment of hydrocephalus and chiari malformation along with noninvasive measurements of elastance and intracranial pressure.[111-114]

2. PC-MRI and NPH

The CSF dynamics within the cranial vault are comprised of two different types of movements, the pulsatile flow within each cardiac cycle, and the slower bulk flow movement of CSF from the choroid plexus to the arachnoid granulations, each receiving a great deal attention over the last 20 years with respect to NPH. Despite the extensive

study of CSF dynamics, there remains conflicting evidence of its efficacy in predicting of shunt response within the NPH population (the lone treatment for NPH). Early studies cite relatively qualitative metrics for the diagnosis or prediction of shunt response. Black reported mixed results from his cohort of NPH patients based on the presence of the classic triad, radiological evidence, and cisternographic evidence.[115] In the early 1990s Bradley et al. correlated shunt outcome to the presence of flow void in the third and fourth ventricles;[116] however, this method is highly dependent on the parameters of the sequence (TR, TE, etc.) and the strength of the magnetic and gradients used. With the development of phase sensitive imaging (PC-MRI), many of the issues related to reproducibility and subjectivity of flow voids were addressed.

PC-MRI has been at the foundation of hemodynamic CSF studies on patients with NPH. Studies have traditionally focused on measuring stroke volume, [65,98,117] flow,[98] and peak velocity[118] within the cerebral aqueduct to investigate their potential impact on the diagnosis and/or prognosis of NPH; however, as previously mentioned, these studies have been met with mixed results. A threshold for aqueductal stroke volume (ASV) was first set by Bradley et al. at 42 microL, suggesting that patients exceeding this threshold would show improvement following shunting.[65] Conflicting results by other groups suggest that stroke volume alone is insufficient for differentiating shunt responders from non-responders.[98,117] Other groups have extended the use of PC-MRI to the quantification of CSF dynamics in additional locations, including the subarachnoid space at the C2-C3 junction[106,119] and prepontine cistern[106,119,120] to better understand the relationship between the ventricular system and the subarachnoid space. Studies by

Balédent et al. reported similar results (SV) at the level of C2-C3 and significant differences in the aqueduct, producing a difference in stroke volume ratio between the hydrocephalic group and the healthy controls.[106] Another report only investigated healthy controls but established a stroke volume ratio of 5.1 ± 1.8 percent and reported significant differences in phase lag between several areas in the subarachnoid space and ventricular system.[121] Both of these studies align well with a proposed model by Egnor et al. In this model, Egnor describes impedance changes within the cranial vault impacting changes in both amplitude and latency metrics [62]. Furthermore, he describes the etiology of communicating hydrocephalus (CH) in as an asymmetrical change in impedance between the ventricular system and the subarachnoid space. The work presented in this thesis expands on the aforementioned work by including pre- and post- shunt NPH patients to investigate changes in amplitude, latency, and variability metrics of the aqueduct and prepontine cistern.

3. Segmentation

Although a majority of the work presented in this chapter revolves around clinical studies of NPH and CSF flow, the technical limitations involved in analyzing the PC-MRI images are not trivial. The pulsatile movement of CSF in the basal cisterns may play an important role in the pathogenesis of so-called “communicating” hydrocephalus. Contrary to the basal cistern, the flow of CSF within the cerebral aqueduct and its potential impact on the diagnosis and/or treatment of hydrocephalus has been extensively studied.[65,98,122,123] We hypothesized that the increase in ventricular displacement of CSF during systole is due to a reduction in cisternal CSF volume buffering. Unfortunately, the quantitative measurement of this parameter presents

considerable technical challenges. Imaging the subarachnoid space (prepontine cistern) adds a level of complexity that is not found in the cerebral aqueduct. The prepontine cistern contains a complex system of connective tissues (trabeculae), cranial nerves, venous and arterial blood flow, and CSF. Various methods were attempted for defining the cisternal region of interest; visual segmentation proved to be too subjective and previously published pulsatile-based segmentation algorithms generated noisy results.[124] Therefore, an imaging segmentation algorithm needed to be developed which would adequately accommodate the low-flow velocity and complex anatomy of the prepontine cistern and provide equally reliable results in the cerebral aqueduct.

In this chapter, I discuss my investigation of several aspects of CSF pulsatility via PC-MRI, including volumetric/flow metrics, temporal-based latency metrics, and flow variability within the cerebral aqueduct and prepontine cistern. Accurate segmentation of the PC-MRI signal is essential for the remaining physiological studies and will be addressed first. Following the segmentation, I investigated individual hypothesizes relating to the pathoetiology of NPH described below.

4. Chapter Objectives

a) Study 1

For the volumetric and flow studies I hypothesized that CH arises primarily from an interference of either cisternal or other subarachnoid CSF pulsatile movement, with the result being a decrease in CSF cisternal pulsatility compared with the hyperdynamic aqueductal flow commonly shown for NPH patients. In some respects, this concept is not too different from the Dandy traditional theory except that the putative point of

"obstruction" to CSF flow is "upstream" from the arachnoid granulations, and related primarily to pulsatile movement rather than solely on bulk CSF flow.[58] We reasoned that a reduction in cisternal and/or subarachnoid CSF volume buffering would have to be compensated for by an increase in ventricular buffering – thereby producing aberration in intracranial pulsatile CSF dynamics described by Bradley[116] and others. In addition, the notion of "scarring" of the cisternal spaces is well known to neurosurgeons who perform endoscopic third ventriculostomies (ETV) for hydrocephalus, as it has been associated with unfavorable outcome.

The treatment of CH typically entails the implantation of a CSF "shunt," a diversionary system that allows CSF flow through a catheter from the ventricle to either the peritoneum or atrium of the heart. In the pulsatile CSF dynamics realm, a CSF shunt offers an alternative pathway for CSF volume buffering. We therefore further hypothesized that successful implantation of a CSF shunt in a hydrocephalic patient would result in a movement of both the aqueductal and cisternal SV values toward normal values.

b) Study 2

The second study investigated the temporal aspects of cisternal CSF flow. Egnor et al. published a model for CH that suggested the increase in ventricular pulsatility (causing ventriculomegaly) was a result of increased impedance in the SAS.[62] This idea did not develop exclusively from theoretical machinations, but rather as a result of trying to explain a well-established observation in NPH: that the CSF stroke volume through the cerebral aqueduct of Sylvius is markedly elevated in NPH.[65,98,125] This change in

impedance suggests altered transit times for the arterial pulse pressure waveform, thus altering the peak flow of the CSF movement. The hypothesis is that NPH CSF peak flow latencies (time to peak flow) are shorter in NPH patients than in age-matched controls.

c) Study 3

Study 1 suggests that cisternal scarring in NPH patients will lead to a decreased cisternal CSF stroke volume. In addition to the possible decrease in stroke volume we hypothesize that the presence of scarring will lead to a greater variability in flow distribution in NPH patients compared to age-matched controls.

B. Methods

1. Patient Population

The following studies have a common patient dataset. While under evaluation at UCLA Adult Hydrocephalus Clinic, patients were enrolled in the PC-MRI study to quantify CSF flow. The local IRB committee approved all imaging and procedures and written consent was provided by both patients and controls prior to the imaging (10-001128, 06-11-013, and 07-08-038). Scans were conducted on 30 pre-treatment patients (77.8 ± 7.1 years, 19 males and 11 females) ranging in age from 58 to 88 years old, and 12 controls (66.3 ± 9.2 years, seven males and five females). Additionally, 12 patients ranging in age from 74 to 89 years (81.7 ± 4.6 years) received scans following either ventriculoatrial (VA) or ventriculoperitoneal (VP) shunt treatment (nine VP, three VA), with a mean follow up time of six months. Of the 12 follow up scans there were nine matched pre-post aqueduct scans and six matched cisternal scans.

All MRI scans were performed using a 3T Siemens Trio T-class MRI (Sienmens Medical Systems, Erlanger, Germany). The participants were placed in the supine position with neck and head in the neutral position using a Siemens Head Matrix coil. All participants received the same imaging protocol, starting with anatomical sequences: a 3D axial T1-weighted MPRage, axial T2-weighted BLADE, and a sagittal T2-weighted TSE. Imaging parameters are shown in **Table 1**.

Sequence	TR (ms)	TE (ms)	Resolution (mm)	Slice thickness (mm)
3D axial T1-weighted MPRage	1900	3.44	0.844	0.9
Axial T2-weighted BLADE	7110	107	0.573	3.0
Sagittal T2-weighted TSE	750.0	100	0.344	8.0
TrueFISP	5.36	2.36	0.625	3.0
Phase contrast sequence	39.1	6.01	0.625	3.0
Time-of-Flight	24.0	3.69	0.780	0.8

Table 1: MRI sequence parameters

Flow quantification was achieved using a series of imaging sequences including localization, anatomical, velocity estimation, and phase contrast. Using a midsagittal slice, an oblique plane was defined perpendicular to the presumed direction of CSF flow for both the cerebral aqueduct and prepontine cistern (**Figure 3**). A trueFISP sequence was used to visualize the local anatomy of the oblique slice; CSF appears as hyperintense because its contrast is determined by T2*. A flow scout sequence was utilized to aid in the definition of the velocity encoding parameter (V_{enc}) for the phase contrast sequence. Following the definition of the V_{enc}, the phase contrast sequence was applied; to ensure its accuracy, the results were checked for aliasing and further adjustments to the V_{enc} were made, when necessary. Due to additional noise from arterial blood flow (Basilar Artery, see **Figure 9**) in the phase images of the prepontine

cistern, a Time-of-Flight sequence was used to aid in the segmentation. The PC-MRI sequence was retrospectively gated with either ECG or pulse oximetry, with a temporal resolution of 30 frames. Within the study cohort, the inter-patient velocity parameter varied drastically ranging from 8 to 30 cm/s for the aqueduct and 3 to 25cm/s in the prepontine cistern. The V_{enc} is an essential part of the process as studies have shown the sensitivity of PC-MRI to the V_{enc}.

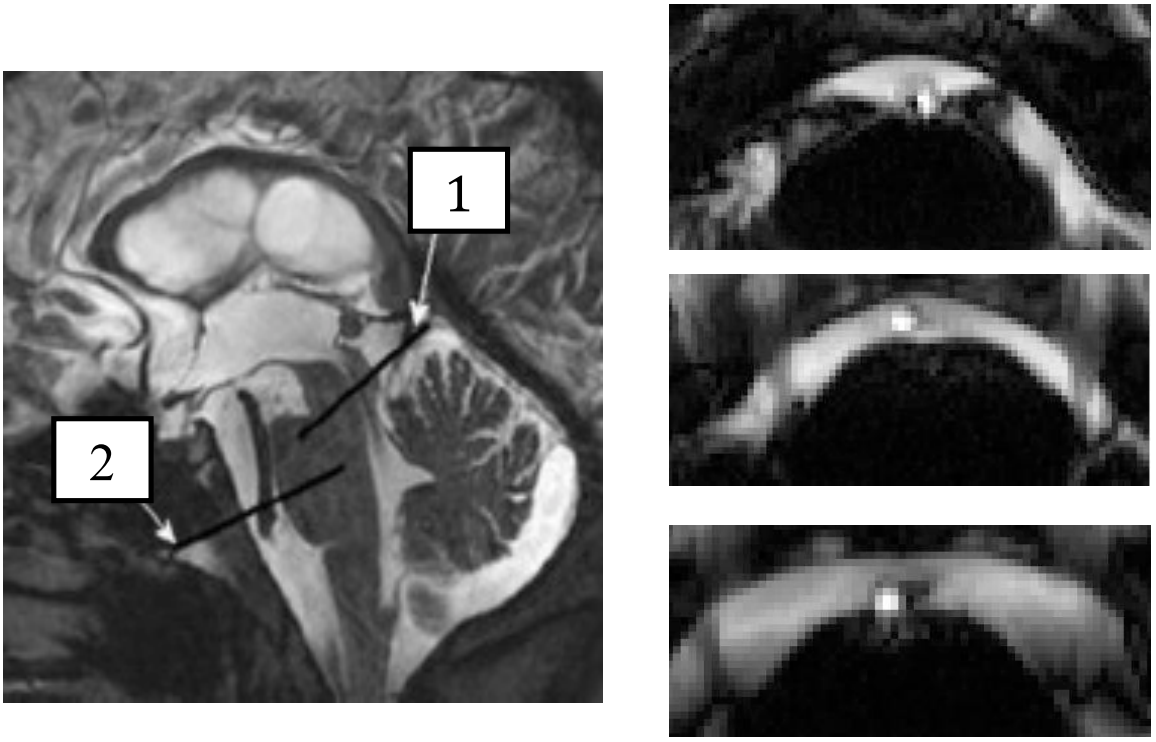

Figure 3: Left) Midsagittal T2-weighted image, flow acquisition planes for **1)** cerebral aqueduct and **2)** prepontine cistern. Planes defined perpendicular to CSF flow. **Right)** Example of prepontine cistern (T2 TruFisp) for three different pre-treatment NPH patients in the oblique plane perpendicular to CSF flow quantification.

2. Segmentation

The following is a detailed description of the segmentation algorithm for the region of interest (ROI) in the PC-MRI studies. An overview of the algorithm is shown in **Figure 4**.

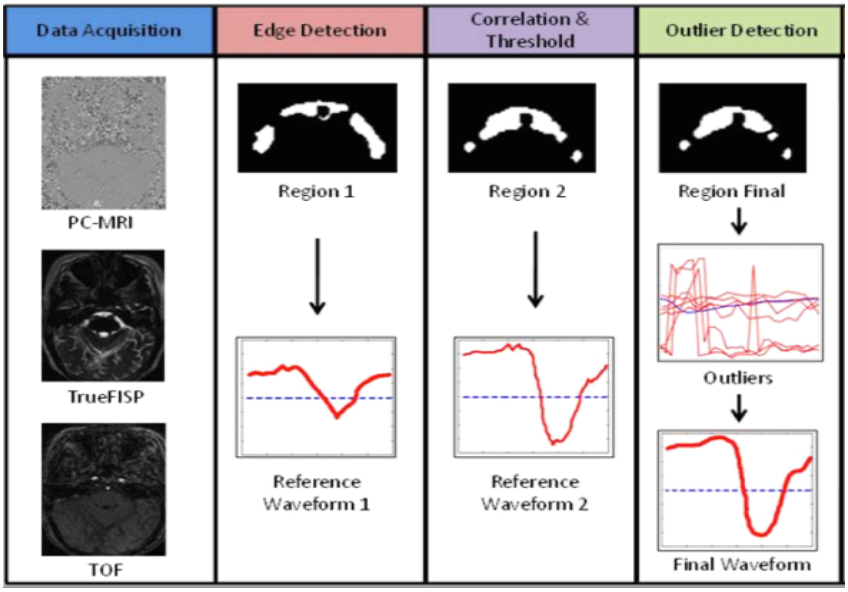

Figure 4: *Shows an overview of the segmentation algorithm. Specific MRI sequences are required for the segmentation of the ROI, including a phase contrast image, an anatomical sequence (TrueFISP) and the blood vessel information in the Time-of-Flight. Step 1) Reference Waveform generation using the anatomical information. Step 2) Incorporates the pulsatile information of the CSF flow. Step 3) is outlier detection and removal.*

a) Step 1: Reference Waveform

In contrast to current segmentation algorithms in which a seed point or manual ROI is defined,[124] I utilized the information from the local anatomy to define the initial seed point, which was fully automated. A standard edge detection algorithm converts the hypertensive CSF to a binary mask. This binary mask ($Region_1$) is used to define the initial reference waveform (W1). Applying the binary mask to the PC-MRI sequence and averaging the voxel intensity over the 30 time frames, which represents the entire cardiac cycle, constructs the reference waveform. This method removes the subjectivity

in manually selecting seed points, which are commonly used in other segmentation algorithms.[124]

b) Step 2: Correlation Mask and Threshold

In step 1, $Region_1$ was based solely on anatomical information. It has been shown, however, that manual segmentation based on anatomy alone produces results that are both inaccurate and difficult to reproduce.[124] Incorporating pulsatility information (flow information) into the segmentation process increases the overall accuracy of the segmentation and therefore the results from the flow quantification.[124] To do this, the reference waveform (W1) constructed from $Region_1$ is correlated with each individual voxel of the PC-MRI sequence using **equation 1**:

$$R(i,j) = \frac{C(i,j)}{\sqrt{C(i,i)C(j,j)}} [1]$$

in which R is a matrix of correlation coefficients and C represents the covariance matrix between the given elements. In this example *i* and *j* represent the voxel waveform (constructed from the 30 time frames) of the reference waveform (W1) and the waveform of the given voxel, respectively. From the correlation values in R a correlation map is created (**Figure 5**).

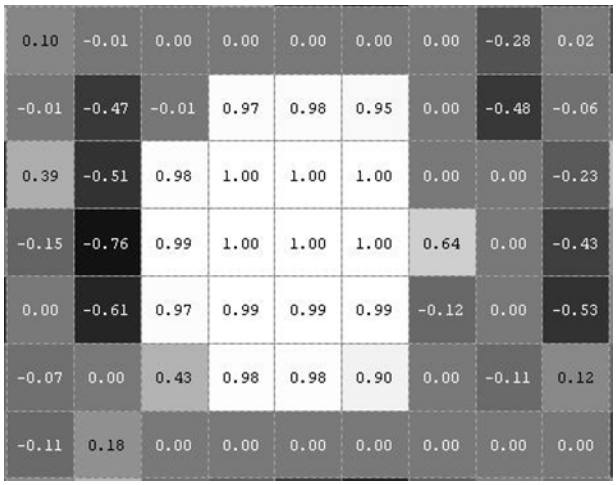

Figure 5: *A section of the correlation map created when comparing the reference waveform (W1) to the corresponding voxel waveform for the cerebral aqueduct. A threshold value is used to segment the voxels within the ROI.*

Once the correlation map is constructed, a threshold must be determined to remove "uncorrelated" voxels (values less than the threshold are removed). The threshold value of 0.5 has been used in similar segmentation algorithms validated by phantom experiments;[124] however, this "one-size-fits-all" approach produces inconsistent results. Therefore, the threshold was determined semi-automatically based on threshold plots for the individual study, which were constructed by plotting the number of voxels included in the ROI for a given threshold value (**Figure 6**). For example, a low threshold value (Pearson's correlation coefficient) will produce a large number of voxels within the ROI because a majority of the voxels within the image are above the given threshold and vice versa. At some point in the graph, a plateau region (**Figure 6**) will form where for increasing thresholds there are no additional voxels removed from the ROI (again, for increasing thresholds there are a decreasing number of voxels within the ROI). A plateau region is defined by a specific segment of the threshold plot that is unchanged for increased threshold value. Anatomically this area represents the luman border. Any threshold selected within the plateau region will have the same effect on the ROI.

Figure 6 shows an example of two different threshold values; the threshold value is selected as the lowest threshold value within the plateau region.

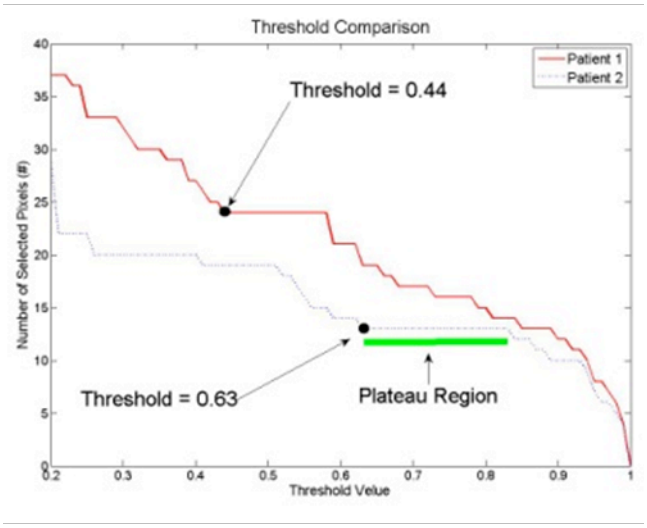

Figure 6: *Threshold plot, highlighting the difference in threshold values. The curves are constructed by iteratively decreasing the threshold value and plotting the number of pixels in the resultant ROI. The threshold is determined by the "plateau region," where a slight decrease in threshold increases the size of the ROI dramatically.*

The impacts of the threshold value along with the V_{enc} are discussed later. Unlike in other automated segmentation algorithms,[124] a boundary is not created, the final ROI is comprised of the voxels selected through the correlation process; $Region_2$ is then defined by the selection of the given voxels. The new reference waveform (W2) is established using the aforementioned method. The new reference waveform provides additional information reducing the influence of noise on the ROI.

c) Step 3: Outlier detection

Figure 9 shows that even though anatomical and pulsatility information has been incorporated within $Region_2$, poorly selected voxels remain (in this case the "noise" is from the influence of the basilar artery shown in **Figure 7**). Due to the complex structure of the prepontine cistern relative to the cerebral aqueduct, a method was developed to

identify these outlying voxels and remove them from the final segmented region. Using W2, defined by the pulsatility based $Region_2$, a new correlation map is computed comparing W2 to each voxel within $Region_2$. It is important to note the difference between steps 2 and 3; in step 2, the reference waveform (W1) is compared to each individual time-series waveform within the **entire image**. In step 3, the new reference waveform (W2) is only compared to the voxels within $Region_2$. Once this correlation is computed via equation 1, a new intermediate region is created. Due to the sensitivity of this process (equation 1) to the reference waveform, input is repeated iteratively until the region is unchanged by the new correlation map and thresholding (thereby producing the same reference waveform as the previous step); this final region is denoted $Region_{FINAL}$.

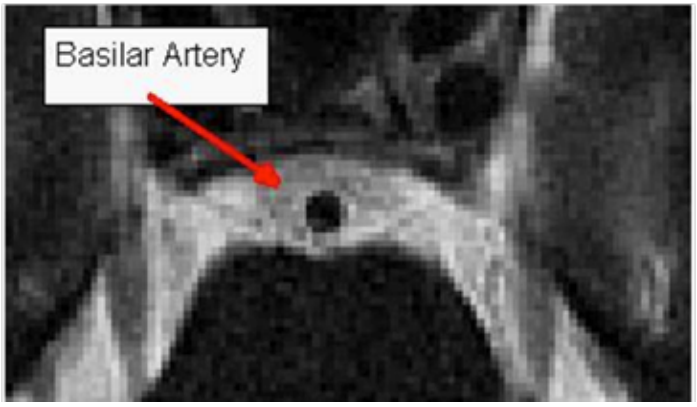

Figure 7: A T2- weighted axial MRI image of the prepontine cistern (white) surrounding the basilar artery (black).

d) Step 4: Results correction

Prior to calculating these metrics, a phase correction was made to offset accumulated phase or eddy currents due in part to the position of the patient in the scanner and to the intrinsic properties of the magnet.

Phase offset – The “piston-like” movement of the brain throughout the cardiac cycle caused by the change in intracranial blood volume can impact the calculations made using the segmented ROI ($Rigion_{FINAL}$). Therefore, a region within the midbrain assumed to have minimal displacement was selected automatically and an offset value was calculated from average velocity (of the “static tissue”) over the cardiac cycle; this value was used to correct for the periodic brain motion.

3. Cerebral Dynamics

Following the calculation of the ROI, various studies were performed on the segmented data.

a) Velocity, Flow, and Stroke Volume

Following the determination of the ROI, several CSF hydrodynamic metrics are derived from the PC-MRI sequence. The metrics are broken down into three categories: velocity, flow, and stroke volume. The velocity (cm/s) metrics are derived from the intensity waveforms obtained from the PC-MRI sequence after correction of the V_{enc}. The metrics reported include both max velocity and mean velocity. The max (peak) velocity and mean velocity metrics are reported for both the caudal and cranial directions. Flow (mL/min) results are computed on a voxel-by-voxel basis, by incorporating the pixel area and integrating over the ROI. Bradley et al. defined aqueductal stroke volume (ASV) as the average of the volume of CSF moving cranio-caudal direction and the caudo-cranial direction;[65] this is in comparison to Bateman et al., who defined the SV as area between the baseline (zero flow) and the peak portion of the flow curve.[126] In practice, these values should be approximately equal due to the

near zero bulk flow throughout the cardiac cycle; however, only values based on Bradley's definition will be reported. Finally, the ROI area was calculated by the summation of the voxels within the ROI.

b) Latency

Peak Flow Latency (PFL) is defined as the percent of the cardiac cycle at peak caudal CSF flow in the cerebral aqueduct and prepontine cistern. Following the calculation of the ROI, several additional steps are needed to reliably calculate the PFL. First, due to the influence of partial voluming, the ROI boundary voxels are removed to increase the signal (flow) to noise ratio. Second, the remaining voxel's temporal waveforms are averaged to produce an intermediate reference waveform (this is the "characteristic flow" within the reduced ROI). The third step is much more applicable in the prepontine cistern than is the homogenous flow of the cerebral aqueduct; the intermediate reference waveform is correlated (Pearson's correlation, **equation 1**) with each voxel in the reduced ROI. Based on this correlation value, the top 25 percent of highly correlated voxels are averaged to represent the final reference waveform (75 percent of the voxels are removed). The new reference waveform's temporal resolution is limited to the PC-MRI imaging parameters, which is 30 samples. Therefore, the final step in the calculation of the PFL is the fitting of a six-degree polynomial to the final reference waveform, which increases the temporal resolution from 30 to 1000 samples per cardiac cycle (selection of the six degree polynomial is discussed later). The PFL latency is defined as the percent of the cardiac cycle at peak caudal CSF flow, which is the minimum of this waveform. For the PFL to be comparable to those patients whose MRI was gated, ECG was used.

c) Variability

Flow variability is the final concept that will be explored pertaining to CSF dynamics. Based on the observation that cisternal scaring can lead to an unfavorable outcome, we investigated the variability of flow within the prepontine cistern. Within an unobstructed environment, laminar flow should be approximately parabolic in shape, with peak velocity/flow near the center of the structure. Obstructions will cause disruptions within the flow profile, causing an increase in flow variability.

Region segmentation and flow calculations were computed in Part 1 of the methods. Using this computation as a baseline, we are able to investigate the variability in the distribution.

(1) Waveform Clustering

The prepontine cistern represents a much more complicated flow profile than the cerebral aqueduct (**Figure 3**). For this reason the flow profiles of each individual voxel were organized into three clusters using k-means in MATLAB 7.5 R2007b functions. In a system with parabolic flow we would expect to find three concentric flow regions.

(2) Distance Calculation

To quantify variability a metric must first be calculated. While the clustering of the flow waveforms incorporates the dynamic information, the distance between the individual voxels within each cluster incorporates the spatial information of the anatomy. The pairwise distances were calculated for the intra-cluster sets using the voxel locations as the inputs because the voxel size is constant for all participants ($0.625mm^2$). Following the calculations for each cluster the distances were combined to form one distribution.

(3) Simulation Data

A ground truth distribution is needed for comparison between the control and pre-treatment NPH patients. This simulation set was built using idealized anatomical structure and flow patterns (**Figure 8A**). Following the construction of the simulation ground truth dataset, steps a-c were calculated to produce a model distribution for comparison (**Figure 8C**).

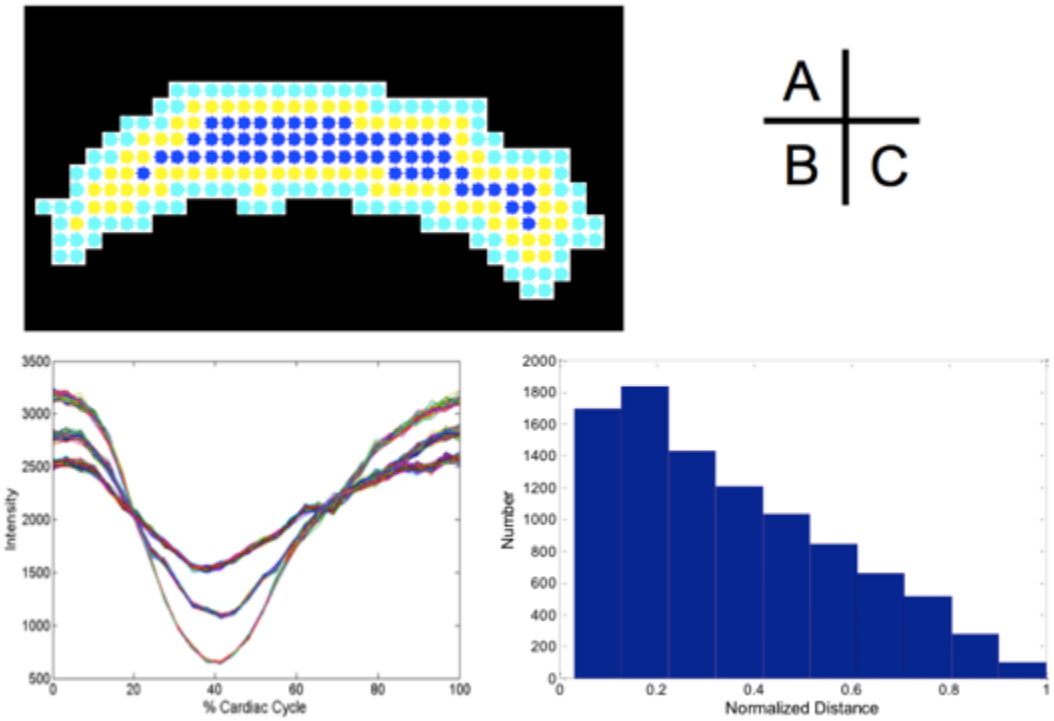

Figure 8: A) *Binary mask of the simulated cisternal flow pattern. The different color voxels represent three simulated flow waveform patterns.* ***B)*** *The waveform patterns from the simulated dataset. Note that there are three distinct waveform shapes; random noise was added to each signal.* ***C)*** *Histogram for the normalized distance distribution for the simulated dataset.*

(4) Distribution Comparison (Kullback–Leibler Divergence)

The Kullback-Leibler Divergence (KL divergence) is a non-symmetric measure designed to provide a number that represents the dissimilarity of two distributions (*P* and *Q*), and is commonly used/ interpreted as the distance metric between distributions. The distributions in this context are the model/simulated voxel normalized distance distribution and the distribution of the control or pre-treatment NPH patient. The equation for the KL divergence of probability distributions P and Q are shown in **equation 2:**

$$D_{KL}(P||Q) = \sum_{i} ln\left(\frac{P(i)}{Q(i)}\right)P(i) \quad [2]$$

The KL divergence is similar to a distance metric in that it always yields non-negative numbers and is only equal to zero if P and Q are identical distributions; however, because it is non-symmetric the definition of P and Q are important for the outcome. P is assigned the true distribution and in our experiment will equal the simulated dataset in which the estimated distribution represents Q and is equal to the measured data in the experiment. In these comparisons, values closer to zero have a lower variability compared with those that have greater KL divergence values.

d) Ventricle Segmentation

For the nine patients who had pre- and post- treatment scans, the total lateral and third ventricle volumes were calculated (3DSlicer, www.slicer.org). The segmentation was

performed semi-automatically following the placement of a seed point in the lateral ventricles and then edited manually by an expert.

e) Patient Outcome

Patient outcome was assessed at the time of the post-treatment scan approximately six months after surgery. The outcome was based on clinical notes at the time of the clinic visit, with an emphasis on the improvement in gait based on the suggestion by Edwards et al.[127] Although further valve adjustments were made for the majority of patients, the outcome was assessed at the time of the post-treatment scan prior to any valve adjustment.

f) Statistical Methods

All statistical analysis was performed using MATLAB 7.5 R2007b functions. For the comparison of the pre-treatment NPH and healthy control groups, the Mann Whitney Rank sum test with a significant level of 0.05 was used. When comparing paired pre- and post-treatment NPH results the Wilcoxon signed rank test was used.

C. Results

1. Segmentation

Figure 9 shows the impact of the waveform selection based on the described segmentation algorithm.

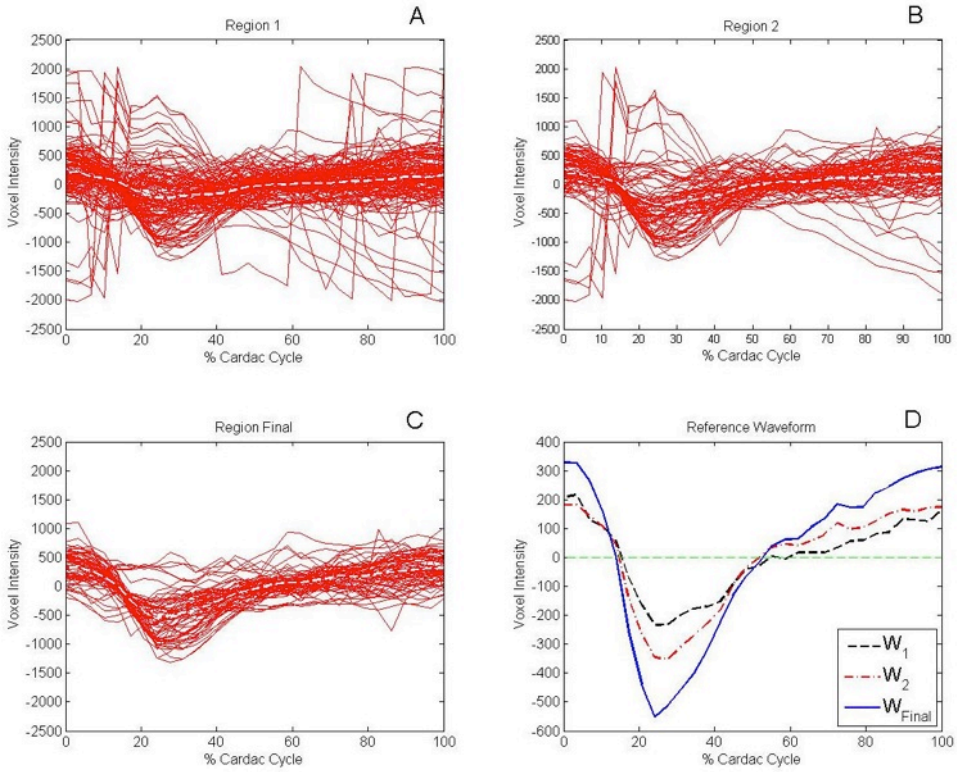

Figure 9 *Step-by-step comparison of the individual voxel waveforms for a given region (prepontine cistern of an NPH patient pre-surgery).* ***A)*** *Voxel waveform for* $Region_1$ ***B)*** $Region_2$ ***C)*** $Region_{Final}$ ***D)*** *Comparison of the reference waveforms. All results are for the complete cardiac cycle.*

Interestingly, **Figure 9B** shows an outline of the arterial blood flow in the basilar artery. This is because the basilar artery is immersed within the prepontine CSF and the initial segmentation included those voxels. **Figure 10** shows the impact of the steps of the segmentation algorithm on the ROI of the cistern.

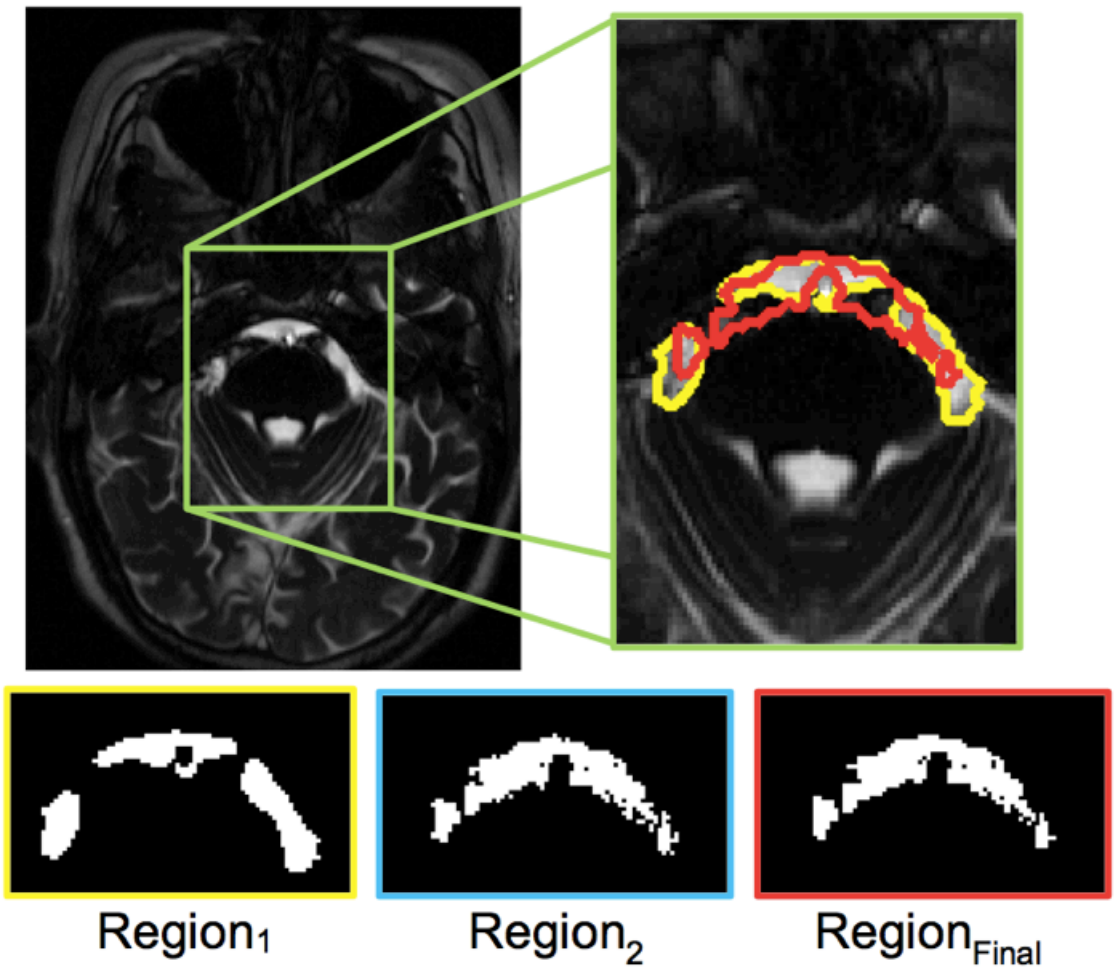

Figure 10: *Upper Left) TrueFISP image of an oblique plane of an NPH patient perpendicular to the presumed flow of CSF within the prepontine cistern. Upper Right) inset from the TrueFISP image showing the original ROI segmentation in in yellow (*$Region_1$*) and the final ROI segmentation in red (*$Region_{Final}$*). The three images on the bottom of the figure show the binary masks of the three segmentations and how they evolved.*

The V_{enc} was significantly higher in the aqueduct pre-treatment NPH group (17.8±4.5) when compared to the healthy controls (12.4 ± 4.6); however, following shunting there was no significant decrease in the V_{enc} (13.1 ± 4.9, post-treatment group). No significant differences were found between the groups in the prepontine cistern V_{enc} (9.6 ± 5.3 and 7.8 ± 2.5 for the pre-treatment NPH and controls, respectively). The threshold value used to determine the ROI did not differ significantly between groups (0.59 ± 0.07, 0.56

± 0.06, 0.57 ± 0.09 for the control, pre-, and post-treatment groups, respectively), with an overall average and standard deviation of 0.55 ± 0.08, which is near the 0.5 reported by Alperin et al.[124]

2. Velocity, Flow, and Stroke Volume

a) Hydrodynamic Results Pre-shunt NPH and Control Group

Significant differences in area, velocity, flow, and aqueductal stroke volume (ASV) metrics for the cerebral aqueduct were found between the pre-treatment NPH group and the age-matched healthy controls. Mean flow and max velocity in both the caudal and cranial direction as well as ASV and ROI area were significantly higher in the pre-treatment group. Selected metric median and interquartile ranges are shown in **Table 2**.

		Area (mm^2)	Caudal Max Velocity (cm/s)	Cranial Max Velocity (cm/s)	Caudal Mean Flow (mL/min)	Cranial Mean Flow (mL/min)	SV (µL)
Aqueduct	Pre-shunt (n = 26)	8.0 [3.1]** (5.1 – 13.7)	12.8 [7.3]* (5.3 – 21.4)	8.4 [5.6]* (4.3 – 17.0)	0.32 [0.22]** (0.12 – 0.73)	0.26 [0.18]** (0.09 – 0.57)	124.5 [90.5]** (37.1 – 275.0)
	Control (n = 10)	4.9 [1.6] (3.1 – 7.4)	7.9 [3.7] (5.3 – 15.0)	5.8 [2.0] (3.8 – 8.2)	0.12 [0.07] (0.06 – 0.19)	0.09 [0.03] (0.05 – 0.15)	49.7 [19.6] (23.1 – 90.5)
Cistern	Pre-shunt (n = 21)	58.6 [62.1] (20.1 – 255.7)			0.78 [0.30] (0.3 – 2.0)	0.43 [0.30] (0.14 – 1.47)	293.5 [135.6] (111.9–683.6)
	Control (n = 8)	69.6 [15.9] (31.1 – 92.2)			0.73 [0.33] (0.4 – 0.8)	0.41 [0.21] (0.27 – 0.63)	299.0 [144.6] (181.2 – 418.7)

Table 2: *Shows the quantitative results from the pre-shunt NPH and healthy control groups for both the aqueduct and prepontine cistern. Significant differences are denoted by *(p<0.05) and **(p<0.001). For each metric the median [iqr] is shown.*

For the prepontine cistern, no hydrodynamic metrics were found to be significantly different between the pre-treatment group and the healthy controls (**Table 2**); however, the distribution of values was wider in the NPH group. The caudal and cranial max

velocities were not reported due to the influence of noise in the cisternal measurements. Violin plots for the caudal mean flow and stroke volume for both the aqueduct and cistern are shown in **Figure 11**.

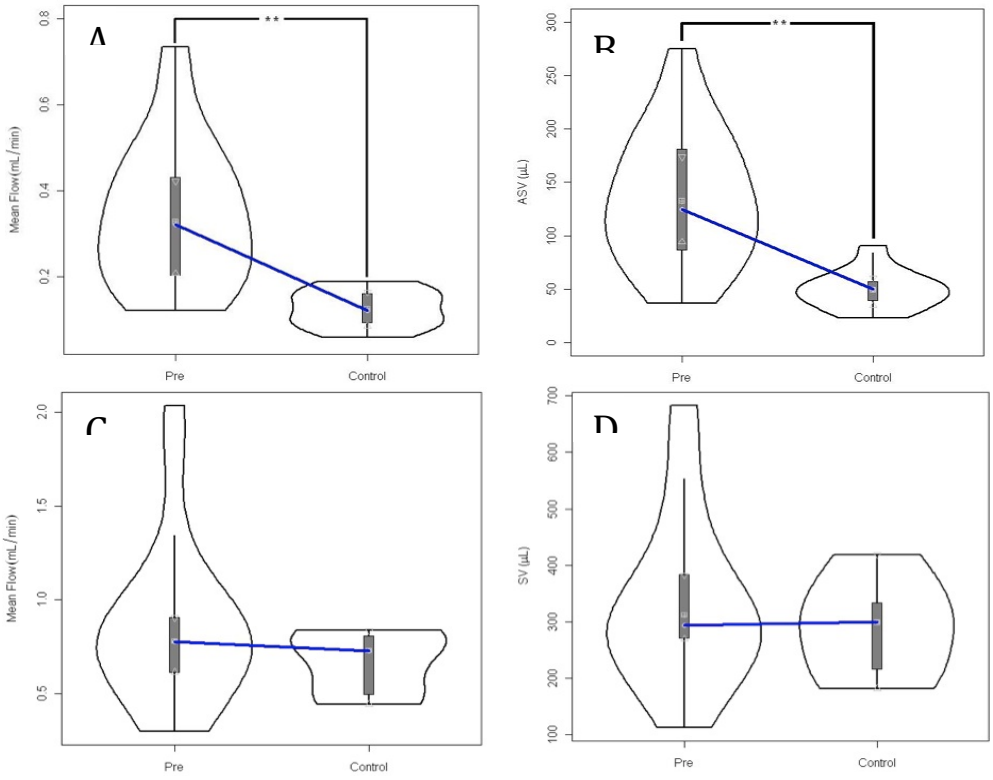

Figure 11: *Violin plots for the comparison of pre-treatment NPH group and age matched controls:* ***A)*** *Aqueductal caudal mean flow* ***B)*** *Aqueduct stroke volume* ***C)*** *Cisternal caudal mean flow* ***D)*** *Cisternal stroke volume. **signifies that p < 0.001*

b) Impact of Shunt Treatment on Hydrodynamic Metrics

Of the 12 post-treatment scans, three underwent VA shunt placement while the rest were treated with a VP shunt. In the cerebral aqueduct (nine matched pre-post pairs) ROI, caudal and cranial mean flow, and SV (**Figure 12**) were significantly reduced after shunt placement (**Table 3**). In the prepontine cistern (six matched pre-post pairs) there

was an increase in the SV (**Figure 12**) and cranial mean flow rates with caudal mean flow remaining unchanged; however, these changes failed to reach the level significance. Complete results for both the aqueduct and cistern are shown in **Table 3**.

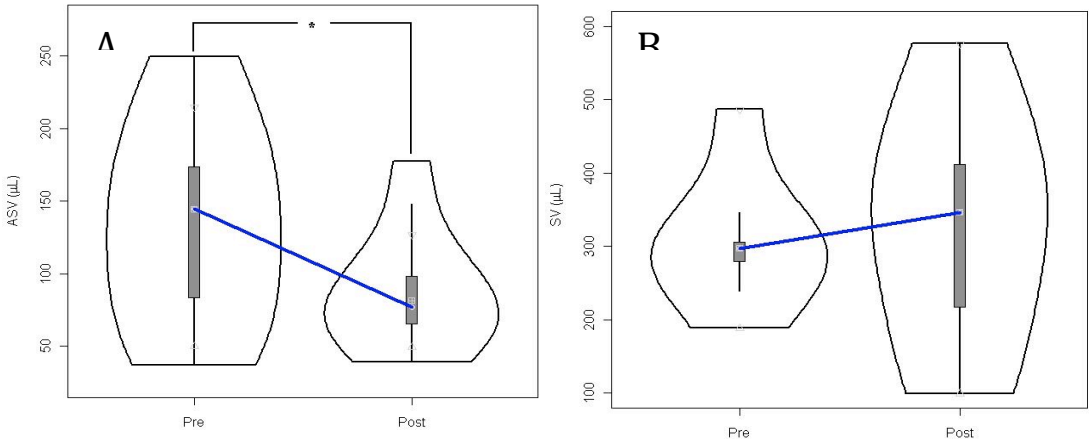

Figure 12: *Comparison of pre-treatment and post-treatment stroke volume in the aqueduct* ***A)*** *and the* ***B)*** *prepontine cistern. The decrease in aqueduct stroke volume is significant *p<0.05.*

		Area (mm^2)	Caudal Max Velocity (cm/s)	Cranial Max Velocity (cm/s)	Caudal Mean Flow (mL/min)	Cranial Mean Flow (mL/min)	SV (µL)
Aqueduct	Pre-shunt (n = 9)	8.4 [3.1]* (5.1 – 16.4)	13.4 [6.9] (6.2 – 21.4)	10.4 [4.4] (6.0-13.0)	0.47 [0.29]** (0.12-0.70)	0.32 [0.21]** (0.1-0.5)	150.2 [104.2]** (50.2 – 249.6)
	Post-shunt (n = 9)	8.0 [3.5] (3.1 - 9.0)	11.4 [4.5] (8.4 – 15.0)	6.8 [2.6] (5.4 – 11.9)	0.22 [0.16] (0.1 – 0.36)	0.15 [0.1] (0.09-0.4)	82.8 [45.5] (49.7-177.6)
Cistern	Pre-shunt (n = 6)	63.5 [78.3] (45.2-255.7)			0.91 [0.29] (0.45-1.1)	0.42 [0.31] (0.29-0.89)	301.4 [85.2] (188.3-486.5)
	Post-shunt (n = 6)	39.1 [54.9] (36.6-161.1)			0.72 [0.46] (0.2-1.1)	0.36 [0.29] (0.15-0.61)	336.9 [217.2] (99.3-430.2)

Table 3: *Shows the quantitative results from the pre- and post-shunt NPH groups for both the aqueduct and cistern. Significant differences are denoted by *(p<0.05) and **(p<0.01) from the paired Wilcoxon signed rank. For each metric the median [iqr] is shown.*

c) Stroke Volume Ratio

The stroke volume ratio is derived from the ratio of the ASV and the prepontine cistern SV for the pre-shunt, post-shunt, and control cohorts. For the pre-shunt group there were 17 patients with technically adequate aqueduct and cisternal values, resulting in a stroke volume ratio of 50.0 ± 7.3 percent mean and SEM respectively. For the post-shunt patients the stroke volume ratio was reduced ($p=0.095$) to 29.5 ± 7.2 percent ($n=7$). The control group had a stroke volume ratio that was significantly lower ($p=0.0086$) than the pre-shunt group, 17.7 ± 2.5 percent. The post-shunt and control groups did not differ significantly ($p = 0.1468$). In addition to the stroke volume ratio calculations for the entire pre- and post- shunt groups, the ratios for the six matched pre-post patients were also calculated. For the six matched patients there was a significant reduction ($p = 0.0321$) from 50.2 ± 13.3 percent to 31.5 ± 8.3 percent respectively.

3. Latency

The PFL required ECG gating of the PC-MRI data, and therefore a subset of the overall data was analyzed. For the cerebral aqueduct 16 pre-treatment NPH patients and seven control patients were analyzed. The pre-treatment group showed a slightly shorter latency of 32.7 ± 8.16 percent in the pre-treatment group compared to the control group of 34.4 ± 13.0 percent but the difference was not significant ($p = 0.66$). In the prepontine cistern there was a significantly shorter PFL ($p<0.01$) in the 15 pre-treatment patients (24.5 ± 6.3 percent) versus the five control subjects (29.6 ±13.2 percent).

Following the shunt treatment there were trends toward control values in both the cerebral aqueduct and prepontine cistern PFL, but all failed to reach the level of significance. In the cerebral aqueduct seven post treatment NPH patients had a mean ± SEM of 33.2 ±12.5 percent ($p = 0.62$ compared to the pre-treatment group). The post-treatment NPH patients had a slightly longer PFL of 27.9 ± 9.3 percent in nine patients, which again was not significantly longer than the pre-treatment group but trended toward the control group ($p = 0.06$).

4. Variability

Variability was only computed in the control and pre-treatment prepontine cistern scans. There were eight control and 28 pre-treatment NPH datasets compared using KL divergence. **Figure 13** shows the box plot for the pre- and control KL divergence measurement with the pre-treatment NPH patients having a significantly higher measure of dissimilarity ($p=0.05$) than the control patients 0.65 [0.21] and 0.53 [0.17] median and [iqr] respectively. This increased measure of dissimilarity can be interpreted as an increase variability. A KL divergence value of zero represents the situation where the compared distributions are equal and higher values representing a greater dissimilarity. Because the pre-treatment group and NPH group were compared against the ideal flow scenario, the increased dissimilarity in the NPH group can be interpreted as a greater variability or departure from normal flow.

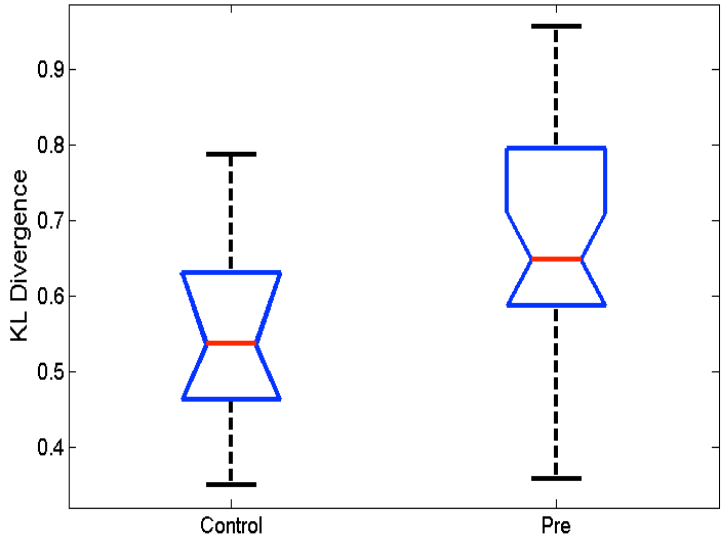

Figure 13: *Boxplot for the KL divergence measure between the control and pre-treatment NPH patients. Pre-treatment NPH patients had a significantly higher (p = 0.05) median KL divergence measurement than control patients, who had measurements of 0.65 [0.21] and 0.53 [0.17] median and [iqr] respectively.*

Figure 14, below, shows an example of the difference in flow distribution between a control patient and a pre-treatment NPH patient.

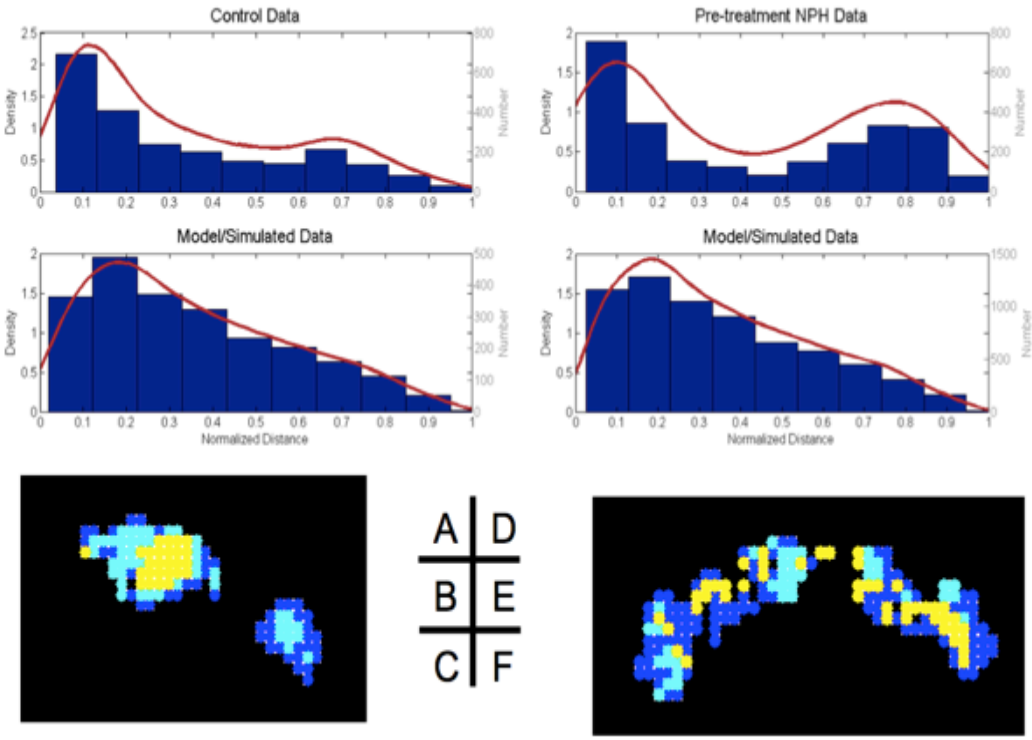

Figure 14: A) *Histogram and corresponding probability distribution for a control subject with a KL divergence value of 0.54.* ***B)*** *The model/simulated histogram and probability distribution which was compared with the control data.* ***C)*** *The corresponding cistern ROI for the control data with the three clusters of waveforms.* ***D)*** *Histogram and corresponding probability distribution for a pre-treatment patient with a KL divergence value of 0.87.* ***E)*** *The model/simulated histogram and probability distribution which was compared with the pre-treatment NPH data* ***F)*** *The corresponding cistern ROI for the pre-treatment data with the three clusters of waveforms.*

The control and pre-treatment data was compared to an idealized flow model. The results of the flow models are shown below. **Table 4** shows the results for the control and pre-treatment KL-divergence when a different ideal model is used. Note that all differences are still significant. The probability distributions from the ten idealized flow models are shown in **Figure 15**.

Model	Control		Pre-Treatment		P-Value
	Median	IQR	Median	IQR	
1	0.54	0.17	0.65	0.21	0.050
2	0.53	0.17	0.64	0.21	0.046
3	0.51	0.17	0.62	0.20	0.050
4	0.52	0.17	0.63	0.20	0.050
5	0.51	0.17	0.62	0.20	0.050
6	0.52	0.17	0.63	0.21	0.046
7	0.54	0.17	0.65	0.20	0.050
8	0.54	0.17	0.65	0.21	0.046
9	0.54	0.17	0.65	0.21	0.046
10	0.54	0.17	0.66	0.20	0.050

Table 4: *Shows the KL-divergence results for the Control and pre-treatment groups for each idealized model. The p-values generated from the Mann Whitney Rank sum test.*

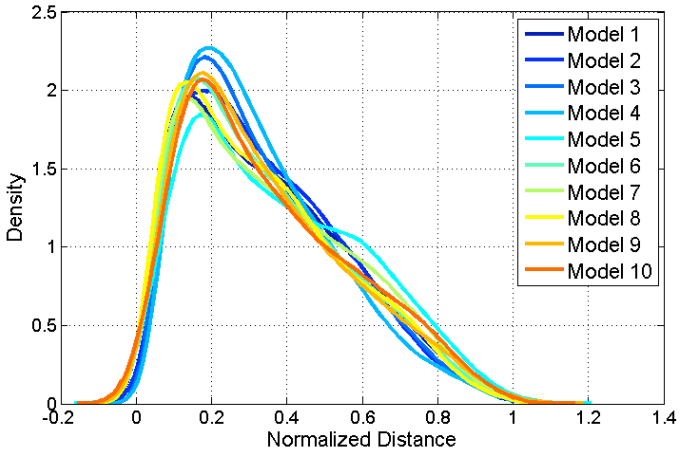

Figure 15: *Probability distributions from the ten idealized models.*

5. Ventricle Volume

The ventricle volume reported is the superposition of the lateral and third ventricles of the nine patients with pre- and post- treatment scans. The pre-shunt ventricular volumes ranged from 63.8 mL to 147.4 mL with a mean and SEM of 109.8 ± 8.2 mL. Following shunting, ventricular volumes were significantly reduced ($p<0.001$) with a mean and SEM of 91.51 ± 9.8 mL. **Figure 16** shows an example of pre- and post-treatment volume reduction from 63.8 mL to 26.2 mL respectively, a difference of 37.6 mL.

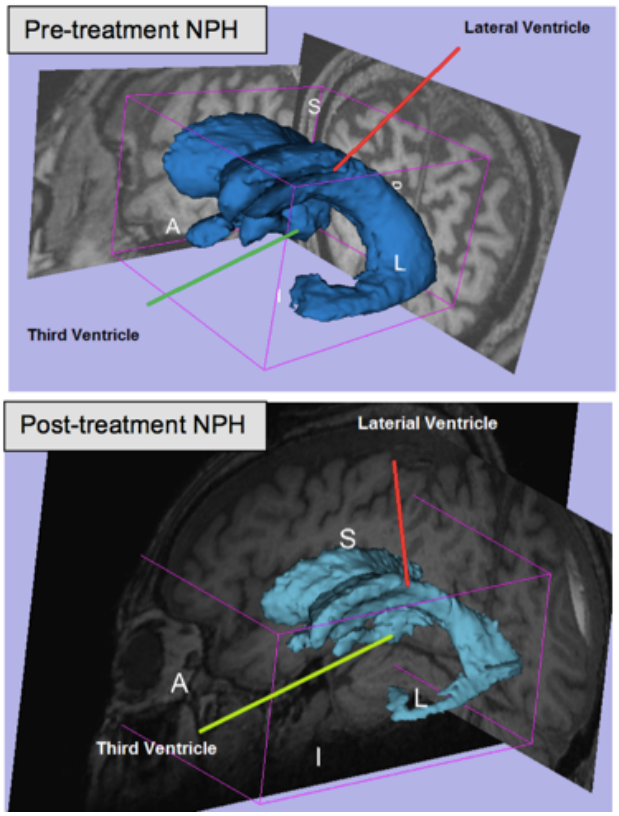

Figure 16: Top) *Pre-treatment ventricular volume of the lateral and third ventricles. The total volume of the pre-treatment scan is 63.8 mL.* ***Bottom)*** *Following CSF diversion (shunting) the volume reduced to 26.1 mL, a decrease in 37.6 mL.*

6. Patient Outcome

Of the nine patients receiving pre- and post-treatment scans, eight received a VP shunt and one received a VA shunt. Of these nine patients, only one (a VP shunt) failed to clinically improve during the six-month follow-up period.

D. Discussion

1. Segmentation

PC-MRI has been utilized throughout the body as a noninvasive method for flow quantification of blood and CSF. Specifically, within the brain, the flow of CSF within the aqueduct has been studied extensively; however, these studies have yielded little progress in the diagnosis and/or treatment of NPH. Described in this chapter is a novel

semi-automated segmentation algorithm for use in the aqueduct and prepontine cistern [128] along with three clinical studies.

The foundation of pulsatility-based segmentation lies in the definition of the reference waveform. Studies have shown the importance and influence of not only the location of the selection (within the ROI), but also the number of voxels used to calculate the reference waveform. Alperin et al. reported a maximum percentage difference of 5.4 percent with mean values within the internal carotid artery, vertebral artery, and jugular vein lumens of 3.0 percent, 3.1 percent and 3.0 percent, respectively[124] when changing the location of the seed point. The impact on the segmentation area as a function of voxels used to construct the reference waveform was also explored, showing that within the carotid artery 97 percent of the voxels were identified by only using two voxels to construct the reference waveform. Even though this may suggest that the impact of the location and number of voxels used to construct the input reference waveform is minimal; when considering the regular lumen structure of the vessels reported, the relatively high velocities compared to the prepontine cistern (3-25 and 80 cm/s respectively), and the absolute size of the regions, the influence of these factors becomes significant. We propose a method that essentially eliminates the subjectivity of reference waveform generation.[98]

a) Limitations of the segmentation

PC-MRI has many applications; however, for CSF flow quantification there are fundamental features that make accurate measurements difficult. For larger regions (usually vessels or other structures with lumens) the area is relatively large compared to

the resolution of the scan; however, when looking at the cross-sectional area of the aqueduct (1-3 mm) the impact of the partial volume effect of MRI becomes significant. Furthermore, the irregular shape, heterogenous flow patterns, and low flow velocities of the prepontine cistern also contribute to a difficult segmentation environment.

b) Threshold Value

As mentioned previously, the segmentation algorithm is a function of the reference waveform, which in turn is intimately connected to the definition of the threshold value. The threshold value varies drastically between studies; Alperin et al. reported threshold values of 0.5 and 0.75 depending on the details of the study[124]. Furthermore, Yoshida et al. used a similar correlation-based approach with minimal threshold values ranging from 0.3 to 0.45.[129] Based on the drastic difference in reported methods, the use of a static threshold is not ideal for optimal segmentation. Automatically identifying the optimal threshold value on a case-by-case basis is essential for accurate, reproducible results. However, this means that a certain level of subjectivity remains in the determination of the threshold value, which thus does not scale well.

Currently, the threshold value is determined based on the “plateau region” variants from patient to patient that can be seen in **Figure 6**. In the example presented in **Figure 6**, a decrease in the threshold value increases the number of voxels included in the ROI, thereby having a large impact on a subset of the hydrodynamic metrics.

No flow phantom experiments were performed to determine the accuracy of this algorithm. This decision was made based on the requirements for a flow phantom

experiment. This would include the ability to operate the MRI after hours along with a flow phantom unit. I do not believe that in this well-developed field the cost of training and scan time are worth the investment.

2. Cerebral Dynamics

a) Study 1

In Study 1, no significant differences were found in the mean CSF volumetric results of the prepontine cistern between the pre-treatment NPH group and the control group (**Table 2** and **Figure 11**), although the range of values was higher in the pre-shunt NPH group. We documented prepontine SV values in NPH patients that were nearly two times lower than the smallest value obtained in the control group. Balédent et al. reported that the prepontine cisternal CSF flow in patients with CH was smaller than in healthy controls, but no quantities were given.[106] Greitz, SVs for the prepontine cistern in two healthy controls (SV = 0.33 ± 0.08 mL) and one CH patient (SV = 0.14 mL).[120] It is difficult to compare our study with these studies due to differences in ROI segmentation and imaging metrics.

Study 1, like several others, demonstrated a significant difference in ASV and other hydrodynamic metrics between hydrocephalic patients and healthy controls.[106,123,130] Balédent et al. implemented an automated method for segmentation of CSF and blood flow and found significant differences between area and SV within the aqueduct between healthy controls and patients with CH. Their results, based on 16 phase segments, showed an increased area (17.0 mm^2 vs. 8.0 mm^2) and increased ASV (196.0 µL/mL vs. 51.0 µL/mL) for hydrocephalic patients versus healthy controls,

respectively.[106] Furthermore, significant differences between CH (various etiologies) and healthy controls were also found by Abbey et al. within the aqueduct for area (10.0 ± 8.9 mm^2, 2.0 – 27.0 mm^2 and 2.0 ± 1.0 mm^2, 1.0 – 4.0 mm^2) and ASV (5.6 - 256.4 µL, 87.20 ± 79.04 µL and 1.9 - 33.2 µL, 17.4 ± 10.1 µL); however, differences in peak systolic and diastolic velocities were not found to be significant between the two groups,[123] in contrast to the differences found in our study.

Not unexpectedly, an increase in the mean ASV combined with no difference in the prepontine SV value resulted in an increase in the stroke volume ratio. Wagshul et al. investigated the CSF stroke volume ratio between the aqueduct and foramen of magnum in 15 healthy adults;[121] although the study did not include CH patients, they were able to define values for the stroke volume ratio in controls. In a related study by Balédent et al., the CH patients showed a significantly higher stroke volume ratio than healthy controls did, with ratios of 42 percent and 11 percent respectively.[106]

(1) Impact of shunting

Shunting remains the primary treatment for NPH. Following the shunting procedure, 12 NPH patients (nine matched aqueduct studies and six matched cistern studies) received identical imaging protocols with a mean follow-up time of six months. Following shunt surgery, cisternal CSF metrics were slightly increased in the SV and cranial mean flow, but did not reach the level of significance.

The diversion of CSF resulted in a significant decrease in both the caudal and cranial mean flow ($p < 0.05$) and ASV ($p < 0.05$) in the aqueduct, which is consistent with

Abbey et al.;[123] however, in contrast to their study, peak velocities (caudal and cranial) and area were not found to be significantly reduced[123] (**Table 3** and **Figure 12**). Again, there have been several studies that show a decrease in the ASV, flow, and velocity following a shunt procedure;[101,125] however, the mechanisms underlying this decrease in hydrodynamics have been relatively unexplored.

The CSF shunts used in our study include a valve mechanism that is a one-way check valve with a certain opening pressure value. For the post-shunt studies, we assume that the system is in steady-state, and therefore CSF flow down the shunt occurs when the peak CSF pulsatile pressure exceeds the threshold value, resulting in microbolus flow. In a study by Miyaje et al., the CSF flow through the shunt was measured using a microflowmeter in seven NPH patients; which included changes in valve opening pressure and changes in position (sitting and standing).[131] For patients in the recumbent position (the same as in the MRI), the study reported that at low valve opening pressures, flow within the shunt varied between 100 and 200 μL/min. When investigating the significant reduction in mean aqueductal flow in our study between the nine pre- and post- surgical patients, there is an average decrease in the caudal and cranial mean flow of 147.1 ± 160.2 and 92.4 ± 97.5 μL/min, respectively. In other words, the magnitude of the decrease in mean flow through the aqueduct is approximately equal to the data reported by Miyaje et al. for the flow through a shunt while in the supine position.

The stroke volume ratio following shunt surgery showed a decrease in the larger (unmatched) cohort but was not significant ($p = 0.095$); however, in the six matched patients with pre- and post- scans there was a significant reduction in stroke volume ratio following the surgery ($p = 0.03$). Furthermore, the pre-shunt group had a significantly higher stroke volume ratio than the control group ($p = 0.0086$), which correlated well with Balédent's work described above. The absolute value of the ratios cannot be directly compared to work by Balédent et al. or Wagshul et al. because of the difference in location for the SAS stroke volume measurement. When investigating the contributions of the aqueduct and the cistern, the significant differences shown should be expected. Although the significant decrease in stroke volume ratio seems to be driven by the significant decrease in ASV shown in **Table 2** and **Table 3**, the upward trend of cisternal SV following surgery supports the hypothesis of redistribution of intracranial CSF pulsations.

b) Study 2

To supplement the volumetric analysis in Study 1, latency metrics were also investigated. Unlike the volumetric results, the aqueduct showed no significant differences in PFL between the groups; however, there was a trend showing a shortened latency in the pre-treatment group compared with the healthy controls, which corresponded well with our hypothesis. In the prepontine cistern the pre-treatment group showed a significantly shorter PFL compared with the healthy controls (**Figure 18**).

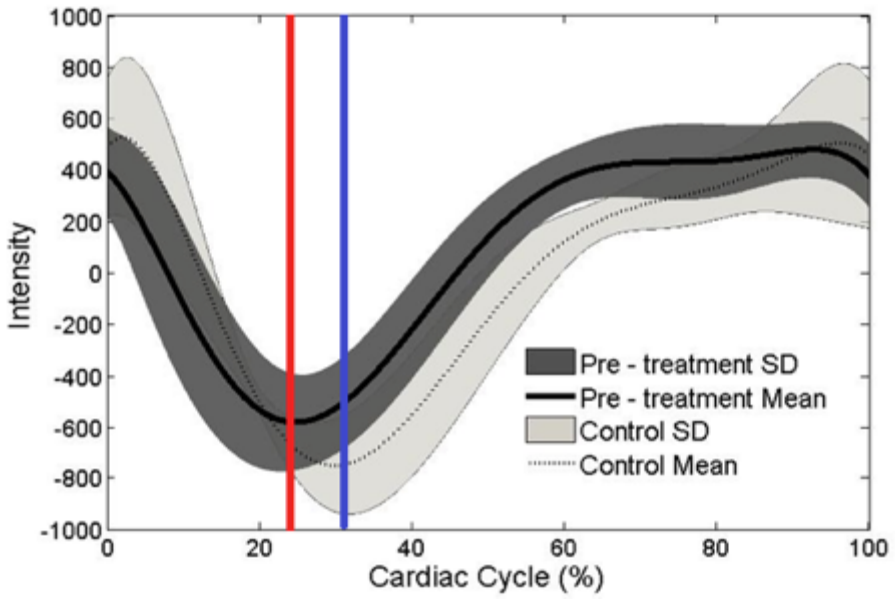

Figure 18: *Mean flow curves in the prepontine cistern for the pre-treatment and control groups. The curves are the average of the polynomial fit (6th degree) of the entire group (SD is also shown as a shaded region). The difference seen between the peak latency (defined as the minimum point of the curve) is significantly shorter ($p < 0.01$) in the pre-treatment group than in the control group. Voxel intensity, not velocity (cm/s) is given on the y axis. Red and blue lines represents the pre-treatment and control PFL respectively.*

The PFL calculations are dependent on two variables: the degree of the polynomial used to increase the temporal resolution and the percentage of voxels removed from the original ROI. **Table 4** shows the corresponding p-values for the prepontine cistern for a number of different combinations of the degree of polynomial (4-10) and percentage of voxels removed. The analysis reported is for a six-degree polynomial and 75 percent voxel removal (marked with an asterisk in **Table 4**). There is minimal impact on the overall significance of the PFL by altering these two variables between the pre-treatment NPH group and healthy controls. However, when 95 percent of the data is removed (thus a majority of the voxels) and the degree of the polynomial fit is relatively high (8-10) the results are no longer significant. This trend is expected; as voxels are

removed there is more influence from individual voxels, increasing the noise in the results along with "over-fitting" from the high degree polynomial fit. Taken at both extremes, a poor fitting or over-fitting polynomial will confound the final results. Finally, when no polynomial fit is performed, the results become very irregular and the level of significance is rarely reached (**Table 5**).

	Percentage of low-correlated voxels removed from the ROI						
Degree of Fit	**1%**	**10%**	**25%**	**50%**	**75%**	**90%**	**95%**
No Poly Fit	0.076	0.076	0.061	0.107	0.040	0.094	0.061
4	0.007	0.009	0.009	0.009	0.009	0.007	0.004
5	0.009	0.009	0.011	0.009	0.011	0.007	0.015
6	0.009	0.007	0.009	0.009	**0.009***	0.007	0.015
7	0.023	0.014	0.014	0.025	0.023	0.009	0.036
8	0.044	0.036	0.044	0.044	0.029	0.009	0.067
9	0.036	0.036	0.044	0.040	0.029	0.011	0.067
10	0.066	0.055	0.036	0.044	0.036	0.011	0.116

***Table 5**: P-value from the Mann Whitney Rank sum comparing pre-treatment NPH and control patients for prepontine cistern PFL. For this analysis a six degree polynomial was used to fit the flow data and the top 25 percent of the voxels were used in the calculation (represents 75 percent of the low-correlated voxels were removed), and p value is shown with an *. The "No Poly Fit" row contains the results excluding any polynomial fitting.*

As established earlier, the pathoetiology of NPH has been discussed to a great extent in the literature, which offers a wide variety of possible root causes. One topic that remains relatively unexplored is the relationship of parenchymal changes to pathogenesis and symptoms in NPH. A new technology known as magnetic resonance elastography (MRE)[132] has the ability to quantify the mechanical properties of the microstructure of the parenchyma. Using this technology, a recent study by Freimann et al. investigated the changes in mechanical properties of the pre- and post- shunt brain of NPH patients and compared those changes to healthy controls[133]. Two significant findings were

reported: first, there was a significant difference between shear elasticity (μ) between the control group and the pre-shunt NPH group that did not correct following shunting. Shear elasticity is a measure of global brain stiffness; therefore, the significant decrease in μ represents a decrease in brain stiffness of the NPH patients. The other finding showed a significant decrease in a parameter known as the connectivity parameter (α) between the healthy control group and the pre-treatment NPH group. Following surgery the connectivity parameter returned to normal ranges. Unlike brain stiffness, the connectivity parameters are slightly more abstract, being described by the authors as being "sensitive to the geometry of the mechanical network."[133] In other words, there is a reorganization of the parenchymal microstructure toward healthy values (which are more organized) (**Figure 19**). We hypothesize that this reorganization following shunting could contribute to the reversal in both the volumetric and latency trends in the prepontine cistern. As we discussed earlier, the aqueductal change is also influenced by the removal of the CSF via shunting.

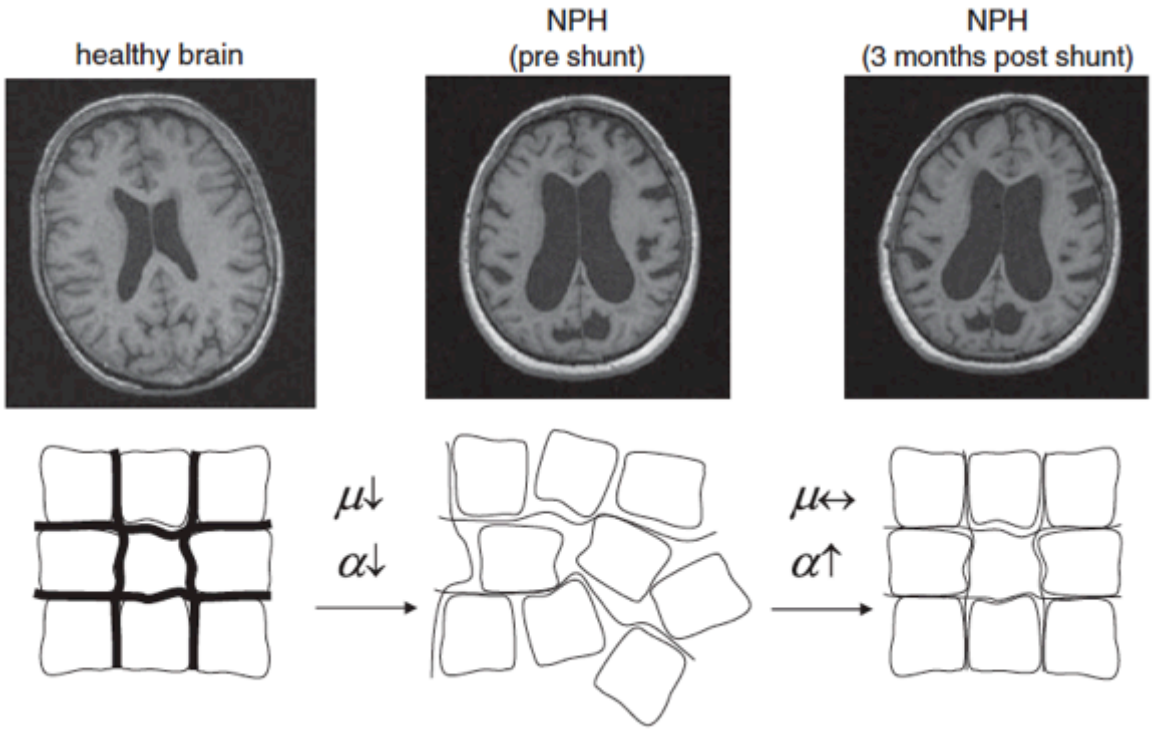

Figure 19: *NPH is associated with ventriculomegaly, which is not necessarily recovered after shunting. Cerebral MRE reveals a disease-related decrease in global brain stiffness indicated by μ, which is not improved by shunt treatment. In contrast, α increases three months after shunt implantation to almost unsymptomatic values, which suggests that the topology of the mechanical tissue matrix is reorganized while its inherent strength remains degraded. Reproduced with permission Freimann et al.*[133]

Our study was limited by the limited number of subjects, particularly patients who were studied both pre- and post-shunt. There were also significant technical challenges. The prepontine cistern is a complex anatomical structure that includes the basilar artery as well as small veins. Arachnoidal septations within the cistern, if present, could possibly direct pulsatile CSF in directions not aligned with the axis of the brainstem. Each or both of these could have contributed to errors in the automated segmentation algorithm, resulting in both inaccurate ROI areas and flow values. Ultrahigh resolution imaging with stronger Tesla MRIs and multiplane imaging could perhaps address these challenges, but were not possible here.

c) Study 3

In addition to the significant decreases in ASV and upward trending of cisternal CSF flow, we also observed an increased variation in SV magnitudes over the pre-treatment NPH group compared with the control subjects (**Table 2**). Based on the observation of cisternal scaring by several neurosurgeons, we hypothesized that NPH patients should have increased variability compared to control subjects, which we were able to show (**Figure 13 and 14**). Using KL divergence, which is an alteration of the general form of entropy, we were able to show a significantly increased variation in flow in the pre-treatment NPH patients compared with the controls. KL divergence has been described as a pseudo-distance metric for probability distributions because of its non-symmetrical properties, but was uniquely suitable for this comparison. KL divergence has been used in a wide variety of fields including mutual information determination and neural coding.[134] Clinically, the results support our hypothesis that NPH patient's altered CSF dynamics extend past the ventricular system into the subarachnoid space.

E. Conclusion

This chapter is multifaceted, both clinically and technically. Technically, as MRI hardware and software continue to develop, similar advancements will need to be made in image processing techniques in order to continually provide valuable information to clinicians. The pulsatility-based algorithm presented here is a combination of anatomical and pulsatility-based information, which provides superior results compared with individual manual segmentation. Clinically, the contributions of this work expand greatly on decades old research in the area of CSF dynamics and NPH. Utilizing stroke volume, latency, and variability measurements in the cerebral aqueduct and prepontine

cistern we would able to show that changes in the cisternal latency and variability were associated with the altered CSF dynamics of NPH. These finding not only provide valuable information about the pathoetiology of the NPH but also may provide a noninvasive prognostic tool for clinicians to use in the future when trying to determine which patients may benefit most from CSF diversion shunting.

VI. Chapter 3

A. Introduction

Normal pressure hydrocephalus (NPH) is a particular form of communicating hydrocephalus (CH) initially described by Hakin and Adams over 50 years ago.[57] The traditional clinical triad of dementia, gait disturbance, and urinary incontinence was described in detail in Chapter 1. The diversion of cerebrospinal fluid (CSF) via ventricular shunt remains the principal treatment option; however, differentiating patients who benefit from this procedure remains widely debated. Determining the prognosis of patients with NPH is significant due to the complication and malfunction associated with the existing shunt technologies.

The last several decades have introduced a variety of methods for identifying shunt responders from those with less favorable responses. Recent guidelines on supplementary prognostic tests for NPH allowed a broad spectrum review of these tests, including radionuclide cisternography, CSF tap test, intracranial pressure (ICP) monitoring, CSF outflow resistance (R_o), aqueductal CSF hydrodynamics, and external lumbar drain (ELD) to make recommendations for future use. Based on the review, the panel recommended the use of ELD (500 ml/3day) for differentiating patients most likely to respond to shunt, but mention additional tests may be implemented to increase accuracy.[102] A later study on 151 NPH patients by Marmarou et al. supported this recommendation, by reporting 92% sensitivity in differentiating shunt responders and non-responders, and remains one of the most important recent papers on prognostic testing for NPH patients.[68] Despite the evidence for ELD, high economic cost (extended

hospital stay) and increased risk to the patient (infection) caused several institutions to implement additional prognostic procedures to help identify shunt responders.

Overnight ICP monitoring is one example of a possible alternative/supplement to ELD. A majority of the prognostic literature for overnight ICP monitoring has focused on slow wave activity characterized by Lundberg in the 1960s.[11] Despites some early positive results that linked increased slow wave activity to positive shunt response,[16,43] others have shown no correlation.[17,18] In addition to investigations of slow wave activity, there have been recent studies of the cardiac induced ICP pulse pressure waveform (**Figure 1**), which have shown promising results. Eide et al. compared mean ICP, ICP pulse amplitude (waveAmp), and other ICP metrics from overnight ICP recordings as possible prognostic features for NPH shunt outcome. Their study reported 98% sensitivity and 70% specificity, based off average and percent time values for ICP pulse amplitude (waveAmp), where mean ICP reported much lower values of sensitivity and specificity.[43] The findings were made possible by their in-house analysis algorithm, which extracted additional features from the ICP pulse pressure waveform.[37]

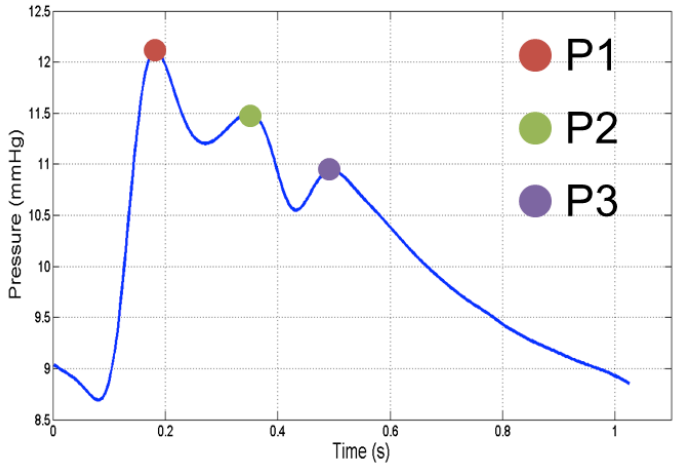

Figure 1: *Pulse pressure ICP waveform with characteristic peaks identified (P1, P2, P3). The pulse pressure waveform is created by the influx of arterial blood entering the cranial vault during each cardiac cycle.*

Another example of advanced ICP waveform analysis is the Morphological Clustering and Analysis of Intracranial Pulse (MOCAIP) algorithm developed by our group.[38] MOCAIP allows for the quantification of several ICP morphological features and has been shown to be advantageous over traditional monitoring/diagnostic techniques in several clinical studies.[22,45,47,48,135-137] This chapter will focus on the applications of MOCAIP on the ICP pulse pressure waveform of overnight ICP monitoring for the prediction of ELD outcome. The work is divided into the two studies described below.

1. Study 1

Given the success of Eide et al. in their study of advanced morphological metrics and the prediction of ELD outcome, the first study aims to develop an automated method of feature extraction and decision rule construction from overnight ICP recording.

Specifically, we used the MOCAIP algorithm to analyze the overnight ICP recordings. MOCAIP was applied to consecutive short segments of an ICP recording resulting in

128 metrics per segment. Then various feature functions were designed to summarize the distribution of the 128 metrics from all the segments per each ICP recording. The predictive value of each feature-metric pair was then assessed using the area under curve (AUC) of the receiver operator characteristic (ROC) curve. Based on the ROC curve, a simple decision rule involving one metric can be derived for predicting LD outcome. To further improve the performance, we proposed an automated way to combine two such simple rules, in either an “AND” or an “OR” manner, to achieve better performance.

2. Study 2

The second study investigated a novel MOCAIP metric related to the third characteristic peak of the ICP waveform (see P3 in **Figure 1**). We hypothesize that the relative elevation of the third peak can be used as a prognostic metric for ELD outcome in NPH patients. This hypothesis is rooted in work performed by Hu et al. that showed a correlation between the third peak of the ICP pulse pressure waveform and changes in cerebral blood flow (CBF) measured by ^{133}Xe.[47] Based on the Hu et al. findings, our study investigates the ability of a novel ICP metric, the ratio of dP3 and waveAmp (P3ratio) from overnight ICP monitoring, to predict ELD outcome.

B. Methods

The foundation of this chapter is centered on advanced morphologic analysis of the ICP waveform and our lab’s hallmark analysis tool MOCAIP.

1. MOCAIP

Morphological Clustering and Analysis of Continuous Intracranial Pulse (MOCAIP) is an analysis toolbox devoted to real time time-domain analysis of intracranial waveform

morphology. Originally developed for analysis of the ICP waveform,[38] this modular framework (**Figure 2**) has recently been extended to cerebral blood flow velocity (CBFV) waveform morphology.[138] ICP and CBFV morphological metrics have been shown to be advantageous over traditional individual metrics (mean ICP and mean CBFV respectively) in several investigations including: prediction of ICP hypertension,[136] detection of cerebral hypoperfusion,[47] assessment of noninvasive ICP,[139] segmentation of ICP slow waves,[22] changes in vasoreactivity (vasodilatation),[135] with a variety of additional projects currently underway. Although there are several publications on specific aspects of this algorithm (characteristic peak determination[140,141] for example), a general overview is provided below.[38]

The MOCAIP algorithm is modular (**Figure 2**), utilizing five individual steps and a reference library to analyze raw time-series data. First, MOCAIP segments the raw data into individual ICP pulses; this process can either use ECG as an additional input to aid in segmentation[142] (ECG QRS detection[143]), or if ECG is not available, use a pulse detection technique. Following the pulse segmentation, a segment of pulses (times of the segments are dependent on the project; however they range from pulse-by-pulse to one minute clusters) is clustered using a hierarchical clustering method. From the largest cluster, a representative pulse or “dominant pulse” is defined for each segment by the mean of the cluster. The dominant pulse is checked against a library of legitimate ICP pulses to avoid selection of a segment that is either entirely noise (the clustering algorithm will cluster its input regardless of quality), or heavily contaminated with noise. Once the dominant pulse has been verified, six landmarks are determined, the three

characteristic peaks[35] and their corresponding valleys. The automated process for identifying these peaks has evolved over time and details can be found in previous publications.[140,141] Finally, the algorithm extracts 128 MOCAIP metrics based on the six landmarks for each dominant pulse, an example of the MOCAIP metrics are shown in **Figures 3**.

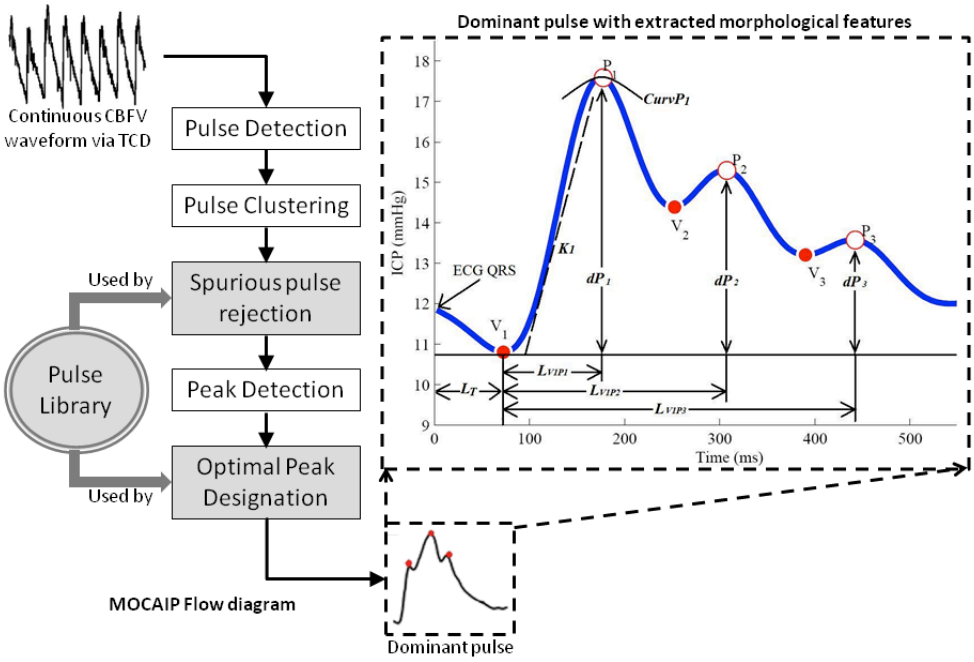

Figure 2: *Block diagram of the MOCAIP process showing a continuous CBFV input waveform that is transformed into one dominant (representative) output CBFV pulse with three sub-peaks. Inset shows a schematic dominant pulse from a CBFV waveform with the six landmarks (three peaks and three valley points).*

28 Basic metrics extracted from individual landmarks or over all characteristics	
dV1, dV2, dV3, dP1, dP2, dP3	Amplitude of landmark relative to the minimum point prior to initial rise
L_{V1P1}, L_{V1P2}, L_{V1P3}, L_{V2P2}, L_{V3P3}	Time delay among landmarks
$Curv_{v1}$, $Curv_{v2}$, $Curv_{v3}$, $Curv_{p1}$, $Curv_{p2}$, $Curv_{p3}$	Absolute curvature of each landmark
K1, K2, K3, RC1, RC2, RC3	K1, K2, K3 are slope of each rising edge and RC1, RC2, RC3 are time-constants of each descending edge
mICP, diasICP	Mean ICP and diastolic ICP
L_T	Time delay of V_1 to ECG QRS peak
mCurv	Mean absolute curvature of the pulse
WaveAmp	Maximum among dP1–dP3
100 extended metrics calculated as ratios among metrics within each group	
$dP_{p1p2,...}$	Ratio among landmark amplitudes
$L_{V1P1}/L_{T,...}$	Ratio among time delays
$Curv_{v1}/Curv_{v2,...}$	Ratio among curvatures
$K_1/RC_{1,...}$	Ratio among slopes/RCs

Figure 3: *A complete list of the 128 MOCAIP metrics Table courtesy of Asgari et al.*[135] *The 100 additional metrics are in the form of ratios of the basic 28 metrics. The ratios are represented as follows: RLv2p2Lp1p2 represents the ratio (R) of the latency between the second valley and the second peak (Lv2p2) and the latency between the first peak and second peak (Lp1p2).*

The following work expands on the benefits of the morphological features of ICP in two specific studies.

2. ICP Morphological Tests

a) Individual MOCAIP Feature Functions

The first study reported in this chapter involved 54 patients undergoing pre-shunt workup that included overnight ICP monitoring and ELD trial while hospitalized at the UCLA Adult Hydrocephalus Center; all procedures and data collection were approved by the local IRB committee with written patient consent. An intraparenchymal ICP microsensor (Codman and Schurtleff, Raynaud, MA) was inserted in the right frontal lobe and monitoring started at least one night before the placement of the LD. Continuous waveform data including ECG and ICP was captured using the BedMaster system with a sampling rate of 240 Hz. Patients were assessed both pre-LD and post-LD before discharge from the hospital by 10m-walking exam, and an NPH routine

assessment which includes the Mini-mental state examination (MMSE). The LD outcome used in the present work was retrospectively collected as indicated from the clinical report of the follow-up visit after the LD procedure and predominantly focused on the improvement in gait.[127] The average age and standard deviation of the 54 patients is 72.05 ± 9.63 years respectively, with a gender distribution of 35 males and 19 females.

(1) Feature Functions

The ICP data was analyzed using the MOCAIP algorithm described section **II.A** above, with a dominate pulse length of 30 seconds. Once the metrics for each dominant pulse have been computed an additional processing step was used to summarize each of the 128 MOCAIP metrics for one overnight ICP recording via five feature functions. For example, if a patient has 10 hours of continuous ICP data there will be approximately 1200 dominant pulses, for each dominant pulse there is 128 MOCAIP metrics, each of the MOCAIP metrics can be summarized with the five feature functions (below). There is no prior knowledge with regard to the best way of summarizing an overnight ICP recording. Therefore, it is necessary to allow for an automated process to identify the best candidates. We have evaluated the following feature functions:

(1) **Average feature:** This feature function simply calculates the average of each individual metric across one overnight ICP recording.

(2) **Standard deviation feature:** This function calculates the standard deviation of each individual metric across one overnight ICP recording.

(3) **Percentage feature:** This function calculates the percentage of time when a metric is greater than a threshold. This threshold is determined by pooling data from all patients and then determined as the average of the corresponding MOCAIP metric.

(4) **Percentage of standard deviation feature:** This function calculates the percentage of time of the standard deviation of MOCAIP metrics greater than a threshold calculated from a 5-minute ICP. The threshold was determined as the standard deviation of pooled MOCAIP metrics from all patients.

(5) **Range feature:** This function calculates the difference between the 95 percentile and the 5 percentile of each individual metric of an overnight ICP recording.

(2) Optimal Single-Metric Rule

After applying a feature function, an overnight ICP recording is reduced to a vector of 128 metric-feature pairs. We next seek for a single-metric rule to predict LD outcome in the following form: “if a metric-feature of an overnight recording is greater (or smaller) than a threshold, then LD outcome will be positive.” Note, rules published in several existing studies[43,86] can be considered as specific instances of the above form. For each metric-feature, we generate a sequence of threshold values by pooling all the data. This

sequence of threshold values can be used to generate two ROC curves for each metric-feature, one of which corresponds to the “greater than” situation and another of which corresponds to the “less than” situation. Then we retain the ROC that has an AUC greater than 0.5 and discard the other one for each metric. Next, for each feature the optimal metric is defined as the one with the greatest AUC. The impact of the optimal metric selection (as a function of AUC) is explained in the results section.

(3) Automated Combination of Two Rules

After finding the optimal metric-feature for each feature function, one natural step further is to determine if one can combine two such rules to obtain a better performance (a combination of two of the five features described above). Considering the combination of two features (A and B) with the corresponding set of false positive (FP), true positive (TP), false negative (FN), and true negative (TN) cases represented (from rule A) as FP_A, TP_A, FN_A, TN_A, respectively, the notation is analogous for rule B. Furthermore, we shall consider two possible combination operations: “AND” and “OR”. If the “OR” operator is used for combination, then the resultant sets of false positive, true positive, false negative, and true negative are shown in **Equation 1**. Conversely, if the “AND” operator is used for combination, then the corresponding sets are shown in **Equation 2**.

$$FP_A \cup FP_B \quad TP_A \cup TP_B \quad FN_A \cap FN_B \quad TN_A \cap TN_B \quad [1]$$

$$FP_A \cap FP_B \quad TP_A \cap TP_B \quad FN_A \cup FN_B \quad TN_A \cup TN_B \quad [2]$$

Based on this analysis, the accuracy of the combined predictive rules can be calculated for the “OR” operator in **Equation 3** where N represents the total number of patients. Similarly, the accuracy of the “AND” operator can be calculated using **Equation 4**.

Following the calculation of both accuracy parameters one can choose which maximizes the results.

$$Accuracy_1 = \frac{1}{N}(|TP_A \cup TP_B| + |TN_A \cap TN_B|) \quad [3]$$

$$Accuracy_2 = \frac{1}{N}(|TP_A \cap TP_B| + |TN_A \cup TN_B|) \quad [4]$$

(4) Data Analysis Protocol

In this section, we summarize the data analysis protocol used in the present work to determine the best rule combination and its accuracy. The following steps were taken to analyze the 54 overnight ICP recordings:

1) Each recording is analyzed using the MOCAIP algorithm on consecutive 30-second segments.

2) Resultant MOCAIP results are then manually checked for any errors in recognizing legitimate dominant pulse and placement of the landmarks. This step is facilitated by using software developed in house MATLAB 7.5 R2007b (The MathWorks, Inc., Natick, MA, USA).

3) Generate the threshold sequence for each metric that will be used to generate ROC curve. The i-th value of the sequence of thresholds is calculated for each metric-feature by the following equations: (i-1)×L where L is the mean plus the 10 standard deviation of the metric-feature divided by the number of steps, which is 100 in the present work.

4) Each value of the threshold sequence is used to form two simple rules (“greater than” and “less than”), which are then used to assess the 54 cases. The corresponding false positive rate (FPR) and true positive rate (TPR) are obtained. After sweeping through the sequence, two ROC curves are obtained but only the one with AUC greater 0.5 is retained.

5) Determine the optimal metric-feature. This is achieved by selecting one metric-feature that has the largest AUC per each feature function evaluated. In other words, for each feature defined above, the metric (out of the 128 calculated by MOCAIP) with the greatest AUC is defined as the optimal metric-feature (five total, one for each feature).

6) Determine the rule. For the optimal metric-feature, the “optimal” point on the ROC curve is selected as the operating point, which gives a false positive rate less than 0.35.

7) Then the accuracy of 10 (combining two features with a total of five features 2*5 = 10) pairs of AND-combination of the five optimal metric-feature rules and those of the OR-combination are calculated.

8) The best rule combination is then determined as the one with the greatest accuracy.

b) P3 Elevation

From July 2007 to November 2011 (this study window was open longer than the previous study), 167 probable NPH patients were admitted to the UCLA Adult Hydrocephalus Clinic for three day ELD trial Of the 167 patients, 66 (40%) received overnight ICP monitoring before the placement of the LD. The decision for ICP monitoring was made by the attending physician based on history and symptoms. This patient cohort consisted of 45 males and 21 females with an average age of 72.2 ± 9.8 years ranging from 45 to 91 years. All data collection and diagnostic procedures were approved by the local IRB committee and written consent was obtained from the patient or medical proxy prior to all procedures. For the ICP monitoring an intraparenchymal ICP microsensor (Codman and Schurtleff, Raynaud, MA) was placed in the right frontal lobe and monitoring started one night before the placement of the LD. Both ECG and ICP were collected continuously with a sampling rate of 240 Hz using the BedMaster system (Excel Medical Electronics, Inc. Jupiter, FL).

(1) ICP Analysis

Following data collection the ICP waveform was analyzed using the MOCAIP algorithm which was described above. In addition to the MOCAIP metrics an additional feature was extracted to investigate specific changes in the ratio of the third peak (P3ratio), which is not represented in the original MOCAIP metrics. The P3ratio was defined as the amplitude of the third peak divided by the wave amplitude of the ICP pulse pressure (waveAmp) shown in **Figure 4**. To specifically address our hypothesis that relative elevations in the P3ratio may be a prognostic indicator of ELD outcome, P3ratio was compared to traditional measurements of ICP pulse pressure features, mean ICP and waveAmp. For the statistical comparison the median value from the overnight monitoring was extracted for each of the ICP morphological metrics.

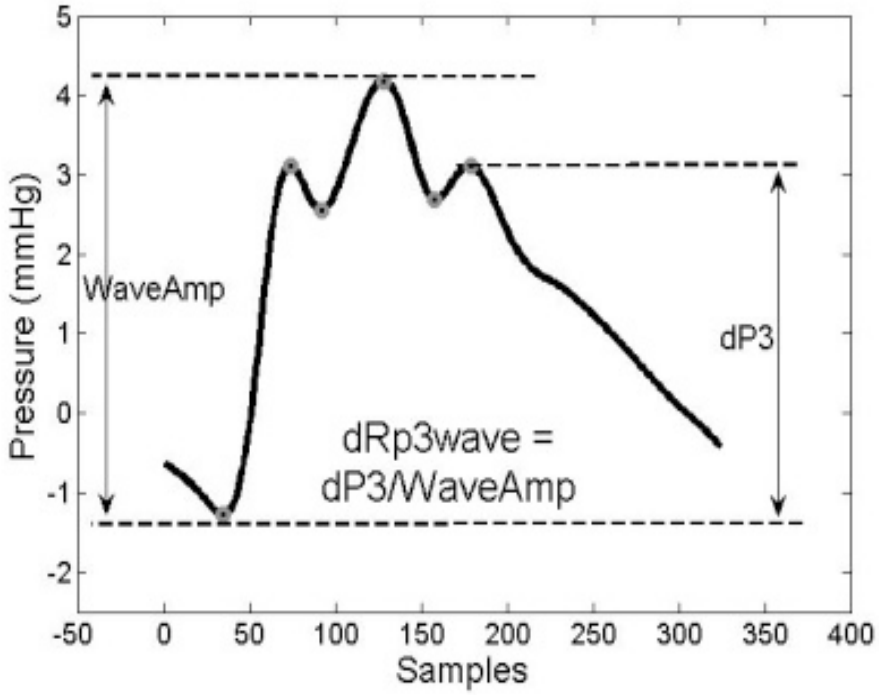

Figure 4: *Illustration of the P3Ratio feature on an ICP pulse pressure waveform.*

(2) Patient Outcome

The patient's response to the ELD was evaluated at the follow up appointment approximately two weeks after discharge. The outcome used in this study was based on clinical observation at the time of follow up with an emphasis on the improvement in gait as this is the most likely symptom to improve.[127] Furthermore, the patients were divided into non-responders and significant responders based on the clinical observations.

(3) Statistical Methods

For each of the aforementioned ICP features (mean ICP, waveAmp, and P3Ratio) the non-responders and significant responders were compared using the Wilcoxon Rank sum test with a significant level of 0.05 in MATLAB 7.5 R2007b (The MathWorks, Inc., Natick, MA, USA). As an additional level of significance testing a surrogate dataset was compiled and tested against. First, the binary outcome from the non-responders and the significant responders were randomized and the Wilcoxon Rank sun test was repeated. The value was stored and due to the sheer number of possible combinations, the surrogate data set consisted of one million iterations. If the true configuration has a p value (from the Wilcoxon Rank sun test) smaller than 95% of the surrogate set, than the original set was considered significant. This is merely an additional level of testing to show that what we have found is not random chance of the assignment of the binary outcome.

C. Results

1. Individual MOCAIP Feature Functions

Of the 54 patients studied, 12 patients (7 males and 5 females) showed no improvement in gait following the procedure. Panel F of **Figure 5** displays ROC curves

of each of the 128 metric-features (average feature function is used here as an example). The ROC curve shown in bold represents the metric with the greatest AUC; which was selected as the optimal metric-feature for rule construction. The ROC curves of optimal metric-pair corresponding to each of the five feature functions (A: Average feature function; B: Standard deviation feature function; C: Percentage of average feature function; D: Percentage of 5-minute standard deviation feature function; E: Inter 5-95 percentile feature function) are shown in Panels A through E of **Figure 5** where the selected MOCAIP metric is also spelled out. On each curve, the operating point is circled, which corresponds to the particular threshold value selected for rule construction.

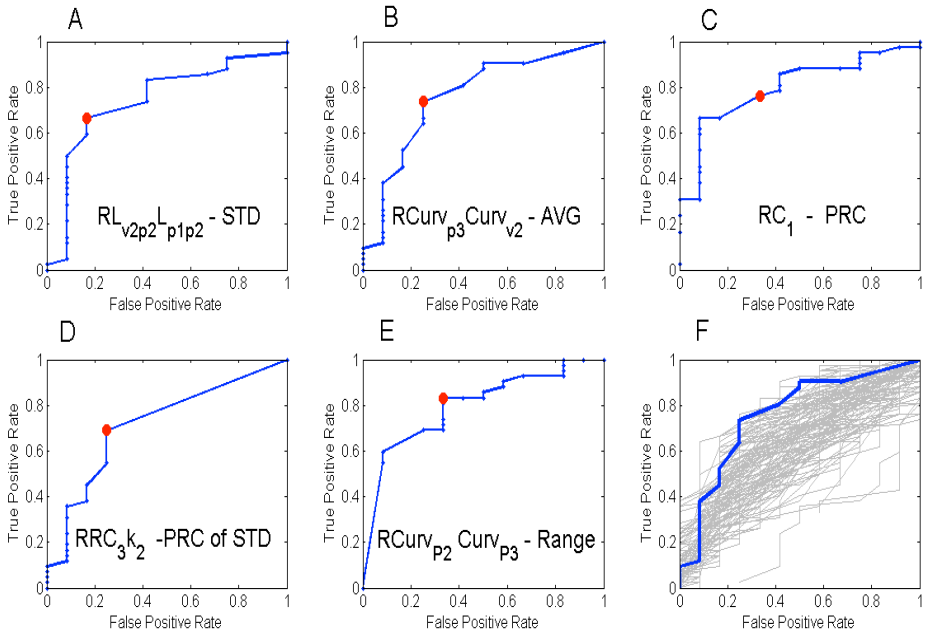

Figure 5: *Receiver operating characteristic (ROC) curves. Panels A through E display the ROC of the optimal metric-feature for each of the five individual feature functions.* ***A:*** *Average feature function;* ***B:*** *Standard deviation feature function;* ***C:*** *Percentage feature function;* ***D:*** *Percentage of standard deviation feature function;* ***E:*** *Range feature function.* ***Panel F*** *displays the ROC curves for the 128 metric-feature (for panel B) using the average feature as an example where the bold curve corresponds to that of the optimal metric-feature.*

Figure 6 demonstrates the impact of the optimal metric selection; for each of the combination rules (“AND” and “OR”) the accuracy is plotted as a function of the rank of the AUC. The decreasing trend of the accuracy for both “AND” and “OR” combination is clearly present. In summary, the individual metric-feature rules found in the present work are:

1) If standard deviation of RLv2p2Lp1p2 of overnight ICP recording is > 0.0547, then patient will respond to LD.
2) If average RCurvp3Curvv2 of overnight ICP recording is > 0.9808, then patient will respond to LD.
3) If percentage of RC1 of overnight ICP recording greater than 8.76 is < 41.48%, then patient will respond to LD.
4) If percentage of 5-minute segments of ICP having a standard deviation of RRC3k2 greater than 57.68 is > 0.49%, then patient will respond to LD drain.
5) If the inter 95-5 quartile range of RCurvp2Curvp3 of overnight ICP recording is < 64.25, then patient will respond to LD.
6) The accuracy for the corresponding features is: 70.4%, 72.2%, 74.1%, 72.2%, and 79.6% respectively. Finally, the OR combination of rules 4 and 5 achieves the best accuracy of 88.9%.

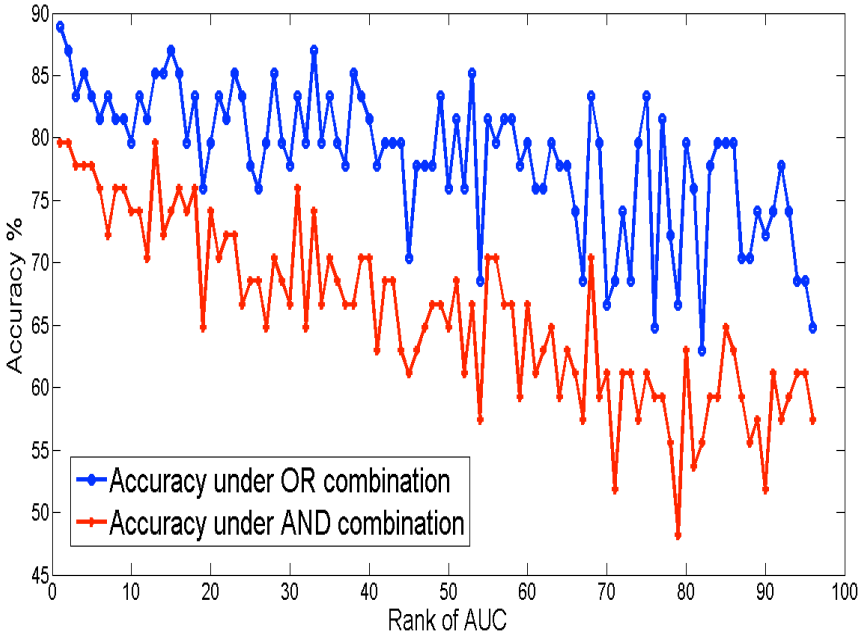

Figure 6: *Accuracy of the combined rules as a function of the rank of AUC of the selected metric-feature as the single-metric constituents for rule combination. A clear deterioration of the accuracy as metric pairs with smaller AUC are selected for rule combination demonstrating the optimality of choosing the one with maximal AUC. In other words, selecting metrics based of maximal AUC produces optimal results when combining signal metrics. Reproduced with permission Hu et al.*[45]

2. P3 elevation

For the 66 patients there were a total of 75,670 dominant ICP pulses, with an average and standard deviation of 1146.5 ± 394.9 dominant pulses per patient. Of the 66 patients, seven were classified as non-responders and 25 as significant responders based on the follow up clinical notes, the remaining patients were classified as intermediate (n= 34).

The mean ICP and waveAmp did not vary significantly ($p = 0.47$ and $p = 0.19$, respectively) between the outcome groups; however, the measure of P3 elevation (P3ratio) did show a significant difference ($p = 0.04$). The ICP morphological metrics

(median and interquartile ranges) and demographic information are shown in **Table 1**.

The violin plots of the three ICP features are shown in **Figure 7**.

	ICP Morphological Metrics			Demographics	
Groups (n)	**Mean ICP (mmHg)**	**WaveAmp (mmHg)**	**P3Ratio**	**Age**	**Sex M/F**
Significant responders (25)	4.7 [3.6]	5.0 [1.5]	0.70 [0.11]	71.7 ± 10.0	16/9
Non-responders (7)	3.8 [3.9]	5.5 [1.5]	0.80 [0.09]	74.6 ± 7.4	5/2
P value	0.47	0.19	0.04	0.48	N/A

Table 1: *For the ICP morphological metrics the average median value and [interquartile range] are given for the significant responders and non-responders. The p values reported are between the significant responders and the non-responders using the Wilcoxon Rank sun test. For the age of the three groups the mean ± standard deviations are given.*

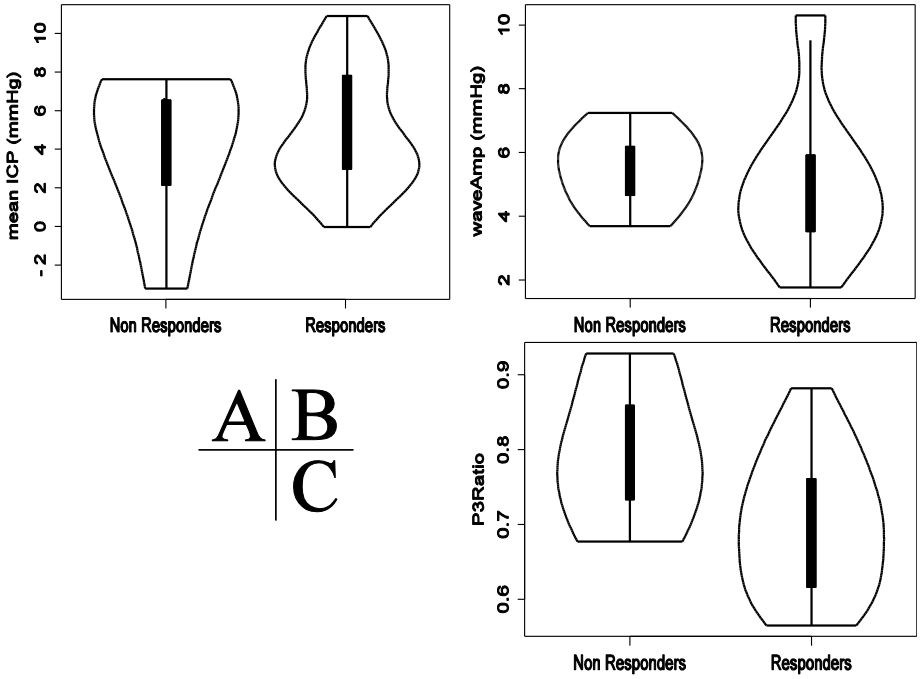

Figure 7: *Violin plots for non-responders, intermediate, and significant responders **A)** mean ICP **B)** waveAmp **C)** P3Ratio. Only P3Ratio was found to be significant when comparing significant responders and non-responders.*

The number of non-responders (7) and significant responders (25) resulted in a large number of possible combinations, therefore the surrogate data was constructed with one million iterations (randomizations of binary outcome). The p value reported for the clinical data set was smaller than over 96% (0.0338) of the iterations, supporting the significant finding between the two groups based on the clinical notes. A distribution of the surrogate data's p values are shown in **Figure 8** with the p value for the true clinical notes is also shown.

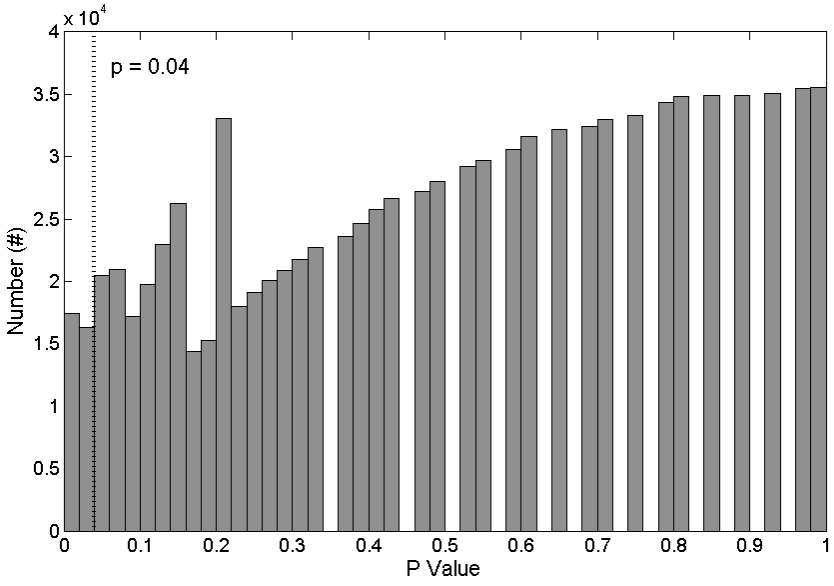

Figure 8: *Distribution of p values from Wilcoxon Rank sum test for the surrogate data. The p-value from the true test (where the binary values were not randomized) is less than 96% of the randomizations. We therefore can interpret the results as a true significant finding and not simply chance.*

D. Discussion

ICP morphology has been underutilized in the diagnosis and prognosis of several neurological conditions. With the recent advances in signal processing technology by our group[38] and others[37], ICP morphological metrics have revolutionized the diagnosis

of NPH,[40,42,43] TBI,[51] and SAH[53] with several other conditions currently being studied. The ability to accurately select NPH patients that benefit from CSF shunting has eluded clinicians and researchers for decades. In this chapter, two novel applications of advanced ICP morphological metrics for predicting the outcome of an ELD trail for NPH patients using overnight ICP waveforms were outlined.

1. Individual MOCAIP Feature Functions

We have demonstrated a systemic way of deriving two-rule combination of simple decision rules from overnight ICP recording to predict the corresponding outcome of ELD for patients with NPH clinical triad undergoing pre-shunt evaluation. Using a cohort of 54 patients, we were able to find optimal two-rule combination that reaches an accuracy of 88.9%, with the added advantage of ready communication with non-technical clinicians and patients using simple English. Although further validation with large patient cohort is needed, the rules found in the present work, in combination with an automated analysis of overnight ICP using the existing MOCAIP algorithm, can readily be built into a decision support system of NPH diagnosis and evaluation that has the potential to reduce the time and cost associated with the existing ELD procedure.

A systemic way of discovering predictive rules is needed, if a large number of ICP pulse morphological metrics are involved to construct rules. Compared to the existing studies that focus on either mean ICP or ICP pulse amplitude (waveAmp), the increased number of ICP metrics demands an objective way of discovering rules to guarantee optimality and avoid bias. Indeed, the five individual optimal metrics found in the present

work do not include either mean ICP or ICP waveAmp, demonstrating the potential power of adopting a more comprehensive ICP pulse morphology characterization.

The proposed rule discovery framework can be easily extended in several aspects. We have proposed five simple feature functions to summarize an overnight ICP recording. More complex feature function can certainly be implemented in future work. In particular, we believe that feature functions characterizing the relationship among MOCAIP metrics could potentially offer better predictive power as compared to single-metric feature functions used in this study. Furthermore, we have only studied the combination of two rules, one could readily derive the equations to calculate the accuracy of combining multiple rules and check if the predictive accuracy can be further improved.

One fundamental limitation of the present work is the lack of cases to conduct independent evaluation of the discovered rules. It remains to be demonstrated whether the same level of predictive accuracy can be retained when applying the rules discovered using our dataset to process data from other centers and how the data from multi-centers can be utilized to refine the rules. The present work has clearly demonstrated the technical feasibility of such future studies. More precise and robust predictive rules can be discovered through multi-center collaboration and the adoption of advanced ICP signal analysis and data mining methods.

2. P3 Elevation

The next advanced morphological metric investigated in this chapter is the P3 Ratio, which unlike a majority of the current MOCAIP metrics, has a physiological basis. As previously mentioned, the ability to accurately select NPH patients benefiting from CSF shunting has eluded scientists/clinician/etc. for decades. Although established methods like ELD report high prognostic accuracy, most are expensive and put the patient at increased risk of infection.[144] Previous overnight ICP attempts have focused on mean pressure (mICP), presence of slow wave activity,[16-18] and more advanced ICP features,[37] these results, however, remain controversial. In this study of overnight ICP morphological metrics, we introduce novel, physiologically based, ICP features that differentiated ELD responders over more traditional clinical measures of ICP pulse pressure waveform.

a) P3Ratio

One common criticism of morphological metrics is the lack of a physiologic origin. Recent work by our group has suggested possible links between the morphological metrics and specific physiologic origins.[47,145] Furthermore, a recent study by Hu et al., ICP waveform morphology metrics were shown to have higher accuracy when detecting low CBF (20 mL/min/100g) verse TCD and blood analysis combined.[47] Although the foundation of the previous study was data-driven through interpretation of the results the elevation of the third peak of the ICP waveform (dP3) was identified to correlate with low cerebral blood flow. Results from the study are shown in **Figure 9**. In comparison to the Hu et al. results[47] selected waveform comparisons for two NPH non-responders and two significant responders are shown in **Figure 10**, which shows an increased P3Ratio for

non-responders (**Figure 10A** and **10C**) verse significant responders (**Figure 10B** and **10D**). From this data-driven approach used by Hu et al., we developed P3ratio to specifically test this hypothesis in NPH prognosis.

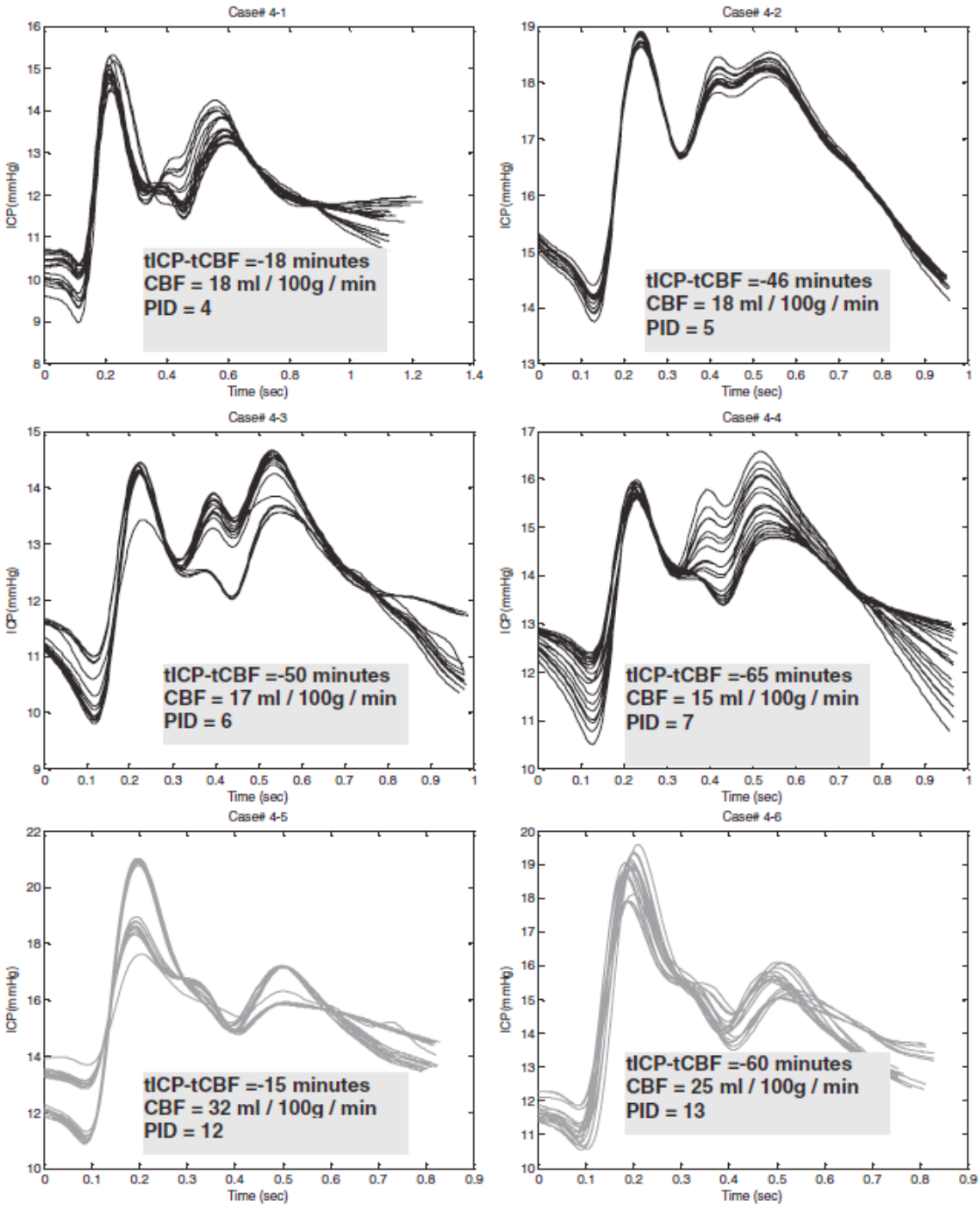

Figure 9: *Comparing dominant ICP pulses from six recordings of patients with ICP recordings and CBF measurements. PID: post injury day when the measurement was taken. It can be observed that the* ***elevation of the third peak is associated with low CBF****. This pattern was observed in six out of eight patients, who had at least one low CBF measurement. Reproduced with permission from Hu et al.*[47]

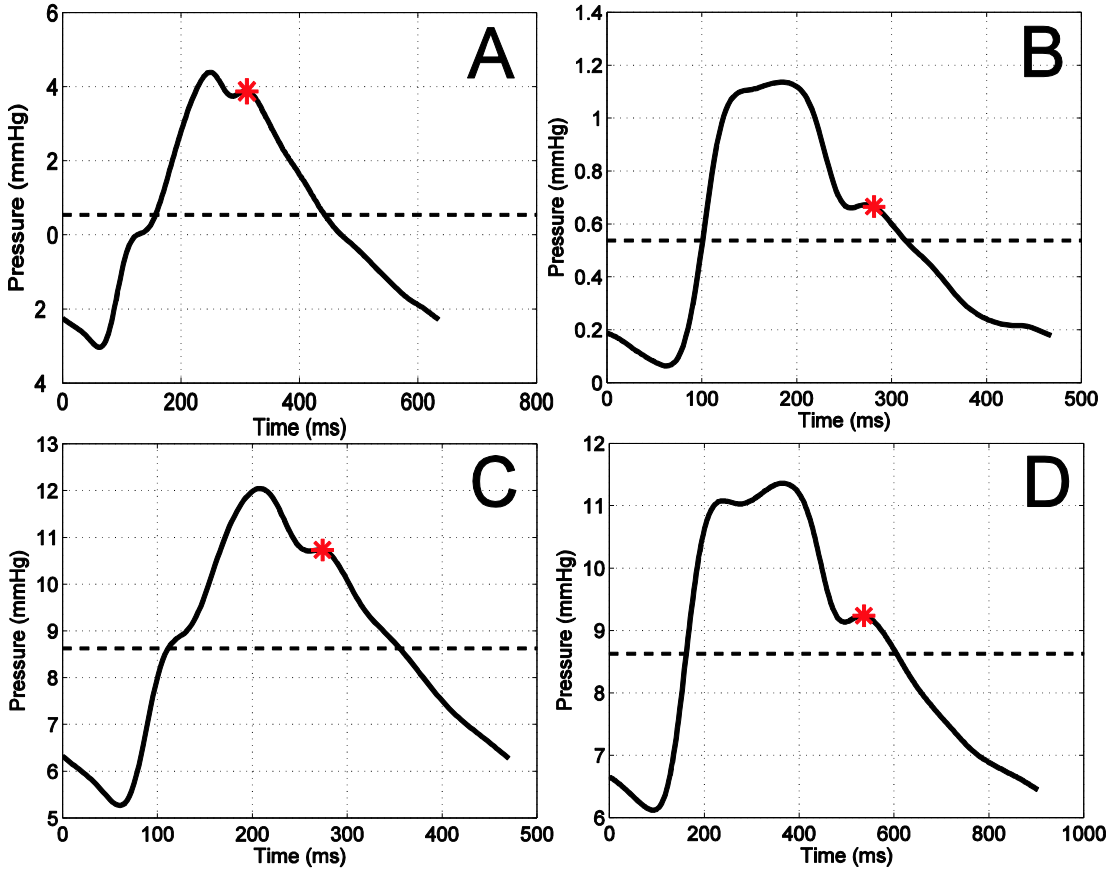

Figure 10: *Examples of dominant pulses from four patients, two non-responders and two significant responders. Each set has equal mean ICP values.* ***A)*** *Non-Responder with relative high P3ratio (0.93) and mean ICP of 0.54 mmHg (dotted line) is compared with a dominate pulse of a significant responder* ***B)*** *with relatively low P3Ratio (0.57) and mean ICP of 0.54 mmHg.* ***C)*** *Non-Responder with P3Ratio of (0.80) and mean ICP of 8.6 mmHg and* ***D)*** *significant responder P3Ratio (0.60) and mean ICP of 8.6 mmHg. Characteristic third peak determined by MOCAIP is marked by the *.*

Physiologically, the ICP pulsations have been long attributed to both arterial and venous components. [120,146] Adolph et al. used surgical interventions to differentiate arterial and venous contributions to the CSF pulsations in the cisterna magna.[146] The study concluded that although a majority of the CSF pulsations have the arterial system as an origin, there is a venous component. In later work by Cardoso et al., they attributed the third peak (P3, or dicrotic wave) to changes in venous pressure. This work suggests

that the changes we found between significant responders and non-responders could represent changes in venous pressure, possibly impacting cerebral perfusion pressure or some other pathological change in the venous system.

b) Cerebral Ischemia in Hydrocephalus

Using both global and/or regional CBF to diagnose NPH verse other forms of dementia, and normal controls along with predicting shunt outcome has been performed in a variety of different modalities, including ^{133}Xe clearance,[147-153] Single Photon Emission Computed Tomography (SPECT),

[154,155] Xe contrast CT,[153,156] PET.[157-159] Although there has been a study reporting no significance difference in CBF between NPH and controls,[160] a vast majority concluded there is some degree of ischemia in NPH.[147-156,159] Specifically, Momjian et al. investigated CBF in idiopathic NPH patients verse health controls using $H_2{}^{15}O$ PET.[159] They found that the NPH patient cohort had a significantly reduced global CBF (28.4 ± 5.2 ml/100 ml/min) when compared to the health controls (33 ± 5.4 ml/100 ml/min). The study also reported a significant decrease in global CBF in the NPH patients during CSF infusion test. Furthermore, they report the decreased CBF is more pronounced in the frontal region, which correlated well with other studies.[153,154,156] Finally, this paper concludes that the decreased CBF in the white matter, which was found when the PET images were co-registered, correlated well with other studies that have found increased white matter lesions in patients with NPH. Additional studies have attempted to tie changes in CBF to removal of CSF via CSF tap test, LD drain, or insertion of a shunt and outcome. Although some have shown a relationship between CBF and outcome following removal of CSF,[149,152] other have found no correlation.[161-163] The previously

mentioned studies demonstrate that NPH patients have lower blood flow verse controls, with a majority revealing the decrease is more pronounced in the frontal region and that these changes are detectable and significant during CSF removal. Unfortunately, the ICP monitor was removed shortly after the start of the ELD trials in our study, so we are unable to investigate changes in P3Ratio during CSF drainage.

c) Prognostic Value of CBF

In addition to using CBF as a diagnostic indicator of NPH, others have attempted to use CBF as a prognostic indicator for shunt outcome. Hayashi et al. investigated CBF and ICP in patients with secondary hydrocephalus following aneurysm rupture.[164] There were two main findings relevant to our study. First, of the 43 patients that underwent shunting for the hydrocephalus, no patient with a CBF of 25 ml/100g/min or less responded well. Secondly, the authors reported a correlation between ICP irregularities (aka B-waves) and CBF. In other words, in patients with no ICP irregularities (no b-waves), there was a lower mean CBF and, thus, patients were less likely to respond to shunt treatment; this result correlates well with selected studies, which suggest that the increased presence of ICP slow waves predict a positive outcome after shunting.[16,165] Although we did not measure CBF in our study, the ICP morphological metric P3ratio demonstrated the analogous results, which suggests that once the elevation reached a certain threshold (or higher in the case of P3Ratio), there is irreversible damage and the shunting has little or no impact. These results were echoed in another study by Tanaka et al. investigating the prognostic ability of CBF on 21 NPH patients.[166] The studied determined a threshold of 20 ml/100g/min as a threshold for improvement, where again patients with blood flows below the given threshold failed to respond to shunting. Both

thresholds for improvement (25 and 20 ml/100g/min) correlated well with the value of CBF in our previous publication using ICP waveform morphology to differentiate ischemic states in severe brain injury patient.[47] In a conflicting study, Klinge et al. suggested the opposite trend: patients with lower CBF (36 ± 7 ml/100g/min) were more likely to respond than those with high flow measurements (44 ± 8 ml/100g/min).[158] Upon closer inspection, the CBF values reported in this study did not eclipse the aforementioned thresholds and, therefore, might be difficult to compare to one another. Finally, there have been a series of studies that found no prognostic value in measuring per treatment CBF.[161,162] Summarizing the findings of the aforementioned studies: the Hu et al. study suggested a high P3 elevation is related to low CBF, in the Tanaka et al. and Hayashi et al. papers results demonstrated NPH patients are less likely to respond to shunt if they call below a given CBF threshold, and our study reinforces these findings by suggesting a high P3Ratio (which correlates well with low CBF) is associated with non-response to CSF drainage.

d) ICP as a Prognostic Indicator of Shunt Outcome

More directly linked to our study are the several attempts to use overnight ICP monitoring as a prognostic indicator of shunt outcome in NPH patients. As mentioned previously, several authors have attempted to use slow waves (Lundberg B-waves[11]) to differentiate shunt responders and non-responders. A few studies have suggested increased slow wave activity correlated with positive outcome;[16,165,167] however, others report no correlation.[17,18] Another popular ICP derived feature is CSF outflow resistance (R_o); however, it has yet to show sufficient evidence for wide adoption and requires additional procedures.[102]

The previously mentioned methods do not utilize ICP waveform morphology specifically, but make inferences about the physiological state from the either the mean ICP or slow wave activity. Recent advances in ICP morphology allow for an entirely new set of variables to be explored. Eide et al. reported a sensitivity and specificity of 98% and 70%, respectively, for an average waveAmp greater than 4 mmHg combined with 10% of the recording time greater than 5 mmHg suggesting positive outcome following CSF shunt.[43] This group has also extended the use of waveAmp to SAH, which has shown positive results when compared to traditional mean ICP management.[54] In the data-driven approach outlined earlier in this chapter, differentiating ELD responders using overnight ICP percentage of waveAmp and average values were not shown to be predictive of outcome; however, using simple combinations of ICP features obtains an accuracy of 89%.[45] Furthermore, the current results suggest that waveAmp alone cannot differentiate shunt response, with average overnight values both above 5 mmHg and statistically non differentiable ($p = 0.19$, **Table 1**). Our data suggest that the advanced ICP morphological feature P3Ratio can provide additional evidence to differentiate significant responders from non-responders. Although the pure data-driven approach obtained a high accuracy (89%), the current study has a physiologic foundation (low CBF), which Marmarou et al. recommended in recent NPH guidelines.[103]

Finally, we made an economic comparison between ICP and ELD. Seven additional, probable NPH patients' overall hospital costs were obtained with consent, showing an average cost of the ELD trial alone was \$25,134 ± \$2,054. For five of the patients that

received ICP monitoring and ELD trial, the average cost reported was $34,724 ± $4,390 resulting in a an average cost of ICP monitoring of approximately $9,600, which represents greater than 60% potential reduction in cost by replacing ELD by ICP monitoring alone. Although patient safety is the top priority of any institution, the economic impact of different procedures remains obvious and noteworthy.

e) Limitations of our study

Klinge et al. emphasized the inconsistent assessment of outcome in retrospective NPH studies and the need to standardize how and when outcome is assessed; furthermore, they noted life expectancy and co-morbidities increase the difficulty of accurate outcome assessments.[168] For this reason, our study investigated outcome assessed by clinical notes during the two week follow-up after ELD. Although more objective measures of outcome are recorded during baseline, discharge, and follow-up, much of that data was incomplete. Variables include Mini-Mental State Examination (MMSE), 10m walk, clinical scale, and a patient questionnaire for pre-ELD, post-ELD, and two week follow-up. Unlike the aforementioned variables, the clinical follow-ups for the ELD were all performed by one clinician (PV). The evaluation to segment the groups into non-responders and significant responders was based off observations in the clinical notes, where there seemed to be a clear division between patients that responded well (significant responders), those who had slight improvement, and those who had no improvement at all.

E. Conclusion

The studies outlined in this chapter focus on the ability of advanced ICP morphology to predict ELD outcome in NPH patients. The studies utilized overnight ICP recordings

from Pre-LD NPH patients using different approaches that aim to develop a safer, more economical method for recommending CSF shunts. Although both studies had positive results, the development of the P3 Ratio as a novel prognostic metrics shows the most promise as the physiological foundations in low CBF, making it more attractive than the data-driven approach described early in this chapter. Although additional work needs to be done for adoption of P3Ratio as a clinical metric, initial results are promising.

VII. Chapter 4

A. Introduction

The objective of this chapter is to investigate the relationship between intracranial pressure (ICP) pulse waveform morphology and selected hydrodynamic metrics of cerebrospinal fluid (CSF). The motivation for this work stems from a long-term goal to advance ICP monitoring by delivering more clinically useful metrics in addition to mean ICP (mICP), which remains the only parameter reported to clinicians by current ICP monitors. To reach this goal, our group and other colleagues have done a series of work in advancing the techniques of ICP signal analysis. One specific example is the Morphological Clustering and Analysis of Continuous Intracranial Pulse (MOCAIP)[38] algorithm, which has been referenced throughout this thesis. As a reminder, MOCAIP can robustly identify the locations of the three sub-peaks and valleys of an ICP pulse and then systematically extract 128 metrics that characterize the amplitude, curvature, slope, and time intervals among these landmarks. Several studies have been performed which show the benefits ICP morphological analysis and the MOCAIP algorithm; however, a majority of this work lacks a physiological basis for their findings. Presented in this chapter are two studies which extend MOCAIP analysis to infer relationships for the different sub-peak regions and individual metrics in the triphasic ICP waveform, which we believe will lead to a greater physiologic understanding of the ICP pulse pressure waveform and thus a more advanced ICP monitoring system.

To test the ability of the MOCAIP metrics to characterize different sub-peak regions of ICP, we have selected three noninvasive hydrodynamic variables measured by phase

contrast MRI (PC-MRI) in the cerebral aqueduct and the prepontine cistern, which were discussed in Chapter 2. The aqueduct and cistern represent locations in two complementary compartments of the cranial vault, the ventricular system and the subarachnoid space, respectively. Our objective is to determine if the CSF hydrodynamics metrics from the aqueduct and cistern are significantly related to specific features or regions in the ICP pulse pressure waveform.

Here, we examined the possible relationship between ICP waveform morphology and MRI CSF flow dynamics in a group of hydrocephalus patients. We hypothesized that morphological metrics of the ICP waveform are related to the hydrodynamics of CSF flow. To investigate this claim, we designed two studies, one which looks at the broad aspects of the three characteristic regions of the ICP pulse pressure waveform and the second which investigates specific metrics of the individual peaks.

1. Study 1: Sub-peak Regions

First, ICP pulse waveform morphology can be segmented based on the peaks into three specific regions (Region1, Region2, and Region3). Using the individual MOCAIP metrics to define a new coding strategy, we investigated the broad correlation between ICP pulse pressure regions and CSF flow in the cerebral aqueduct and the prepontine cistern.

2. Study 2: Characteristic Peaks

The second study takes a slightly different approach by looking at specific features related to the characteristic peaks. We hypothesize that P2 peak would be more closely tied to measures of aqueductal CSF flow than the other ICP peaks (P1 and P3).

B. Methods

The studies in this chapter use identical patient populations so a general description of the data is provided first.

1. Patient Characteristics & Data Acquisition

While under evaluation for NPH at the UCLA Adult Hydrocephalus Center, seven patients (71.1 ± 9.8 years) received both overnight ICP monitoring and a PC-MRI CSF flow protocol. Patients were recommended for extended lumbar drain (ELD) trial based on presence of the NPH clinical triad (gait ataxia, urinary incontinence, and dementia); however, progressive gait ataxia was the most common symptom. All ICP sensor and data acquisition (both imaging and pressure monitoring) were approved by the local IRB committee and all subjects signed informed consent to participate. All measurements were taken while the patient was in the supine position.

a) Overnight ICP Monitoring

During the overnight monitoring, patients assumed a supine or near supine position. An intraparenchymal ICP microsensor (Codman and Schurtleff, Raynaud, MA) was inserted in the right frontal lobe and continuously monitoring ICP for one night before the placement of the lumbar drain (LD). Continuous waveform data, including ECG and ICP, was captured using the BedMaster^{TM} system (Excel Medical Electronics, Inc Jupiter, FL) with a sampling rate of 240 Hz. Following overnight monitoring, the

intraparenchymal ICP monitor was removed and the patient transitioned into the ELD trial.

b) Phase-Contrast MRI Protocol

Seven patients (71.1 ± 9.8 years) received the imaging protocol, which either preceded admission for ELD or followed the ELD by no less than three weeks; which allowed for equilibration of the baseline hydrodynamics. For patients that had temporarily improved after the ELD trial, all had completely reverted back to their original state at least two weeks prior to the MRI study. Patient manuscript ID, age, and sex characteristics are shown in **Table 1.** All patients showed temporary improvement from ELD along with an average Evan's ratio of 0.35 ± 0.04. All MRI scans were performed using a 3-Tesla Siemens Trio T-class MRI (Sienmens Medical Systems, Erlanger, Germany). Using a Siemens Head Matrix birdcage head coil, the participants were placed in the supine position with their neck and head in the neural position. Phase-contrast imaging took place in the cerebral aqueduct and prepontine cistern shown in **Figure 1** (prepontine cistern was only studied in Study 1). The imaging protocol contained both anatomical and flow quantification sequences. The standard anatomical sequences included a 3D axial T1-weighted MPRage, axial T2-weighted BLADE, and a sagittal T2-weighted TSE. Image parameters are shown in **Table 1** of **Chapter 2**.

Patient Index	Age (Years)	Sex	Time Between Measurement (Days)
1	73	Male	-4
2	74	Male	0
3	79	Male	0
4	84	Female	-6
5	58	Male	+33
6	58	Male	+24
7	72	Male	+32

Table 1: *General patient characteristics including patient index, age, sex, and time separation between the MRI scan and overnight ICP monitoring in days. Negative values represent MRI study prior to ICP monitoring. Again, for MRI scans following ELD trial and ICP monitoring (positive values), at least 3 weeks separated the two measurements to allow for baseline hydrodynamics to return.*

Flow quantification was achieved using a standard phase contrast sequence. An oblique plane was defined perpendicular to the presumed direction of CSF flow (**Figure 1**). The velocity encoding parameter (V_{enc}) was set with the aid of a flow scout in order to reduce aliasing. Following the definition of the V_{enc}, the phase contrast sequence was applied. The average and standard deviation of the V_{enc} for the seven patients was 17.4 ± 4.4, respectively. Finally, a temporal resolution of 30 frames was defined by retrospectively gating with either ECG or pulse oximetry signals.

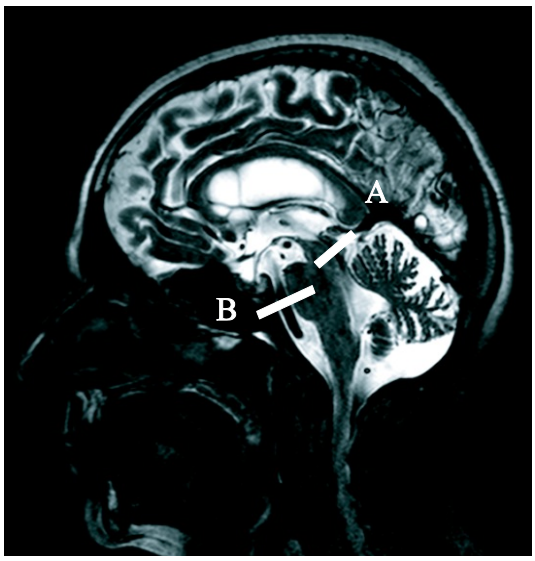

Figure 1: *Location of the oblique slices for the PC-MRI study, A) cerebral aqueduct and B) the prepontine cistern.*

2. Data Analysis

a) Study 1: Sub-peak Regions

(1) CSF Hydrodynamic Analysis

The semi-automated segmentation algorithm was implemented in MATLAB 7.5 R2007b (The MathWorks, Inc., Natick, MA, USA) to define the region of interest (ROI) for both anatomical locations and was described in detail in Chapter 2.[128] Next, three CSF hydrodynamic metrics were calculated based on the extracted ROI, including the peak velocity, the peak to mean flow, (P2P Mean Flow) which represented the absolute mean difference between the average flow rates in the caudal and cranial directions, and the average stroke volume, defined as the average volume of CSF moving cranial-caudal during systole and caudal-cranial during diastole.

(2) ICP Analysis

The ICP analysis was performed using the MOCAIP algorithm developed by our group using MATLAB 7.5 R2007b. A complete description of MOCAIP can be found in

Chapter 3;[38] however, a brief description follows. MOCAIP is an end-to-end framework devoted to real time time-domain analysis of intracranial waveform morphology. MOCAIP utilizes a five-step process to convert the raw ICP and ECG inputs into a series of clean ICP pulses, known as dominant pulses. First, the raw ICP data is segmented using the RR interval of the ECG signal. Following the segmentation, the individual pulses are grouped based on a pre-defined time interval (one minute in this study) and then clustered using a hierarchical clustering method. A dominant pulse is defined for each segment (one minute of raw signal) as the mean of the largest cluster. However, the dominant pulse produced could be an invalid ICP pulse because the entire segment could be noise; therefore, the segment's dominant pulse is checked against a reference ICP pulse library to determine the legitimacy of the pulse. Once the dominant pulse has been verified, six landmarks are determined: the three characteristic peaks and their corresponding valleys. Finally, the algorithm extracts 128 MOCAIP metrics based on the six landmarks for each dominant pulse. An example of the dominant pulse along with sub-peak regions are shown in **Figure 2**.

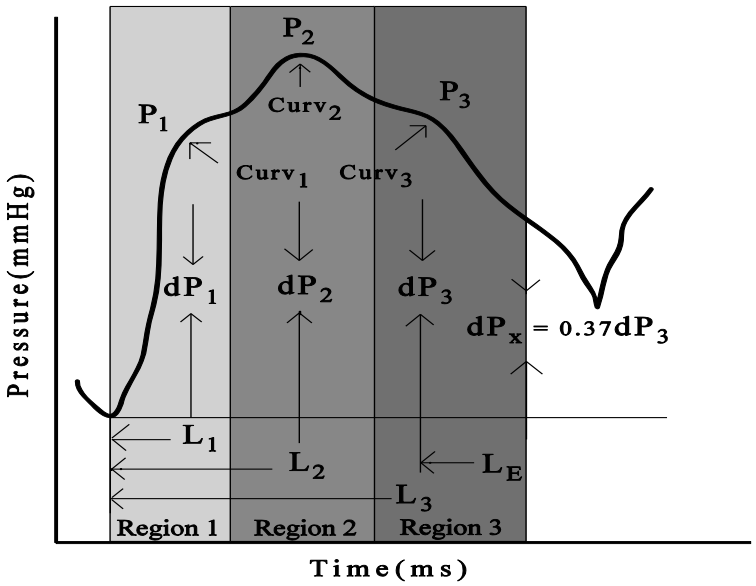

Figure 2: *MOCAIP example of a dominant pulse with metric identifies including amplitude, latency, and curvature. The regions are also shown in boxes*

(3) Description of Region Weight

Although physiologic relationships can be speculated from the individual metrics derived from the MOCAIP algorithm (Study 2), a more general analysis is possible. The MOCAIP metrics can be divided into sub-peak regions (region 1, 2, and 3), based on a binary scheme that characterizes each MOCAIP metric's dependency on three different sub-peak regions (**Figure 2**). For example, amplitude metric '**dP1**' (amplitude of the first peak) would be associated with a sub-peak region binary code (1 0 0) representing (region 1 region 2 region 3), where ratio metric **'RCurvp2Curvp3'** (ratio between curvature of peak 2 and curvature of peak 3) would be assigned a code (0 1 1). The sub-regions are not uniformly distributed, with region 1, 2, and 3 having an approximate distribution of 35.6%, 33.2%, and 31.2%, respectively.

(4) Correlation of ICP Metrics and MRI metrics

Following calculation of the metrics sets (PC-MRI and ICP), Spearman's rank correlation coefficient (ρ) was used to quantify the dependencies of the ICP metrics and the hydrodynamic metrics derived from PC-MRI. In other words, each ICP metric (128 metrics, each with a three digit binary region code) was compared to the six of the aforementioned PC-MRI metrics (three for each of the two locations) and the correlation coefficient was calculated.

Once the correlation coefficients were calculated for each pair of measurements, a threshold value (alpha) had to be determined to study the region contribution of those highly correlated metrics. Namely, each combination will have some correlation value; however, many of these will have correlation coefficients near zero and thus should not be included in the analysis. To investigate the region contribution of the CSF hydrodynamics metrics, an alpha value was determined ad hoc. At this value of alpha, a normalized region contribution (NRC) was calculated; for example, if three metrics had correlation values greater than alpha (dP1, Lv1p3, and mICP: (1 0 0), (1 0 1), (1 1 1), respectively) the NRC would be (47.2% 16.9% 35.9%). Obviously, the NRC is a function of the alpha value. The lower the alpha value the more metrics included in the NRC calculation. To account for this, the NRC was calculated for each alpha value from 0 to 1.0 (steps of 0.01) resulting in a percent region weight trend for each of the three regions. This plot aided in the selection of the final alpha value (**Figure 3**).

To summarize, each of the six CSF metrics were compared to the 128 ICP MOCAIP metrics and a correlation value was calculated. An alpha value was then determined based on the overall distribution of region weights (see **Figure 3**). This selection resulted in a small number of ICP metrics (N_{ICP}) that were greater than the alpha value. From the N_{ICP} metrics, an NRC was calculated.

(5) Significance Testing

For significance testing of the association between a CSF hydrodynamic metric and an ICP pulse sub-peak region, a surrogate data set was used with a significance level of 5%. For any given experiment, a number of metrics will be greater than alpha (N_{ICP}). For the surrogate testing, N_{ICP} metrics were randomly selected from the 128 metrics and the NRC was calculated. For example, if the following three metrics were selected (N_{ICP} = dP1, Lv1p3, and mICP) during the initial analysis (Spearman's value greater than alpha), then three metrics would be selected at random from the 128 overall metrics and the NRC would be calculated (N_{random}). To provide an adequate distribution, 10,000 random selections were made. If the NRC calculated from the data (N_{ICP}) was greater than 95% of the randomly generated surrogate data, it was considered significant.

b) Study 2: Characteristic Peaks

(1) CSF Hydrodynamic Analysis

For the imaging data, the semi-automated segmentation algorithm described in Chapter 2 was implemented for the designation of the region of interest (ROI).[128] The algorithm was developed using MATLAB 7.5 R2007b (The MathWorks, Inc., Natick, MA, USA), which utilized both anatomical and dynamic information from the phase contrast study. Following the extraction of the ROI, the hydrodynamic metric ASV was calculated as the

average volume moving in the cranial-caudal and caudal-cranial direction over the cardiac cycle.

(2) ICP Analysis

The ICP waveform morphology characterization was done using the MOCAIP analysis toolbox, which was described above and in detail in Chapter 3.[38] There were 2785 dominant ICP pulses analyzed for the patient population. The results had a mean and standard deviation of 397.9 ± 95.8 dominant pulses per patient, with a range from 209 to 503 pulses.

(3) Correlation of ICP Metrics and MRI metrics

For the individual dominant pulses, we focused on nine temporal metrics and two common amplitude metrics. The small subset of temporal metrics was chosen to specifically investigate the relationship of the three characteristic peaks and the amplitude metrics (mean ICP and ICP pulse pressure wave amplitude) are commonly used as the gold standard measurement in ICP monitoring/analysis. For the temporal metrics, we investigate three physiologic parameters related to each of the three characteristic pulses giving a total of nine metrics. The three physiologic parameters are the rising time of the leading edge (the time between the preceding valley and subsequent peak), the time of the falling edge (the time from the peak to the following valley), and finally, the time between subsequent valley points represents the width of the peak. Mean ICP (mICP) and the ICP pulse pressure amplitude (waveAmp) were chosen as the amplitude metrics for this study.

(4) Significance Testing

Following calculation of the metrics sets (PC-MRI and ICP), Spearman's rank correlation coefficient (ρ) was used to quantify the dependencies of the ICP metrics and the ASV. Each patient's overnight ICP data contained several dominant pulses produced by the MOCAIP algorithm. Therefore, for the statistical comparison, the median values of the overnight metric (nine temporal and two amplitude metrics) were compared to the ASV imaging data. The overnight section of ICP data was selected based on relatively low noise compared with the day time hours and patient position (supine), this allowed us to remove any subjectivity in selecting specific segments of ICP and has been used in several studies.[22] Finally, to account for the multiple comparisons used in this study, the statistical level of 0.05 was altered based on the Bonferroni correction to 0.0045 based off the 11 metrics stud-ied. All statistical tests were performed in MATLAB 7.5 R2007b.

C. Results

1. Study 1: Sub-peak Regions

For the seven patients, a total of 2,785 dominant ICP pulses were analyzed. The results had a mean and standard deviation of 397.9 ± 95.8 dominant pulses per patient, with a range from 209 to 503 pulses. The PC-MRI results for the CSF hydrodynamics are shown in **Table 2**.

	Aqueduct	Cistern
Peak Velocity (cm/s)	13.24 ± 4.37	5.54 ± 2.48
P2P Mean Flow (mL/min)	2.99 ± 1.01	1.20 ± 0.77
Stroke Volume (mL)	0.16 ± 0.04	0.24 ±0.09

Table 2: *PC-MRI results for the four CSF hydrodynamic parameters for each anatomical location (mean* ± standard deviation)

a) Regional Analysis

For the aqueduct, all three of the CSF metrics reached significance in regional testing. Peak velocity, P2P Mean Flow, and the aqueductal stroke volume (ASV) were all significantly correlated with region 2 (**Table 2**). Although the individual ICP metrics (N_{ICP}) are not reported for each significant correlation it is worth noting that mICP was not included; however, the amplitude of the ICP pulse pressure (waveAmp) was selected for the ASV and peak velocity.

The prepontine cistern had two CSF metrics reach significance (peak velocity and P2P Mean Flow). Although the stroke volume did not reach significance it maintained the same tendency toward region 3 as the other metrics. Again, mICP was not included as one of the significant ICP metrics.

b) Threshold Selection

The threshold selection process was based on the trend of the NRC for each alpha value ranging from 0 to 1.0 (**Figure 3**). Each alpha value in the trend plot has a number of metrics associated with it (N_{ICP}); this is not represented in the figure but is critical for significance testing. The individual alpha values have no physical representation but are reported for completeness in **Table 3**. An example of the aqueductal P2P Mean Flow regional contribution (percent region) as a function of alpha value is shown in **Figure 3.**

	Aqueduct		Cistern	
	Alpha	Region	Alpha	Region
Peak Velocity	0.79	2**	0.64	3*
P2P Mean Flow	0.83	2**	0.46	3*
Stroke Volume	0.58	2*	0.50	3

Table 3: *Metrics for ICP, PC-MRI, and TCD that were used in the region analysis. Each noninvasive metric (PC-MRI and TCD) was compared against all 128 MOCAIP metrics. *P-value < 0.05 and ** P-value < 0.001*

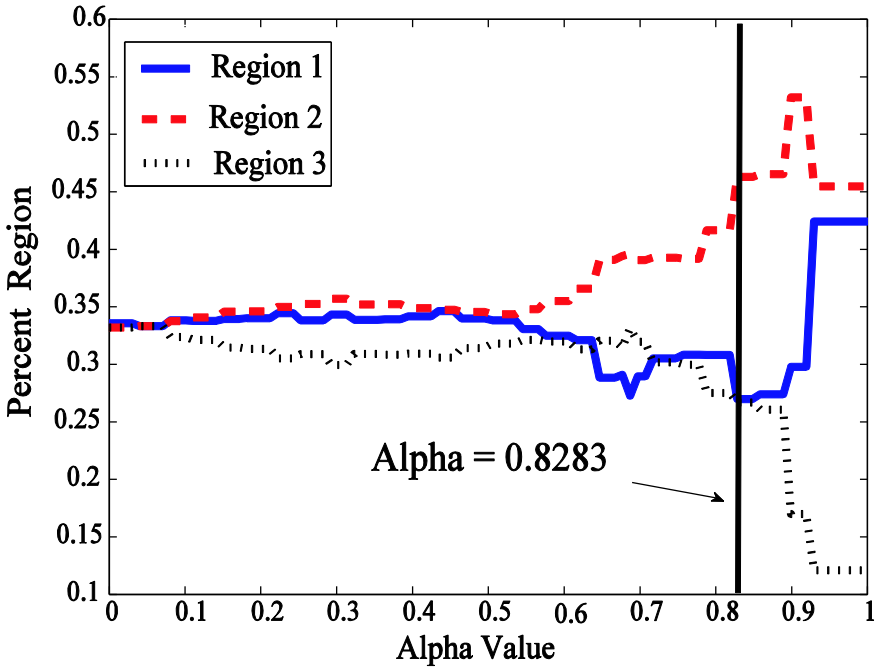

Figure 3: *Percent region contribution as a function of the alpha value. The plot represents P2P Mean Flow in the cerebral aqueduct. The respective alpha value (where the significance testing was performed) is shown with a vertical line.*

2. Study 2: Characteristic Peaks

The ASV for the seven patients had a mean and standard deviation of 0.156 ± 0.043 mL, respectively. These values compare well with previously published ASV for NPH patients.[106,123] The age of the patients did not show any significant relationship for either the ASV or ICP metrics.

The correlation values between the ICP temporal metrics and PC-MRI ASV metric are shown in **Table 4**, with significant values marked with an asterisk for *p*-values less than 0.0045 (Bonferroni correction). Of the nine temporal metrics correlated with the ASV, only the width of P2 (ICP-W_i2) was significantly correlated (p = 0.0025); however, the rising edge of P2 (ICP-W_i2^+) trended toward significance (p = 0.0068). Examples of selected metrics (peak widths) are shown in **Figure 4A-C**; along with a linear fit of the variables and a 95% prediction interval. Also shown in **Figure 4D** is a sample ICP pulse pressure waveform that depicts the definitions of the studied temporal metrics. Both the ICP pulse pressure amplitude (p = 0.023) and the mean ICP (p = 0.6445) failed to reach the corrected significance level (**Figure 5**).

	P1		**P2**		**P3**	
Metric Type	Metric	**ρ**	Metric	**ρ**	Metric	**ρ**
Rising	ICP-W_i1^+	-0.5	ICP-W_i2^+	0.9	ICP-W_i3^+	-0.1
Falling	ICP-W_i1^-	-0.3	ICP-W_i2^-	0.7	ICP-W_i3^-	-0.1
Pulse width	ICP-W_i1	-0.6	ICP-W_i2	0.9*	ICP-W_i3	-0.1

Table 4: *Spearman's rank correlation coefficient (**ρ**) for the aqueductal stroke volume. The metrics are divided into three regions defined by the characteristic ICP pulse pressure waveform peaks (columns P1, P2, P3) and by temporal category (rising time, falling time, and peak width time). *Significant correlations (p<0.05)*

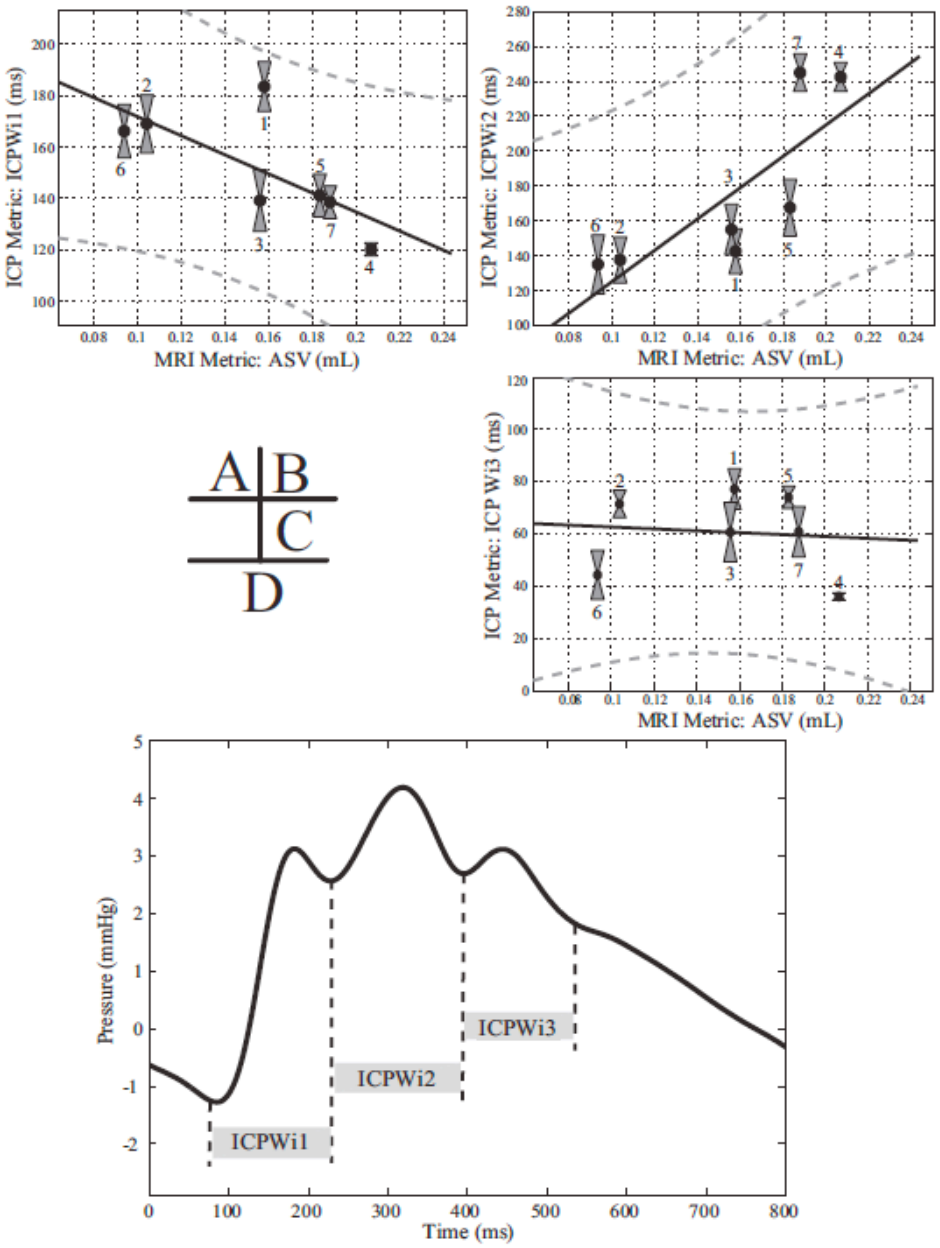

Figure 4: *Plots with linear fit and 95% prediction interval.* ***A)*** *ICP-Wi1 vs. ASV* ***B)*** *ICP-Wi2 vs. ASV* ***C)*** *ICP-Wi3 vs. ASV* ***D)*** *A sample ICP pulse pressure waveform with the corresponding temporal width metrics shown graphically. On figures A-C gray boxes show the standard deviation of the overnight ICP metrics along with the unique patient index defined in* ***Table 1****. Reproduced with permission from Hamilton et al.*[145]

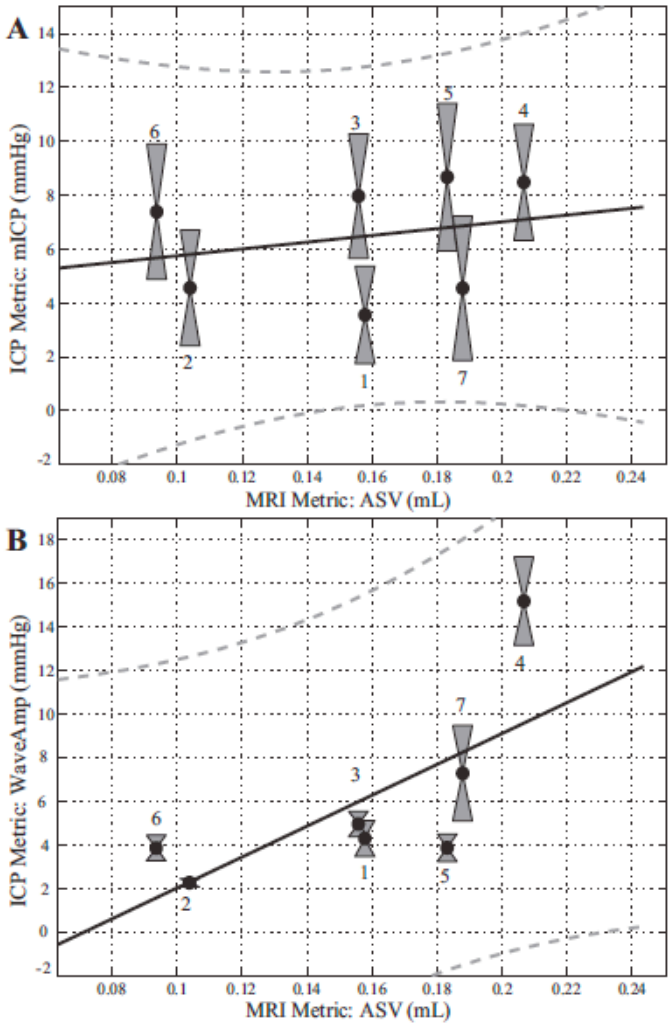

Figure 5: *Examples of **A)** mean ICP vs. ASV and **B)** waveAmp vs. ASV with the unique patient index defined in **Table 1.** Reproduced with permission from Hamilton et al.*[145]

D. Discussion

Both studies presented in this chapter investigate the role of CSF dynamics and ICP pulse pressure morphology. The results complement each other well showing a regional relationship between CSF flow in the aqueduct and Region2, with more detailed results showing the significant correlation between the width of P2 and CSF flow in the cerebral aqueduct. In addition to the common results of the studies, each study contributes something unique to the overall understanding of ICP pulse pressure morphology.

1. Study 1: Sub-peak Regions

The impact of this study is multifaceted, contributing both technically and physiologically to the study of ICP and cerebral dynamics. Technically, this study introduces a novel framework for generalizing the ICP morphological metrics produced by the MOCAIP algorithm into regional information based on the characteristic peaks. In this study, we proposed the use of CSF hydrodynamics measurements via PC-MRI; however, this framework could easily be expanded to include different measures of brain pulsatility. Physiologically, this work supports the idea that the global mean value of ICP and the characteristics of the three individual regions of an ICP pulse may reflect different aspects of the CSF dynamics and can provide complementary information. Such a finding therefore challenges the current paradigm of monitoring only mICP while ignoring the shape of an ICP pulse and could have a far reaching impact on the study of ICP waveform morphology in a variety of conditions.

a) Traditional Analysis of ICP

The MOCAIP algorithm provides a framework for the advanced analysis of ICP waveform morphology, which has been shown to be advantageous over the traditional mICP in several conditions. For example, Eide *et al*. has recently shown the prognostic value of ICP pulse amplitude for shunt outcome prediction in NPH patients. The work described in this study extends the morphological metrics by strategically segmenting the 128 metrics into regional contributions seen in **Figure 2**. This simple binary framework was developed to help elucidate some of physiological meanings of the MOCAIP metrics. The motivation behind this work is based on the classical studies of ICP waveform morphology that focused on the characteristic peaks.

b) Physiological Impact

The findings in this study provide additional evidence that the sub-peaks of the ICP waveform have physiologic meaning. There are several studies stating theories for each of the characteristic peaks. For P1 (percussion wave), a majority of the literature cites the pulsation of the large intracranial conductive vessels as the main driving force. The second sub-peak (P2) has been linked to capillary expansion. Finally, P3 is thought to be venous in origin. These results have been echoed in recent studies and are accepted as ICP dogma regarding the characteristic peaks.

A key finding of this work is that a significant association exists between CSF hydrodynamic measures from two distinct anatomical locations (aqueduct and cistern) and the sub-peak regions of the ICP pulse. The aqueductal CSF metrics were correlated with region 2 of the ICP waveform. One possible interpretation for these results is that the driving pressure required to displace an increased CSF volume through the aqueduct is related to the second peak of the ICP pulse. Another related theory proposed by Greitz *et al.* suggests that the aqueductal egress is predominantly caused by the brain expansion (capillaries). Therefore, the second peak of an ICP pulse may correlate with the arterial pulse wave reaching the level of the choroid plexus and/or capillary expansion in terms of the timing.

The results for the prepontine cistern are just as compelling with two CSF metrics significantly correlated with region 3. Traditionally, region 3 has been associated with the venous system. However, we know from previous studies by Greitz and Wagshul *et*

al. that the cisternal CSF pulse precedes the aqueductal pulse. Based on these studies the cisternal correlation with region 3 seems paradoxical as one might expect a correlation with region 1. We believe that these results can be explained by the pulsatile nature of CSF. Again, physiologically, the ICP pulse pressure waveform is created by the intracranial volume increase from the arterial blood entering the cranial vault. For adequate perfusion of the brain to occur, there must be a CSF egress into the spinal canal and a subsequent return following venous drainage. We believe that the correlation with P3 region is due to the return of CSF back into the cranial vault.

2. Study 2: Characteristics Peaks

The results of the previous study motivated an in-depth investigation into the relationship between the CSF flow in the cerebral aqueduct and individual peaks of the ICP pulse pressure waveform. Our study found a significant positive correlation between the width of the second peak of an ICP pulse (ICP-Wi2) and the ASV in patients with probable NPH. This was a rather specific finding in that neither mean ICP, the pulse amplitude (waveAmp), nor the width of the other two peaks achieved a significant correlation with ASV. This correlation supports our hypothesis that the P2 peak morphology would be more closely tied to measures of aqueductal CSF flow than the other ICP peaks (P1 and P3).

As shown in **Table 4**, the significant correlation with ASV was exclusive to the P2 region of ICP. Qualitatively the different characteristics of the three regions of an ICP pulse can be seen in **Figure 6** where two sets of ICP pulse pressure waveforms (**Figure 6C-D**) are shown for relatively different ASV (**Figure 6B**). Furthermore, the waveforms in

Figure 6C-D have equal mean ICP values (for both sets of waveforms) as it has been well established that mean ICP impacts ICP waveform morphology. One interpretation of this result is that the driving pressure required to displace an increased CSF volume through the aqueduct is related to the second peak of the ICP pulse. As noted previously, early physiological studies suggested that the first peak of ICP pulse primarily reflects the pulsations of large intracranial conductive arteries and that the third peak of an ICP pulse mainly reflects venous pulsation. We of course can only speculate as to what factors contribute to the P2 morphology. The high correlation with ASV might suggest that capillary-phase brain expansion, as proposed by Greitz,[3] is a likely dominant component. There are other possible drivers of ventricular CSF pulsatile movement, including pulsations in the ventricular choroid plexus.

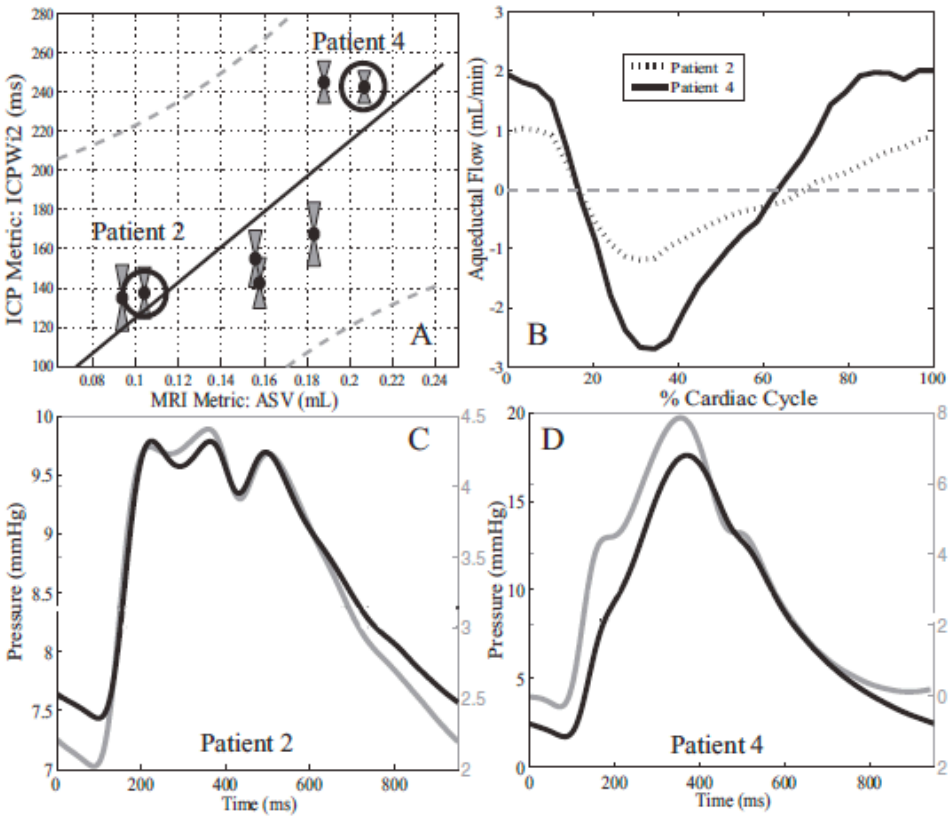

Figure 6: A) *Scatter plot of ICP-Wi2 vs. ASV, where ICP-Wi2 represents the width of P2. The correlation is significant with a p value = 0.0025.* ***B)*** *The ASV for two selected patients from Figure 4A* ***C)*** *Two example dominant ICP pulses with different mean ICPs for Patient 2 (low ASV).* ***D)*** *Two example dominant ICP pulses with different mean ICPs for Patient 4 (high ASV). For plots C and D the dominant pulses are plotted on separate axes which are color coded (black on the left, gray on the right) and are meant to compare waveform shapes between patients at equal mean ICP values. The mean ICP of the pressure pulse is depicted with a dashed line, each pair of dominant pulses (black and gray from C and D) are within 0.1 mmHg of each other (black =8.3 mmHg and gray = 3.0 mmHg). Reproduced with permission from Hamilton et al.*[145]

Physiologically, the relationship between the width of P2 and the ASV is likely related to finite time required to initiate the capillary bed expansion after each heart beat. Since the early 1940s CSF flow dynamics have been tied to arterial blood flow into the cranial vault . Greitz *et al.* expanded on this idea using phase contrast MRI, where they showed distinct brain expansion and retraction phases with an estimation of CSF flow in the

aqueduct delayed several hundred milliseconds after the ECG R wave due to the capillary bed expansion. In our study the PC-MRI measurement was made in the cerebral aqueduct. Incorporating the relationship between capillary bed expansion and CSF movement through the aqueduct we believe that the proposed link between the temporal metric of ICP and ASV is justifiable based on the capillary filling time. Moreover, we believe that the temporal correlations of ICP do not end with the filling of the capillary bed. We speculate that if a pulsatility measurement (flow stroke volume, etc) was made in another location (foramen of magnum, prepontine cistern, etc.) a different temporal ICP metric would be correlated. Finally, from a technical standpoint, studies investigating ICP pulse pressure temporal metrics are rare. Eide *et al.* reported no significant difference between NPH shunt responders and non-responders for mean ICP rise time (time from diastolic to the systolic peak). However, to our knowledge, the temporal features of the subpeaks in the ICP pulse have not been studied. MOCAIP provides the ability to reliably study subpeak temporal metrics and thus addresses an unmet need in the investigation of ICP waveform morphology investigation.

Much like the first study, this study supports the claim that the three individual regions of an ICP pulse provide complementary information to mICP. Eide's recent clinical studies provide additional evidence of this by demonstrating that ICP amplitude can potentially be more important in guiding the management of hydrocephalus patients[42] and subarachnoid hemorrhage patients than mean ICP. The present work shows that temporal metrics, such as ICP-Wi2, may provide additional insight into CSF dynamics and may play a role in managing patients with a wide variety of altered CSF dynamics.

A few tangentially related studies have shown relationships between ICP and CSF dynamics, although not directly linking ICP morphologic metrics and CSF dynamics. Alperin *et al.* utilized the characteristic pressure volume curve to estimate ICP non-invasively using MRI to quantify CSF and blood flow into the cranial vault. Although this study did not address ICP waveform morphology, it did suggest an association between the two measures of pulsatility investigated in our study. Another study investigated the efficacy of ASV for predicting outcome of shunt surgery in NPH, comparing ASV to lumbar CSF pressures before and during lumbar infusion study. The results showed no significant correlation between ASV and mean baseline lumbar pressure or ASV and mean plateau pressure. However, there was a correlation with both baseline and plateau pulse amplitude and ASV. [117] Again, the aforementioned studies simply suggest a possible relationship between noninvasive measures of CSF pulsatility and invasive pressure measurements, which act as reasonable background for our results.

A limitation of our study was the small sample size. In our study design, patients being evaluated for possible NPH were given the option to participate in the MRI research study. Some chose not to for personal reasons (including claustrophobia), and in others, the MRI studies obtained were not analyzable due to technical reasons (such as malfunctioning ECG gating software). In one respect, this small number of subjects coupled with the Bonferroni correction would challenge us more in achieving a significant *p* value when quantifying the correlation between metrics. We also acknowledge that there was a variable time lag between the ICP measurement and the time of PC-MRI imaging. However, acute changes of either ICP pulse morphology or

CSF flow dynamics are unlikely in this patient population and simultaneous measurements of invasive ICP morphology and CSF dynamics is not currently possible. It remains to be studied whether ICP-Wi2 can be a specific and sensitive metric to provide continuous surveillance of acute changes of the ASV.

E. Conclusion

Both studies support the hypothesis that morphological changes in the ICP pulse pressure waveform are correlated with CSF dynamics. The first study introduced a novel framework for investigating regional attributes of the ICP waveform based on the MOCAIP metrics. Specifically, we measured three CSF hydrodynamic metrics at two distinct locations within the cranial vault (aqueduct and prepontine cistern) and correlated them with ICP morphological metrics derived by the MOCAIP algorithm. We found significant correlations between CSF flow dynamics at both the aqueduct and the cistern correlating with region 2 and region 3 of the ICP pulse waveform, respectively. The individual studies further supported this idea by showing the width of the second peak of an ICP pulse wave is positively related to the volume of pulsatile CSF movement through the cerebral aqueduct. This finding is important because it helps our understanding of the specific ICP pulse wave morphology metrics studied in this work. Given the existing evidence that increased aqueductal CSF stroke volume is a marker of impaired CSF flow dynamics, ICP monitoring equipped with a metric of second peak width can thus offer a continuous assessment changes in CSF dynamics that mean ICP would fail to capture.

VIII. Chapter 5

A. Thesis Conclusion

Normal brain pulsatility is essential for healthy brain function. Although the pathoetiology of NPH has not clearly been defined, one overall conclusion that can be drawn from this work is altered brain pulsatility is present in NPH patients. The results of this work are multifaceted and have applications outside of NPH.

Since the invention of PC-MRI in the early 1990s the noninvasive study of blood and CSF flow has greatly advanced the understanding of cerebral dynamics. NPH in particular has been a focus of CSF research because of the obvious ventriculomegaly. Early work by Grietz, Bradley, and others help define the pulsatile nature of the brain and some of the abnormalities in NPH. This work built off their initial findings and defined a more complete understanding of the dysfunction, which extends past CSF flow and into temporal and variation changes. Future work in this area should confirm these initial findings with an emphasis on temporal and flow changes in both the ventricular system and the subarachnoid space.

The recent BEST TRIP trial shed doubt on the use of invasive ICP monitoring for management of TBI patients.[10] Despite some of the shortcomings of the trial (high mortality rate in both arms), we agree with the fundamental premise that traditional ICP monitoring is insufficient. The work presented in this thesis expands on the UCLA group's work showing that morphological features of ICP are advantageous compared to traditional mean ICP analysis. Additionally, the specific work investigating the

P3Ratio of the ICP pulse pressure waveform provides additional evidence for a physiological basis for the waveform changes. This work in particular has the potential to revolutionize the way ICP monitoring and cerebral blood flow monitoring is performed in the intensive care unit.

The final study of this thesis focuses on the relationship between noninvasive and invasive measures of brain pulsatility. Building off the latter portion of the previous chapter, this work extends the knowledge of the characteristic peaks of the ICP waveform, leading toward a more physiological understanding. This work for the first time showed a significant relationship between CSF flow within a specific anatomical location and a morphological feature of the ICP waveform. Again, this work is a first step toward a greater utilization of the ICP waveform for both diagnostic and prognostic purposes.

In conclusion, the work presented in this thesis approach the study of brain pulsatility from both the invasive and noninvasive modalities. NPH was also a common theme through this work as it has been well established that it is a disease of CSF flow dysfunction. Although this work has expanded the knowledge of brain pulsatility and dynamics in NPH patients much of the advances can be applied to other neurological conditions. The hope of the author is that this work will motivate the next generation of studies into brain pulsatility and ICP analysis.

IX. References

1 Min, K. J., Yoon, S. H. & Kang, J. K. New understanding of the role of cerebrospinal fluid: offsetting of arterial and brain pulsation and self-dissipation of cerebrospinal fluid pulsatile flow energy. *Med. Hypotheses* **76**, 884-886, doi:10.1016/j.mehy.2011.02.043 (2011).

2 OpenStaxCollege. in *"Circulation and the Central Nervous System Connexions"* Vol. 2013 (Connexions, http://cnx.org/content/m46719/1.3/, 2013).

3 Greitz, D. *et al.* Pulsatile brain movement and associated hydrodynamics studied by magnetic resonance phase imaging. The Monro-Kellie doctrine revisited. *Neuroradiology* **34**, 370-380 (1992).

4 Narayan, R. K. *et al.* Intracranial pressure: to monitor or not to monitor? A review of our experience with severe head injury. *J. Neurosurg.* **56**, 650-659, doi:10.3171/jns.1982.56.5.0650 (1982).

5 Czosnyka, M., Smielewski, P., Lavinio, A., Czosnyka, Z. & Pickard, J. D. A synopsis of brain pressures: which? when? are they all useful? *Neurol. Res.* **29** (2007).

6 Czosnyka, M. & Pickard, J. D. Monitoring and interpretation of intracranial pressure. *J. Neurol. Neurosurg. Psychiatry* **75**, 813-821, doi:10.1136/jnnp.2003.033126 (2004).

7 Faul, M., Wald, M. M., Rutland-Brown, W., Sullivent, E. E. & Sattin, R. W. Using a cost-benefit analysis to estimate outcomes of a clinical treatment guideline: testing theBrain Trauma Foundation guidelines for the treatment of severe traumatic brain injury. *J. Trauma* **63**, 1271-1278, doi:10.1097/TA.0b013e3181493080 (2007).

8 Ratanalert, S. *et al.* ICP threshold in CPP management of severe head injury patients. *Surg. Neurol.* **61**, 429-434; discussion 434-425, doi:10.1016/S0090-3019(03)00579-2 (2004).

9 Chambers, I. R., Treadwell, L. & Mendelow, A. D. Determination of threshold levels of cerebral perfusion pressure and intracranial pressure in severe head injury by using receiver-operating characteristic curves: an observational study in 291 patients. *J. Neurosurg.* **94**, 412-416, doi:10.3171/jns.2001.94.3.0412 (2001).

10 Chesnut, R. M. *et al.* A trial of intracranial-pressure monitoring in traumatic brain injury. *N. Engl. J. Med.* **367**, 2471-2481, doi:10.1056/NEJMoa1207363 (2012).

11 Lundberg, N. Continuous recording and control of ventricular fluid pressure in neurosurgical practice. *Acta Psychiatry Scand* **39** (1960).

12 Risberg, J., Lundberg, N. & Ingvar, D. H. Regional cerebral blood volume during acute transient rises of the intracranial pressure (plateau waves). *J. Neurosurg.* **31**, 303-310 (1969).

13 Rosner, M. J. & Becker, D. P. Origin and evolution of plateau waves experimental observations and a theoretical model. *J. Neurosurg.* **60**, 312–324 (1984).

14 Lemaire, J. J. *et al.* Slow Pressure Waves in the Cranial Enclosure. *Acta Neurochir. (Wien.)* **144**, 243-254 (2002).

15 Kasprowicz, M., Bergsneider, M., Czosnyka, M. & Hu, X. Association between ICP pulse waveform morphology and ICP B waves. *Acta Neurochir. Suppl.* **114**, 29-34, doi:10.1007/978-3-7091-0956-4_6 (2012).

16 Raftopoulos, C. *et al.* Morphological Quantitative Analysis of Intracranial Pressure Waves in Normal Pressure Hydrocephalus. *Neurological Reseach* **14** (1992).

17 Stephensen, H. *et al.* Objective B wave analysis in 55 patients with non-communicating and communicating hydrocephalus. *J. Neurol. Neurosurg. Psychiatry* **76**, 965-970, doi:10.1136/jnnp.2004.039834 (2005).

18 Woodworth, G. F., McGirt, M. J., Williams, M. A. & Rigamonti, D. Cerebrospinal fluid drainage and dynamics in the diagnosis of normal pressure hydrocephalus. *Neurosurgery* **64**, 919-925; discussion 925-916, doi:10.1227/01.NEU.0000341902.44760.10 (2009).

19 Lemaire, J. J., Boire, J. Y., Chazal, J. & Irthum, B. A computer software for frequential analysis of slow intracranial pressure waves. *Comput. Methods Programs Biomed.* **42**, 1-14 (1994).

20 Hara, K., Nakatani, S., Ozaki, K., Ikeda, T. & Mogami, H. Detection of the B waves in the oscillation of intracranial pressure by fast Fourier transform. *Med. Inform. (Lond.)* **15**, 125-131 (1990).

21 Eklund, A. *et al.* Two Computerized Methods used to analyze intracranial pressure B waves: comparison with traditional visual interpretation. *J. Neurosurg.* **94**, 392-396 (2001).

22 Kasprowicz, M. *et al.* Pattern recognition of overnight intracranial pressure slow waves using morphological features of intracranial pressure pulse. *J. Neurosci. Methods* **190**, 310-318, doi:10.1016/j.jneumeth.2010.05.015 (2010).
23 Takizawa, H., Gabra-Sanders, T. & Miller, J. D. Changes in the Cerebrospinal Fluid Pulse Wave Spectrum Associated with Raised Intracranial Preussre. *Neurosugery* **20** (1987).
24 Nitta, M. [The effect of increased intracranical pressure on pulse wave (author's transl)]. *Neurol. Med. Chir. (Tokyo)* **22**, 193-200 (1982).
25 Portnoy, H. D. & Chopp, M. Cerebrospinal Fluid Pulse Wave Form Analysis during Hypercapnia and Hypoxia. *Neurosurgery* **9** (1981).
26 Hirai, O., Handa, H., Ishikawa, M. & Kim, S. Epidural Pulse Waveform as an Indicator of Intracranial Pressure Dynamics. *Surg. Neurol.* **21**, 67-74 (1984).
27 Hirai, O., Ishikawa, M. & Handa, H. [Changes of epidural pulse waveform in increased intracranial pressure: an experimental study (author's transl)]. *No To Shinkei* **33**, 1235-1242 (1981).
28 Cardoso, E. R., Rowan, J. O. & Galbraith, S. Analysis of the cerebrospinal fluid pulse wave in intracranial pressure. *J. Neurosurg.* **59**, 817-821, doi:10.3171/jns.1983.59.5.0817 (1983).
29 Adolph, R., Fukusumi, H. & Fowler, N. Origin of Cerebrospinal Fluid Pulsations. (1966).
30 Dereymaeker, A., Stevens, S. A., Rombouts, J. J., Lacheron, J. M. & Pierquin, A. Study of the Influence of the Arterial Pressure upon the Morphology of Cisternal CSF Pulsations. *Europ. Neurol* **5**, 107-114 (1971).
31 Hamer, J., Alberti, E., Hoyer, S. & Wiedemann, K. Influence of Systemic and Cerebral Vascular Factors on the Cerebrospinal Fluid Pulse Waves. *J. Neurosurg* **46** (1977).
32 Czosnyka, M. *et al.* Intracranial pressure: more than a number. *Neurosurg. Focus* **22**, E10 (2007).
33 Wagshul, M. E., Eide, P. K. & Madsen, J. R. The pulsating brain: A review of experimental and clinical studies of intracranial pulsatility. *Fluids and barriers of the CNS* **8**, 5, doi:10.1186/2045-8118-8-5 (2011).
34 Brain Trauma, F. *et al.* Guidelines for the management of severe traumatic brain injury. VI. Indications for intracranial pressure monitoring. *J. Neurotrauma* **24 Suppl 1**, S37-44, doi:10.1089/neu.2007.9990 (2007).
35 Doyle, D. J. & Mark, P. W. S. Analysis of Intracranial Pressure *J. Clin. Monit.* **8**, 81-90 (1992).
36 Stocchetti, N. *et al.* Intensive care management of head-injured patients in Europe: a survey from the European brain injury consortium. *Intensive Care Med.* **27**, 400-406 (2001).
37 Eide, P. K. A new method for processing of continuous intracranial pressure signals. *Med. Eng. Phys.* **28**, 579-587, doi:10.1016/j.medengphy.2005.09.008 (2006).
38 Hu, X., Xu, P., Scalzo, F., Vespa, P. & Bergsneider, M. Morphological Clustering and Analysis of Continuous Intracranial Pressure. *IEEETransactions on Biomedical Engineering* **56** (2009).
39 Guendling, K. *et al.* Use of ICM+ software for on-line analysis of intracranial and arterial pressures in head-injured patients. *Acta Neurochir. Suppl.* **96**, 108-113 (2006).
40 Eide, P. K. Intracranial pressure parameters in idiopathic normal pressure hydrocephalus patients treated with ventriculo-peritoneal shunts. *Acta Neurochir. (Wien.)* **148**, 21-29; discussion 29, doi:10.1007/s00701-005-0654-8 (2006).
41 Eide, P. K. Demonstration of uneven distribution of intracranial pulsatility in hydrocephalus patients. *J. Neurosurg.* **109**, 912-917, doi:10.3171/JNS/2008/109/11/0912 (2008).
42 Eide, P. K. & Brean, A. Intracranial pulse pressure amplitude levels determined during preoperative assessment of subjects with possible idiopathic normal pressure hydrocephalus. *Acta Neurochir. (Wien.)* **148**, 1151-1156; discussion 1156, doi:10.1007/s00701-006-0896-0 (2006).
43 Eide, P. K. & Sorteberg, W. Diagnostic intracranial pressure monitoring and surgical management in idiopathic normal pressure hydrocephalus: a 6-year review of 214 patients. *Neurosurgery* **66**, 80-91, doi:10.1227/01.NEU.0000363408.69856.B8 (2010).
44 Hu, X., Gonzalez, N. & Bergsneider, M. Steady-state indicators of the intracranial pressure dynamic system using geodesic distance of the ICP pulse waveform. *Physiol. Meas.* **33**, 2017-2031, doi:10.1088/0967-3334/33/12/2017 (2012).
45 Hu, X., Hamilton, R., Baldwin, K., Vespa, P. M. & Bergsneider, M. Automated extraction of decision rules for predicting lumbar drain outcome by analyzing overnight intracranial pressure. *Acta Neurochir. Suppl.* **114**, 207-212, doi:10.1007/978-3-7091-0956-4_40 (2012).

46 Czosnyka, Z. H., Cieslicki, K., Czosnyka, M. & Pickard, J. D. Hydrocephalus shunts and waves of intracranial pressure. *Med. Biol. Eng. Comput.* **43**, 71-77 (2005).
47 Hu, X. *et al.* Intracranial pressure pulse morphological features improved detection of decreased cerebral blood flow. *Physiol. Meas.* **31**, 679-695, doi:10.1088/0967-3334/31/5/006 (2010).
48 Hu, X., Xu, P., Asgari, S., Vespa, P. & Bergsneider, M. Forecasting ICP elevation based on prescient changes of intracranial pressure waveform morphology. *IEEE Trans. Biomed. Eng.* **57**, 1070-1078, doi:10.1109/TBME.2009.2037607 (2010).
49 Soehle, M., Gies, B., Smielewski, P. & Czosnyka, M. Reduced complexity of intracranial pressure observed in short time series of intracranial hypertension following traumatic brain injury in adults. *J. Clin. Monit. Comput.* **27**, 395-403, doi:10.1007/s10877-012-9427-0 (2013).
50 Hutchinson, P. J. *et al.* Intracranial pressure monitoring in severe traumatic brain injury. *BMJ* **346**, f1000, doi:10.1136/bmj.f1000 (2013).
51 Lu, C. W. *et al.* Complexity of intracranial pressure correlates with outcome after traumatic brain injury. *Brain* **135**, 2399-2408, doi:10.1093/brain/aws155 (2012).
52 Eide, P. K. & Kerty, E. Static and pulsatile intracranial pressure in idiopathic intracranial hypertension. *Clin. Neurol. Neurosurg.* **113**, 123-128, doi:10.1016/j.clineuro.2010.10.008 (2011).
53 Eide, P. K. *et al.* A randomized and blinded single-center trial comparing the effect of intracranial pressure and intracranial pressure wave amplitude-guided intensive care management on early clinical state and 12-month outcome in patients with aneurysmal subarachnoid hemorrhage. *Neurosurgery* **69**, 1105-1115, doi:10.1227/NEU.0b013e318227e0e1 (2011).
54 Eide, P. K., Rapoport, B. I., Gormley, W. B. & Madsen, J. R. A dynamic nonlinear relationship between the static and pulsatile components of intracranial pressure in patients with subarachnoid hemorrhage. *J. Neurosurg.* **112**, 616-625, doi:10.3171/2009.7.JNS081593 (2010).
55 Eide, P. K. & Sorteberg, W. Intracranial pressure levels and single wave amplitudes, Glasgow Coma Score and Glasgow Outcome Score after subarachnoid haemorrhage. *Acta Neurochir. (Wien.)* **148**, 1267-1275; discussion 1275-1266, doi:10.1007/s00701-006-0908-0 (2006).
56 Budohoski, K. P. *et al.* Cerebral autoregulation after subarachnoid hemorrhage: comparison of three methods. *J. Cereb. Blood Flow Metab.* **33**, 449-456, doi:10.1038/jcbfm.2012.189 (2013).
57 Hakim, S. & Adams, R. D. The special clinical problem of symptomatic hydrocephalus with normal cerebrospinal fluid pressure. Observations on cerebrospinal fluid hydrodynamics. *J. Neurol. Sci.* **2**, 307-327 (1965).
58 Dandy, W. E. Intracranial Pressure without Brain Tumor: Diagnosis and Treatment. *Ann. Surg.* **106**, 492-513 (1937).
59 Bateman, G. A. The reversibility of reduced cortical vein compliance in normal-pressure hydrocephalus following shunt insertion. *Neuroradiology* **45**, 65-70, doi:10.1007/s00234-002-0901-0 (2003).
60 Egnor, M. Radiological assessment of hydrocephalus: new theories and implications for therapy. *Neurosurg. Rev.* **27**, doi:10.1007/s10143-004-0327-8 (2004).
61 Owler, B. K. *et al.* Normal pressure hydrocephalus and cerebral blood flow: a PET study of baseline values. *J. Cereb. Blood Flow Metab.* **24**, 17-23, doi:10.1097/01.WCB.0000093326.88757.49 (2004).
62 Egnor, M. R., Zheng, L., Rosiello, A., Gutman, F. & David, R. A Model of Pulsations in Communicating Hydrocephalus. *Pediatr. Neurosurg.* **36**, 281-303 (2002).
63 Borgesen, S. E. & Gjerris, F. The predictive value of conductance to outflow of CSF in normal pressure hydrocephalus. *Brain* **105**, 65-86 (1982).
64 Borgesen, S. E., Gjerris, F. & Sorensen, S. C. Intracranial Pressure and Conductance to Outflow of Cerebrospinal Fluid in Normal-Pressure Hydrocephlus. *J Neurourg* **50**, 489-493 (1979).
65 Bradley, W. G. *et al.* Normal-Pressure Hydrocephalus: Evaluation with Cerebrospinal Fluid Flow Measurements at MR Imaging. *Neuroradiology* **198**, 523-529 (1996).
66 Bateman, G. A. The pathophysiology of idiopathic normal pressure hydrocephalus: cerebral ischemia or altered venous hemodynamics? *AJNR Am. J. Neuroradiol.* **29**, 198-203, doi:10.3174/ajnr.A0739 (2008).
67 Bateman, G. A. Vascular Compliance in Normal Pressure Hydrocephalus. *AJNR Am. J. Neuroradiol.* **21**, 1574-1585 (2000).
68 Marmarou, A. *et al.* Diagnosis and management of idiopathic normal-pressure hydrocephalus: a prospective study in 151 patients. *J. Neurosurg* **102**, 987-977 (2005).

69 O'Brien, D. F., Javadpour, M., Collins, D. R., Spennato, P. & Mallucci, C. L. Endoscopic third ventriculostomy: an outcome analysis of primary cases and procedures performed after ventriculoperitoneal shunt malfunction. *J. Neurosurg.* **103**, 393-400, doi:10.3171/ped.2005.103.5.0393 (2005).
70 Prusseit, J. *et al.* Epidemiology, prevention and management of ventriculoperitoneal shunt infections in children. *Pediatr. Neurosurg.* **45**, 325-336, doi:10.1159/000257520 (2009).
71 Drake, J. M. *et al.* Randomized trial of cerebrospinal fluid shunt valve design in pediatric hydrocephalus. *Neurosurgery* **43**, 294-303; discussion 303-295 (1998).
72 Pollack, I. F., Albright, A. L. & Adelson, P. D. A randomized, controlled study of a programmable shunt valve versus a conventional valve for patients with hydrocephalus. Hakim-Medos Investigator Group. *Neurosurgery* **45**, 1399-1408; discussion 1408-1311 (1999).
73 Kestle, J. R. *et al.* Management of shunt infections: a multicenter pilot study. *J. Neurosurg.* **105**, 177-181, doi:10.3171/ped.2006.105.3.177 (2006).
74 Vanneste, J., Augustijn, P., Davies, G. A., Dirven, C. & Tan, W. F. Normal-pressure hydrocephalus. Is cisternography still useful in selecting patients for a shunt? *Arch. Neurol.* **49**, 366-370 (1992).
75 Williams, M. A., Razumovsky, A. Y. & Hanley, D. F. Comparison of Pcsf monitoring and controlled CSF drainage diagnose normal pressure hydrocephalus. *Acta Neurochir. Suppl.* **71**, 328-330 (1998).
76 Malm, M. *et al.* The predictive value of cerebrospinal fluid dynamic tests in patients with the idiopathic adult hydrocephalus syndrome. *Arch. Neurol.* **52**, 783–789 (1995).
77 Kahlon, B. Comparison between the lumbar infusion and CSF tap tests to predict outcome after shunt surgery in suspected normal pressure hydrocephalus. *J. Neurol. Neurosurg. Psychiatry* **73**, 721-726, doi:10.1136/jnnp.73.6.721 (2002).
78 Walchenbach, R., Geiger, E. & Thomeer, R. The value of temporary external lumbar CSF drainage in predicting the outcome of shunting on normal pressure hydrocephalus. *J. Neurol. Neurosurg. Psychiatry* **72**, 503-506, doi:10.1136/jnnp.72.4.503 (2002).
79 Haan, J. & Thomeer, R. T. Predictive value of temporary external lumbar drainage in normal pressure hydrocephalus. *Neurosurgery* **22**, 388-391 (1988).
80 Petersen, R. C., Mokri, B. & Laws, E. R., Jr. Surgical treatment of idiopathic hydrocephalus in elderly patients. *Neurology* **35**, 307-311 (1985).
81 Takeuchi, T., Kasahara, E., Iwasaki, M., Mima, T. & Mori, K. Indications for shunting in patients with idiopathic normal pressure hydrocephalus presenting with dementia and brain atrophy (atypical idiopathic normal pressure hydrocephalus). *Neurol. Med. Chir. (Tokyo)* **40**, 38-46; discussion 46-37 (2000).
82 Malm, J. *et al.* The predictive value of cerebrospinal fluid dynamic tests in patients with th idiopathic adult hydrocephalus syndrome. *Arch. Neurol.* **52**, 783-789 (1995).
83 Boon, A. J. *et al.* Dutch normal-pressure hydrocephalus study: prediction of outcome after shunting by resistance to outflow of cerebrospinal fluid. *J. Neurosurg.* **87**, 687-693, doi:10.3171/jns.1997.87.5.0687 (1997).
84 Qvarlander, S., Malm, J. & Eklund, A. CSF dynamic analysis of a predictive pulsatility-based infusion test for normal pressure hydrocephalus. *Med. Biol. Eng. Comput.*, doi:10.1007/s11517-013-1110-1 (2013).
85 Andersson, K., Sundstrom, N., Malm, J. & Eklund, A. Effect of resting pressure on the estimate of cerebrospinal fluid outflow conductance. *Fluids and barriers of the CNS* **8**, 15, doi:10.1186/2045-8118-8-15 (2011).
86 Eide, P. K. & Brean, A. Cerebrospinal fluid pulse pressure amplitude during lumbar infusion in idiopathic normal pressure hydrocephalus can predict response to shunting. *Cerebrospinal fluid research* **7**, 5, doi:10.1186/1743-8454-7-5 (2010).
87 Kim, D. J. *et al.* Index of cerebrospinal compensatory reserve in hydrocephalus. *Neurosurgery* **64**, 494-501; discussion 501-492, doi:10.1227/01.NEU.0000338434.59141.89 (2009).
88 Brean, A. & Eide, P. K. Assessment of idiopathic normal pressure patients in neurological practice: the role of lumbar infusion testing for referral of patients to neurosurgery. *Eur. J. Neurol.* **15**, 605-612, doi:10.1111/j.1468-1331.2008.02134.x (2008).
89 Eklund, A. *et al.* Assessment of cerebrospinal fluid outflow resistance. *Med. Biol. Eng. Comput.* **45**, 719-735, doi:10.1007/s11517-007-0199-5 (2007).

90 Bech-Azeddine, R., Nielsen, O. A., Logager, V. B. & Juhler, M. Lumbar elastance and resistance to CSF outflow correlated to patency of the cranial subarachnoid space and clinical outcome of endoscopic third ventriculostomy in obstructive hydrocephalus. *Minim. Invasive Neurosurg.* **50**, 189-194, doi:10.1055/s-2007-985890 (2007).
91 Kahlon, B., Sundbarg, G. & Rehncrona, S. Lumbar infusion test in normal pressure hydrocephalus. *Acta Neurol. Scand.* **111**, 379-384, doi:10.1111/j.1600-0404.2005.00417.x (2005).
92 Meier, U. & Bartels, P. The importance of the intrathecal infusion test in the diagnosis of normal pressure hydrocephalus. *J. Clin. Neurosci.* **9**, 260-267 (2002).
93 Kahlon, B., Sundbarg, G. & Rehncrona, S. Comparison between the lumbar infusion and CSF tap tests to predict outcome after shunt surgery in suspected normal pressure hydrocephalus. *J. Neurol. Neurosurg. Psychiatry* **73**, 721-726 (2002).
94 Meier, U. & Bartels, P. The importance of the intrathecal infusion test in the diagnostic of normal-pressure hydrocephalus. *Eur. Neurol.* **46**, 178-186 (2001).
95 Boon, A. J. *et al.* Does CSF outflow resistance predict the response to shunting in patients with normal pressure hydrocephalus? *Acta Neurochir. Suppl.* **71**, 331-333 (1998).
96 Czosnyka, M., Whitehouse, H., Smielewski, P., Simac, S. & Pickard, J. D. Testing of cerebrospinal compensatory reserve in shunted and non-shunted patients: a guide to interpretation based on an observational study. *J. Neurol. Neurosurg. Psychiatry* **60**, 549-558 (1996).
97 Borgesen, S. E. & Gjerris, F. Relationships between intracranial pressure, ventricular size, and resistance to CSF outflow. *J. Neurosurg.* **67**, 535-539, doi:10.3171/jns.1987.67.4.0535 (1987).
98 Luetmer, P. H. *et al.* Measurement of Cerebrospinal Fluid Flow at the Cerebral Aqueduct by Use of Phase-contrast Magnetic Resonance Imaging: Technique Validation and Utility in Diagnosing Idiopathic Normal Pressure Hydrocephalus. *Neurosurgery* **50** (2002).
99 Dixon, G. R. *et al.* Use of cerebrospinal fluid flow rates measured by phase-contrast MR to predict outcome of ventriculoperitoneal shunting for idiopathic normal-pressure hydrocephalus. *Mayo Clin. Proc.* **77**, 509-514, doi:10.4065/77.6.509 (2002).
100 Algin, O., Hakyemez, B. & Parlak, M. The efficiency of PC-MRI in diagnosis of normal pressure hydrocephalus and prediction of shunt response. *Acad. Radiol.* **17**, 181-187, doi:10.1016/j.acra.2009.08.011 (2010).
101 Scollato, A. *et al.* Changes in aqueductal CSF stroke volume in shunted patients with idiopathic normal-pressure hydrocephalus. *AJNR Am. J. Neuroradiol.* **30**, 1580-1586, doi:10.3174/ajnr.A1616 (2009).
102 Marmarou, A., Bergsneider, M., Klinge, P., Relkin, N. & Black, P. M. The Value of Supplemental Prognostic Tests for the Preoperative Assessment of Idiopathic Normal-pressure Hydrocephalus. *Neurosurgery*, S2-17-S12-28, doi:10.1227/01.neu.0000168184.01002.60 (2005).
103 Marmarou, A., Bergsneider, M., Relkin, N., Klinge, P. & Black, P. M. Development of Guidelines for Idiopathic Normal-pressure Hydrocephalus: Introduction. *Neurosurgery*, S2-1-S2-3, doi:10.1227/01.neu.0000168188.25559.0e (2005).
104 Moran, P. R. A flow velocity zeugmatographic interlace for NMR imaging in humans. *Magn. Reson. Imaging* **1**, 197-203 (1982).
105 Lotz, J., Meier, C., Leppert, A. & Galanski, M. Cardiovascular flow measurement with phase-contrast MR imaging: basic facts and implementation. *Radiographics* **22**, 651-671 (2002).
106 Baledent, O. *et al.* Relationship between cerebrospinal fluid and blood dynamics in healthy volunteers and patients with communicating hydrocephalus. *Invest. Radiol.* **39**, 45-55, doi:10.1097/01.rli.0000100892.87214.49 (2004).
107 Enzmann, D. R. & Pelc, N. J. Normal flow patterns of intracranial and spinal cerebrospinal fluid defined with phase-contrast cine MR imaging. *Radiology* **178**, 467-474, doi:10.1148/radiology.178.2.1987610 (1991).
108 Bhadelia, R. A., Bogdan, A. R. & Wolpert, S. M. Analysis of cerebrospinal fluid flow waveforms with gated phase-contrast MR velocity measurements. *AJNR Am. J. Neuroradiol.* **16**, 389-400 (1995).
109 Nitz, W. N. *et al.* Flow dynamics of cerebrospinal fluid Assessment with phase contrast velocity MR imaging performed with retrospective cardiac gating. *Radiology* **183**, 395-405 (1992).

110 Feinberg, D. A. & Mark, A. S. Human brain motion and cerebrospinal fluid circulation demonstrated with MR velocity imaging. *Radiology* **163**, 793-799, doi:10.1148/radiology.163.3.3575734 (1987).
111 Alperin, N., Lee, S. H., Loth, F., Raksin, P. B. & Lichtor, T. MR–Intracranial Pressure (ICP): A Method to Measure Intracranial Elastance and Pressure Noninvasively by Means of MR Imaging: Baboon and Human Study. *Radiology* **217**, 877-885 (2000).
112 Tain, R. W. & Alperin, N. Noninvasive intracranial compliance from MRI-based measurements of transcranial blood and CSF flows: indirect versus direct approach. *IEEE Trans. Biomed. Eng.* **56**, 544-551 (2009).
113 Menick, B. J. Phase-contrast magnetic resonance imaging of cerebrospinal fluid flow in the evaluation of patients with Chiari I malformation. *Neurosurg. Focus* **11**, E5 (2001).
114 Bhadelia, R. A. *et al.* Cerebrospinal fluid flow waveforms: analysis in patients with Chiari I malformation by means of gated phase-contrast MR imaging velocity measurements. *Radiology* **196**, 195-202, doi:10.1148/radiology.196.1.7784567 (1995).
115 Black, P. M. Idiopathic normal-pressure hydrocephalus. Results of shunting in 62 patients. *J. Neurosurg.* **52**, 371-377, doi:10.3171/jns.1980.52.3.0371 (1980).
116 Bradley, W. G. *et al.* Marked Cerebrospinal Fluid Void: Indicator of Successful Shunt in Patents with Suspected Normal-Pressure Hydrocephlus. *Radiology* **178**, 459-466 (1991).
117 Kahlon, B., Annertz, M., Stahlberg, F. & Rehncrona, S. Is aqueductal stroke volume, measured with cine phase-contrast magnetic resonance imaging scans useful in predicting outcome of shunt surgery in suspected normal pressure hydrocephalus? *Neurosurgery* **60**, 124-129; discussion 129-130, doi:10.1227/01.NEU.0000249208.04344.A3 (2007).
118 Sharma, A. K., Gaikwad, S., Gupta, V., Garg, A. & Mishra, N. K. Measurement of peak CSF flow velocity at cerebral aqueduct, before and after lumbar CSF drainage, by use of phase-contrast MRI: utility in the management of idiopathic normal pressure hydrocephalus. *Clin. Neurol. Neurosurg.* **110**, 363-368, doi:10.1016/j.clineuro.2007.12.021 (2008).
119 Wagshul, M. E., Chen, J. J., Egnor, M. R., McCormack, E. J. & Roche, P. E. Amplitude and phase of cerebrospinal fluid pulsations: experimental studies and review of the literature. *J. Neurosurg.* **104**, 810-819 (2006).
120 Greitz, D. Cerebrospinal fluid circulation and associated intracranial dynamics. A radiologic investigation using MR imaging and radionuclide cisternography. *Acta Radiol. Suppl.* **386**, 1-23 (1993).
121 Wagshul, M. E. *et al.* Resonant and notch behavior in intracranial pressure dynamics. *J. Neurosurg. Pediatr.* **3**, 354-364, doi:10.3171/2009.1.PEDS08109 (2009).
122 Al-Zain, F. T., Rademacher, G., Meier, U., Mutze, S. & Lemcke, J. The role of cerebrospinal fluid flow study using phase contrast MR imaging in diagnosing idiopathic normal pressure hydrocephalus. *Acta Neurochir. Suppl.* **102**, 119-123 (2008).
123 Abbey, P., Singh, P., Khandelwal, N. & Mukherjee, K. K. Shunt surgery effects on cerebrospinal fluid flow across the aqueduct of Sylvius in patients with communicating hydrocephalus. *J. Clin. Neurosci.* **16**, 514-518, doi:10.1016/j.jocn.2008.05.009 (2009).
124 Alperin, N. & Lee, S. H. PUBS: pulsatility-based segmentation of lumens conducting non-steady flow. *Magn. Reson. Med.* **49**, 934-944, doi:10.1002/mrm.10455 (2003).
125 Kim, D., Choi, J., Huh, R., Yun, P. & Kim, D. I. Quantitative Assessment of Cerebrospinal Fluid Hydrodynamics using a Phase-Contrast CINE MR Image in Hydrocephalus. *Child's Nerv Syst* **15**, 461-467 (1999).
126 Bateman, G. A., Levi, C. R., Schofield, P., Wang, Y. & Lovett, E. C. The pathophysiology of the aqueduct stroke volume in normal pressure hydrocephalus: can co-morbidity with other forms of dementia be excluded? *Neuroradiology* **47**, 741-748, doi:10.1007/s00234-005-1418-0 (2005).
127 Edwards, R. J., Dombrowski, S. M., Luciano, M. G. & Pople, I. K. Chronic hydrocephalus in adults. *Brain Pathol.* **14**, 325-336 (2004).
128 Hamilton, R. *et al.* Quantification of pulsatile cerebrospinal fluid flow within the prepontine cistern. *Acta Neurochir. Suppl.* **114**, 191-195, doi:10.1007/978-3-7091-0956-4_37 (2012).
129 Yoshida, K. *et al.* Phase-Contrast MR Studies of CSF Flow Rate in the Cerebral Aqueduct and Cervical Subarachnoid Space with Correlation-based Segmentation. *Magn. Reson. Med. Sci.* **8**, 91-100 (2009).

130 Unal, O. *et al.* Cine phase-contrast MRI evaluation of normal aqueductal cerebrospinal fluid flow according to sex and age. *Diagn Interv Radiol* **15**, 227-231, doi:10.4261/1305-3825.DIR.2321-08.1 (2009).
131 Miyake, H., Ohta, T., Kajimoto, Y. & Nagao, K. New Concept for the Pressure Setting of a Programmable Pressure Valve and Measurement of in vivo Shunt Flow Performed using a Microflowmeter. *J. Neurosurg* **92**, 181-187 (2000).
132 Muthupillai, R. *et al.* Magnetic resonance elastography by direct visualization of propagating acoustic strain waves. *Science* **269**, 1854-1857 (1995).
133 Freimann, F. B. *et al.* Alteration of brain viscoelasticity after shunt treatment in normal pressure hydrocephalus. *Neuroradiology* **54**, 189-196, doi:10.1007/s00234-011-0871-1 (2012).
134 Shlens, J. Notes on Kullback-Leibler Divergence and Likelihood Theory. (2007).
135 Asgari, S., Bergsneider, M., Hamilton, R., Vespa, P. & Hu, X. Consistent changes in intracranial pressure waveform morphology induced by acute hypercapnic cerebral vasodilatation. *Neurocrit. Care* **15**, 55-62, doi:10.1007/s12028-010-9463-x (2011).
136 Hamilton, R. *et al.* Forecasting intracranial pressure elevation using pulse waveform morphology. *Conf. Proc. IEEE Eng. Med. Biol. Soc.* **2009**, 4331-4334, doi:10.1109/IEMBS.2009.5332749 (2009).
137 Hu, X., Xu, P., Lee, D. J., Vespa, P. & Bergsneider, M. Morphological changes of intracranial pressure pulses are correlated with acute dilatation of ventricles. *Acta Neurochir* **102**, 131-136 (2008).
138 Kim, S. *et al.* Inter-subject correlation exists between morphological metrics of cerebral blood flow velocity and intracranial pressure pulses. *Neurocrit. Care* **14**, 229-237, doi:10.1007/s12028-010-9471-x (2011).
139 Kim, S., Hamilton, R., Pineles, S., Bergsneider, M. & Hu, X. Noninvasive intracranial hypertension detection utilizing semisupervised learning. *IEEE Trans. Biomed. Eng.* **60**, 1126-1133, doi:10.1109/TBME.2012.2227477 (2013).
140 Scalzo, F., Asgari, S., Kim, S., Bergsneider, M. & Hu, X. Robust peak recognition in intracranial pressure signals. *Biomed Eng Online* **9**, 61, doi:10.1186/1475-925X-9-61 (2010).
141 Scalzo, F., Xu, P., Asgari, S., Bergsneider, M. & Hu, X. Regression analysis for peak designation in pulsatile pressure signals. *Med. Biol. Eng. Comput.* **47**, 967-977, doi:10.1007/s11517-009-0505-5 (2009).
142 Hu, X. *et al.* An algorithm for extracting intracranial pressure latency relative to electrocardiogram R wave. *Physiol. Meas.* **29**, 459-471, doi:10.1088/0967-3334/29/4/004 (2008).
143 Afonso, V. X., Tompkins, W. J., Nguyen, T. Q. & Luo, S. ECG beat detection using filter banks. *IEEE Trans. Biomed. Eng.* **46**, 192-202 (1999).
144 Governale, L. S., Fein, N., Logsdon, J. & Black, P. M. Techniques and complications of external lumbar drainage for normal pressure hydrocephalus. *Neurosurgery* **63**, 379-384; discussion 384, doi:10.1227/01.NEU.0000327023.18220.88 (2008).
145 Hamilton, R. *et al.* Intracranial pressure pulse waveform correlates with aqueductal cerebrospinal fluid stroke volume. *J. Appl. Physiol.* **113**, 1560-1566, doi:10.1152/japplphysiol.00357.2012 (2012).
146 Du Boulay, G., O'Connell, J., Currie, J., Bostick, T. & Verity, P. Further investigations on pulsatile movements in the cerebrospinal fluid pathways. *Acta Radiol. Diagn. (Stockh.)* **13**, 496-523 (1972).
147 Greitz, T. Cerebral blood flow in occult hydrocephalus studied with angiography and the xenon 133 clearance method. *Acta Radiol. Diagn. (Stockh.)* **8**, 376-384 (1969).
148 Greitz, T. V., Grepe, A. O., Kalmer, M. S. & Lopez, J. Pre- and postoperative evaluation of cerebral blood flow in low-pressure hydrocephalus. *J. Neurosurg.* **31**, 644-651, doi:10.3171/jns.1969.31.6.0644 (1969).
149 Mathew, N. T., Meyer, J. S., Hartmann, A. & Ott, E. O. Abnormal cerebrospinal fluid-blood flow dynamics. Implications in diagnosis, treatment, and prognosis in normal pressure hydrocephalus. *Arch. Neurol.* **32**, 657-664 (1975).
150 Salmon, J. H. & Timperman, A. L. Effect of intracranial hypotension on cerebral blood flow. *J. Neurol. Neurosurg. Psychiatry* **34**, 687-692 (1971).
151 Salmon, J. H. & Timperman, A. L. Cerebral blood flow in posttraumatic encephalopathy. The effect of ventriculoatrial shunt. *Neurology* **21**, 33-42 (1971).

152 Meyer, J. S. *et al.* Normal pressure hydrocephalus. Influences on cerebral hemodynamic and cerebrospinal fluid pressure--chemical autoregulation. *Surg. Neurol.* **21**, 195-203 (1984).
153 Meyer, J. S. *et al.* Evaluation of treatment of normal-pressure hydrocephalus. *J. Neurosurg.* **62**, 513-521, doi:10.3171/jns.1985.62.4.0513 (1985).
154 Graff-Radford, N. R. *et al.* Regional cerebral blood flow in normal pressure hydrocephalus. *J. Neurol. Neurosurg. Psychiatry* **50**, 1589-1596 (1987).
155 Vorstrup, S. *et al.* Cerebral blood flow in patients with normal-pressure hydrocephalus before and after shunting. *J. Neurosurg.* **66**, 379-387, doi:10.3171/jns.1987.66.3.0379 (1987).
156 Maeder, P. & de Tribolet, N. Xenon CT measurement of cerebral blood flow in hydrocephalus. *Childs Nerv. Syst.* **11**, 388-391 (1995).
157 Klinge, P. *et al.* PET and CBF studies of chronic hydrocephalus: a contribution to surgical indication and prognosis. *J. Neuroimaging* **8**, 205-209 (1998).
158 Klinge, P. M., Berding, G., Brinker, T., Knapp, W. H. & Samii, M. A positron emission tomography study of cerebrovascular reserve before and after shunt surgery in patients with idiopathic chronic hydrocephalus. *J. Neurosurg.* **91**, 605-609, doi:10.3171/jns.1999.91.4.0605 (1999).
159 Momjian, S. *et al.* Pattern of White Matter Regional Cerebral Blood Flow and Autoregulation in Normal Pressure Hydrocephalus. *Brain* **127**, 965-972 (2004).
160 Waldemar, G. *et al.* High resolution SPECT with [99mTc]-d,l-HMPAO in normal pressure hydrocephalus before and after shunt operation. *J. Neurol. Neurosurg. Psychiatry* **56**, 655-664 (1993).
161 Kushner, M. *et al.* Cerebral hemodynamics in the diagnosis of normal pressure hydrocephalus. *Neurology* **34**, 96-99 (1984).
162 Mamo, H. L. *et al.* Cerebral blood flow in normal pressure hydrocephalus. *Stroke* **18**, 1074-1080 (1987).
163 Kristensen, B. *et al.* Regional cerebral blood flow, white matter abnormalities, and cerebrospinal fluid hydrodynamics in patients with idiopathic adult hydrocephalus syndrome. *J. Neurol. Neurosurg. Psychiatry* **60**, 282-288 (1996).
164 Hayashi, M., Kobayashi, H., Kawano, H., Yamamoto, M. & Maeda, T. Cererbral Blood Flow and ICP Patterns in Patients with Communicating Hydrocephalus after Aneurysm Rupture. *J. Neurosurg* **61**, 30-36 (1984).
165 Symon, L. & Dorsch, N. Use of Long-term intracranial Pressure Measurement to Assess Hydrocephalic Patients Prior to Shunt Surgery. *J. Neurosurg* **42** (1975).
166 Tanaka, A., Kimura, M., Nakayama, Y., Yoshinaga, S. & Tomonaga, M. Cerebral blood flow and autoregulation in normal pressure hydrocephalus. *Neurosurgery* **40**, 1161-1165; discussion 1165-1167 (1997).
167 Raftopoulos, C. *et al.* Cognitive recovery in idiopathic normal pressure hydrocephalus: a prospective study. *Neurosurgery* **35**, 397-404; discussion 404-395 (1994).
168 Klinge, P., Marmarou, A., Bergsneider, M., Relkin, N. & Black, P. M. Outcome of Shunting in Idiopathic Normal-pressure Hydrocephalus and the Value of Outcome Assessment in Shunted Patients. *Neurosurgery*, S2-40-S42-52, doi:10.1227/01.neu.0000168187.01077.2f (2005).